Spectroscopic Ellipsometry Analysis of Nanoporous Low Dielectric Constant Films Processed via Supercritical CO_2 for Next-generation Microelectronic Devices

---

A dissertation

Presented to the Faculty of the Graduate School

University of Missouri-Columbia

In Partial Fulfillment

Of the Requirements for the Degree

Doctor of Philosophy

By

Maslina T. Othman

Dr. Shubhra Gangopadhyay, Dissertation Supervisor

May 2007

The undersigned, appointed by the dean of the Graduate School, have examined the dissertation entitled

Spectroscopic Ellipsometry Analysis of Nanoporous Low Dielectric Constant Films Processed via Supercritical CO_2 for Next-generation Microelectronic Devices

presented by Maslina Tasrin Othman,

a candidate for the degree of Doctor of Philosophy in Electrical and Computer Engineering,

and hereby certify that, in their opinion it is worthy of acceptance.

Professor Shubhra Gangopadhyay

Professor Lex A. Akers

Professor Suchismita Guha

Professor Ping Yu

Professor Rajesh Shende

Acknowledgements

First and foremost I would like to thank my dissertation supervisor, Professor Shubhra Gangopadhyay, who is supported me in every possible way being her guidance and ideas. Thank you for guiding me through out my PhD's studies. Without her I would not have accomplished this. What she taught me is far beyond this research itself.

It is also a pleasure to acknowledge the assistance of Dr. Jorge Lubguban and his family throughout my PhD program.

My gratitude also goes to the faculty and staff in the Department of Electrical Engineering at the University of Missouri-Columbia for contributing in one way or another to my studies. I would also like to thank to Tami Beatty and Betty Barfield for helping me in many ways through my undergraduate, master and Ph.D studies.

Last but not least, I am very grateful to my family for supporting me in many ways. I am extremely thankful to my many friends who supported me through difficulties I encountered during my research and studies.

Table of Contents

Acknowledgements………………………………………………………………..…..ii

List of Figures ……………………………………………………………………….....v

List of Tables…………………………………………………………………….....vii

Abstract……………………………………………………………………..…………..x

Abbreviations………………………………………………………………………viii

Chapter 1 1

1.1 THE NEED FOR LOW-K MATERIALS 1
1.2 POSSIBLE MATERIAL USED AS INSULATOR LAYER 3
1.3 INTRODUCING POROSITY TO LOWER K-VALUE 5
1.4 $SCCO_2$ TO GENERATE PORES 6
1.5 $SCCO_2$ PROCESS TO SOLVE LOW-K INTEGRATION ISSUES 7
1.6 PROBLEMS IN POROUS FILM CHARACTERIZATION 8
1.7 VASE™ AS A GOOD MEASURING TECHNIQUE TO POROUS FILM 9
1.8 OBJECTIVE OF THE DISSERTATION 10
1.9 DISSERTATION ORGANIZATION 16

Chapter 2 18

2.1 SUPERCRITICAL CO_2 PROCESS TO GENERATE POROUS FILM 18
2.2 SUPERCRITICAL OR VAPOR TREATMENT WITH HMDS TO REPAIR POROUS FILM 24
2.3 SUPERCRITICAL OR VAPOR TREATMENT WITH TMCS TO REPAIR POROUS FILM 28
2.4 OTHER APPLICATIONS USING SUPERCRITICAL FLUID TECHNOLOGY 30

Chapter 3 32

3.1 OVERVIEW 32
3.2 VARIABLE ANGLE SPECTROSCOPIC ELLIPSOMETRY 33
3.2.1 Basic concepts: How do ellipsometers work? 33
3.2.2 Ellipsometer Configuration 35
3.2.3 Reflection/refraction at the planar interface 36
3.2.4 Variable Angle Spectroscopic Ellipsometry (VASE™) Measurement and Analysis 43
3.3 ANALYTICAL METHOD USING SPECTROSCOPY ELLIPSOMETRY TO CHARACTERIZE THIN FILM 47
3.3.1 Cauchy layer 47
3.3.2 Bruggeman Effective Medium Approximation (BEMA) layer 47
3.3.3 Graded layer 49
3.3.4 Surface roughness 49
3.3.5 Silicon substrate 50
3.4 ELLIPSOMETRY MODELING FOR POROUS FILM 50
3.5 FOURIER TRANSFORM INFRARED (FT-IR) 51
3.5.1 Absorbance, Lambert-Beer's Law 52

3.5.2 Quantitative spectral analysis *55*
3.6 CAPACITANCE-VOLTAGE (C-V) ELECTRICAL MEASUREMENT 59

Chapter 4 60

4.1 OVERVIEW 60
4.1.1 Fabrication of sacrificial porogen approach *62*
4.1.2 Description of samples used in this research *63*
4.2 THERMAL ANNEALING PROCESS 64
4.3 SUPERCRITICAL CO_2 PROCESS 65
4.3.1 High Pressure $SCCO_2$ Experimental System *65*
4.3.2 $SCCO_2$ treatment procedure *67*
4.4 EXPERIMENT PARAMETERS 69

Chapter 5 70

5.1 OVERVIEW 70
5.2 IMPLEMENTED SPECTROSCOPIC ELLIPSOMETRY ANALYTICAL METHOD FOR CHARACTERIZING POROUS THIN FILM 71
5.3 $SCCO_2$ WITH PULSING MODE TO REMOVE POROGEN EFFECTIVELY 82
5.3.1 Overview *82*
5.3.2 Experimental Procedure *82*
5.3.3 Results and Discussions *83*
5.4 POROGEN AND WATER REMOVAL VIA $SCCO_2$ 85
5.4.1 Overview *85*
5.4.2 Experimental Procedure *86*
5.4.3 Results and Discussions *86*
5.5 SILYLATION (TMCS) TO RESTORE HYDROPHOBICITY IN POROUS FILM VIA $SCCO_2$ 93
5.5.1 Overview *93*
5.5.2 Experimental Procedure *94*
5.5.3 Results and Discussions *94*
5.6 SPECTROSCOPIC ELLIPSOMETRY STUDY OF THE REDUCTION IN POROSITY OF OPEN-PORE ORGANOSILICATE FILMS AFTER HEXAMETHYLDISILAZANE TREATMENT 98
5.6.1 Overview *98*
5.6.2 Experimental Procedure *99*
5.6.3 Results and discussion *102*
5.7 CHARACTERIZATION OF PLASMA EXPOSED SAMPLES FOLLOWED BY POROGEN/WATER REMOVAL. 110
5.7.1 Overview *110*
5.7.2 Experiment *110*
5.7.3 Results and discussion *111*

Chapter 6 116

6.1 CONCLUSION/FUTURE WORK 116

Reference 118

Vita 124

List of Figures

Figure 1-1. Moore's Law predicted exponential increases in the number of transistors integrated into Intel processors [Reference: www.intel.com] 2
Figure 1-2 Process flow (a) industry and (b) proposed in this dissertation. 15
Figure 2-1. A phase diagram showing the different phase and supercritical region......... 19
Figure 2-2 The behavior of CO_2 in open and closed sealed vessel................................. 20
Figure 3-1. Interaction of polarized light with sample of interest. 34
Figure 3-2. Rotating Analyzer Ellipsometer, Variable Angle Spectroscopy Ellipsometer VASE™ (J.A. Woolam Co. Inc.) used in this work. 36
Figure 3-3. Illustrates oblique incident, refracted and reflected beam on planar surface from medium *0* to medium *1*. 39
Figure 3-4. Incident beam refracted into film resulted in multiple internal reflection and reflected out to medium *0*. 43
Figure 3-5. Flow chart of spectroscopy ellipsometry analysis. 46
Figure 3-6. Illustrates schemative representative of Bruggeman Effective Medium Approximation theory. 48
Figure 3-7. Shows the schematic representative of (a) single layer and (b) graded layer to describe a film. 49
Figure 3-8. Illustration of surface roughness on film. 50
Figure 3-9. A simple absorption experiment showing some incident light is been absorbed by sample. 52
Figure 3-10. Comparison FT-IR spectra between (a) absorption and (b) transmission as a function of wavenumber (cm^{-1}). 55
Figure 3-11. Example of FT-IR spectra (a) baseline construction and (b) baseline corrected. 56
Figure 3-12. Demonstration of multiple Gaussian curve fitting of FTIR spectra............. 57
Figure 4-1. General procedure in preparing nanoporous film. 61
Figure 4-2. Nanoporous film with two different morphology structure (a) closed-pore and (b) open-pore. 62
Figure 4-3. Procedures to prepare nanoporous film using sacrificial porogen approach. 63
Figure 4-4. Schematic diagram of $SCCO_2$ system. 66
Figure 5-1. Nonporous PMSSQ (a) Ψ fit spectra (b) Δ fit spectra using Cauchy model. (MSE = 5.5). 71
Figure 5-2. Generated and experimental (a) Ψ fit spectra and (b) Δ fit spectra using Cauchy model for open-pore sample with an MSE = 3.1.. 74
Figure 5-3. Depth profiles at 633 nm wavelength for open pore film using single BEMA with grading [MSE = 1.5] and two BEMA layers with grading [MSE = 1.5]................. 75
Figure 5-4 Depth profiles at 633 nm wavelength for (1) closed pore films using single BEMA with grading [MSE = 2.2], two BEMA layers with grading [MSE = 2.2] and (2) single porous film using single BEMA grading [MSE = 1.0] 77
Figure 5-5. Generated and experimental (a) and (b) using single BEMA model (MSE=77) and (c) and (d) using double BEMA model (MSE=3.5).. 79

Figure 5-6. Depth profile at 633 nm wavelength for bi-layer porous film with different porogen loading. 80
Figure 5-7. Depth profile at 633 nm wavelength for O_2 ashed. 81
Figure 5-8. Multiple co-solvents injections $SCCO_2$ process in comparison with annealed sample. 84
Figure 5-9. FTIR –CH absorption spectra for multiple injections in $SCCO_2$ process 85
Figure 5-10. Refractive index depth profile at 633 nm wavelength for closed-pore film after several treatments: before extraction, $SCCO_2$/co-solvents and $SCCO_2$/Methanol process 89
Figure 5-11 FTIR spectra of –OH absorption band after several treatments: as-cured, $SCCO_2$/co-solvents and $SCCO_2$/Methanol process. 90
Figure 5-12. Refractive index depth profile at 633 nm wavelength for open-pore film after several treatments: before extraction, $SCCO_2$/co-solvents and $SCCO_2$/Methanol process 91
Figure 5-13. FTIR absorption spectra of -OH and -CH band after Butanol* and Methanol* $SCCO_2$ treatment. 93
Figure 5-14. Absorption spectra of -OH region after several treatments including TMCS treatment for (a) open-pore and (b) closed-pore sample. 95
Figure 5-15 Percentage water remained in the sample after different treatments. 96
Figure 5-16. Absorption spectra of CH region after several treatments including TMCS treatment for open-pore sample. 97
Figure 5-17. Absorption spectra of CH region after several treatments including TMCS treatment for closed-pore. 98
Figure 5-18 SEM images of open-pore sample after (a) annealing, (b) plasma treatment and (c)HMDS treatment and the correspondence (d) refractive index depth profile. 104
Figure 5-19 SEM images of closed-pore sample after (a) annealing, (b) plasma treatment and (c)HMDS treatment and the correspondence (d) refractive index depth profile. 109
Figure 5-20 shows the refractive index depth profile of open-pore processed samples (a) with plasma process and (b) without plasma process. 112
Figure 5-21 FTIR spectra of 2800cm-1 – 4000 cm^{-1} and 950cm^{-1} – 1250cm^{-1}, open-pore pore processed samples (a) and (c) with plasma process (b) and (d) without plasma process. For Si-O-Si (950 cm^{-1} – 1250 cm^{-1}) spectra. 113
Figure 5-22 Depth profile of closed-pore processed samples (a) with plasma process and (b) without plasma process. 114
Figure 5-23 FTIR spectra of 2800cm-1 – 4000 cm-1 and 950cm-1 – 1250cm-1, closed-pore pore processed samples (a) and (c) with plasma process (b) and (d) without plasma process. 115

List of Tables

Table 1-1 Shows listed available low-*k* dielectric layer 5
Table 1-2 Flowchart overview dissertation research work. 13
Table 2-1. Physical properties of a gas, liquid and supercritical fluid. 21
Table 3-1. Selected FT-IR active band peaks used in this research. 58
Table 4-1. Fabricated open- and closed-pore samples used in this study with either PPG or PPO as sacrificial porogen. 64
Table 5-1. List of optical constants and MSE for nonporous PMSSQ and SiO_2 film modeled as Cauchy and modified graded Cauchy layer. 72
Table 5-2. List of thickness, optical constant, porosity and MSE for open- and closed-pore film using Cauchy and BEMA model with or without grading. 73
Table 5-3 List of thickness, refractive index (R.I.), porosity and dielectric constant for both open- and closed-pore films of as-cured, annealed, plasma processed and hexamethyldisilazane treated 102

Abbreviations

BEMA - Bruggeman Effective Medium Approximation

BEOL - back-end-of-line

CMP - chemical mechanical planarization

C-SiO_2 - carbon doped SiO_2

C-V – Capacitance Voltage

EP - ellipsometric porosimetry

F-SiO_2 - fluorinated silicon dioxide film

FT-IR - Fourier Transform Infra-red

HMDS - Hexamethyldisilizane

ITRS - International Technology Roadmap for Semiconductors

N_2 - nitrogen

PMSSQ - poly(methylsilsesquioxane)

PECVD - plasma enhanced chemical vapor deposition

PALS - positron annihilation lifetime spectroscopy

PGMEA - propylene glycol methyl ether acetate

PPG - poly propylene glycol

RC - resistance-capacitance

$SCCO_2$ - Supercritical Carbon Dioxide

SAXS - small-angle x-ray spectrometry

SEM - scanning electron microscopy

TMCS - Trimethylchlorosilane

TEFS - triethoxyfluorosilane

T_g - glass transtition

VT – Vapor treatment

VASE™ - variable angle spectroscopic ellipsometry

XPS - x-ray photoelectron spectroscopy

XRR - x-ray reflectivity

Abstract

Spectroscopic Ellipsometry Analysis of Nanoporous Low Dielectric Constant Films Processed via Supercritical CO_2 for Next-generation Microelectronic Devices

My research will address issues at the back-end-of-line in microelectronics fabrication, specifically the need for Low-*k* extendibility. The International Roadmap for Semiconductors (2005) suggested that interconnect insulation must be replaced with a material having an ultra-low dielectric constant (*k*) of < 2.0 and can withstand rigorous current process integration for the 65 nm technology. Creating porosity in the films produces *k*-values as low (1.0) air. In this research, supercritical CO_2 ($SCCO_2$) process is utilized to create pores, remove water, repair plasma-damaged sample and seal pores. These multi-step processing does not only produce low-*k* film but also create device reliability. Spectroscopy ellipsometric (SE) analysis is used to evaluate the performance of each process on porous film. In SE analysis, Cauchy, Bruggeman Effective Medium Approximation and graded models are used to model the processed samples. The depth profile SE analysis demonstrates the individual process performance based on its changes of refractive index (*n*) throughout the film thickness. SE also provide important film properties like thickness, porosity etc. In addition to SE, Fourier Transform Infra-red (FT-IR), Scanning Electron Microscopy (SEM) and electrical characterizations are used. Results show that $SCCO_2$/co-solvents can extract porogens and remove water effectively at a significantly shorter time (≤1 hr) and at a low temperature (≤160°C) without thickness shrinkage in contrast with thermal annealing which uses 450°C and 5 hours without significantly shrinkage. $SCCO_2$/TMCS removes water and terminates silanol

group with methyl group, and hence preventing water re-adsorption which increases k. The dense layer on the sample surface that formed through the vapor treatment/HMDS helps to seal pores and prevent metal diffusion. This research also shows that patterning samples prior to porogen/water removal can minimize plasma damages on porous sample.

Chapter 1

Introduction

1.1 The Need for Low-*k* Materials

In 1965, Moore's law stated the number of transistors on a chip doubles every year. In 1975, Gordon Moore revised his law by stating the number of transistors that the semiconductor industry can place on a microprocessor chip roughly doubles about every two years. This modification with the rate of alternate year is due to the complexity of chips fabrication [1]. Figure 1-1shows that Moore's Law predicts exponential increase in the number of transistor placed on the Intel processor. The first Intel microprocessor had only 2200 transistors as compared to today's Intel microprocessor with more than 1 billion transistors.

Non-stop demand for higher performance microprocessor chip has led to reduction in device size with high number of transistor on a chip. However, shrinking the transistor size extensively tends to create new problems. The more transistor density on a single chip would consume more power, hence generating heats. The capacitive load and cross-talk between wires can also reduce the speed performance. These issues create a continuous challenge for the entire silicon industry. Thus, the semiconductor industry is

now researching a new material to produce chips that meet the high-performance and low-power consumption demands for the next-generation microprocessors [2].

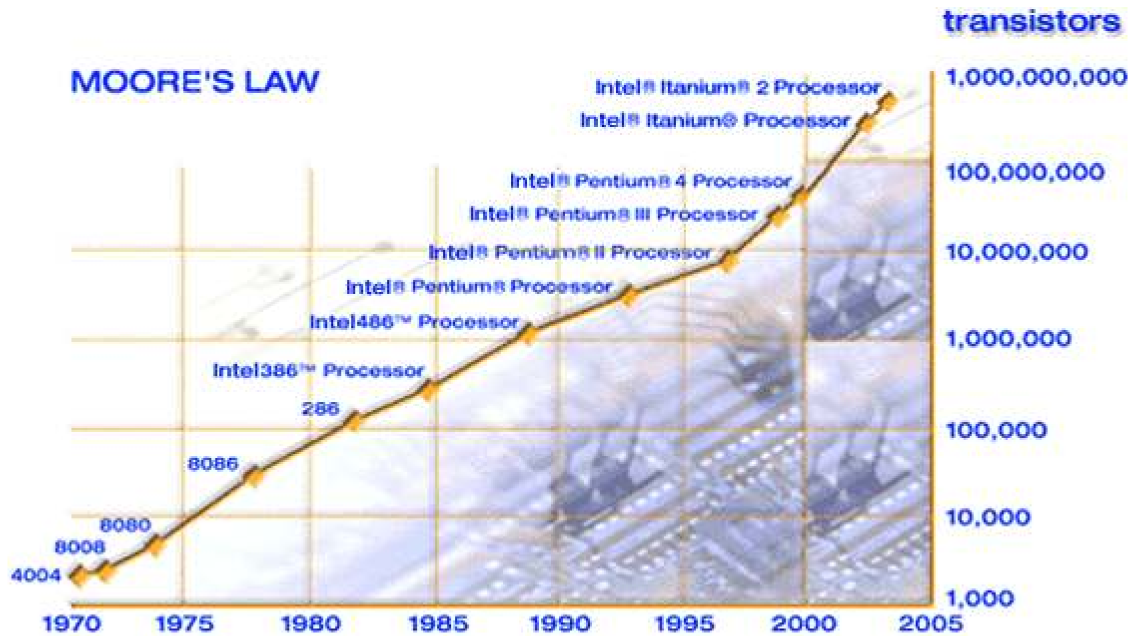

Figure 1-1. Moore's Law predicted exponential increases in the number of transistors integrated into Intel processors [Reference: www.intel.com]

A low-dielectric constant (low-*k*) material is needed to reduce the resistance-capacitance (RC) time delay and crosstalk noise at the back-end-of-line (BEOL) when device size is scaled down to sub-micron level [3,4]. Replacing aluminum (ρ_{Al} = 2.655 μΩ -cm) with Copper (ρ_{Cu} =1.678 μΩ-cm) for metal lines can theoretically reduce the RC delay by almost 37% due to its lower resistivity [5]. However, the reduction in resistivity is insufficient to further improve the RC delay. Therefore, researchers are focused on changing the insulator material (capacitance side). Substituting SiO_2 (k = 4.0) with a lower dielectric material (e.g. k = 2.0) will reduced the delay by 50%. Using lower dielectric layer also reduced the power consumption, hence less heat. As the packing

density of interconnect metal lines increases, a dielectric layer with k < 2.0 is urgently needed. The International Technology Roadmap for Semiconductors (ITRS) predicts that by year 2010, a 45 nm technology with 12 metal levels will be used [6]. One of the best ways to further reduce the k-value is by incorporating porosity (air) into the films, since air has the lowest dielectric constant (k=1) [7].

1.2 Possible material used as insulator layer

For a low-k dielectric to be able to use in current device fabrication, several requirements need to be satisfied. Some basic requirements for the desired low-k film are listed as follows:

- Possess low dielectric constant value (approaching 1)
- High glass transition temperature (if applicable)
- Low absorbance of water or contaminants
- High mechanical strength
- Ability to endure chemical mechanical planarization
- Etch selectivity over photoresist

Table 1.1 shows some of the available materials that can be used as an insulator layer. These listed low-k materials have both advantages and disadvantages. For fluorinated silicon dioxide film (F-SiO_2), some amount of fluorine atoms replace oxygen atoms in SiO_2 layer. This effect reduces the dielectric constant from ~4.0 to ~3.5. The F-SiO_2 sample is deposited via plasma enhanced chemical vapor deposition (PECVD) by incorporating fluorine directly into the precursor that is similar to tetraethocysilane (TEOS). The main disadvantage of the F-SiO_2 film is that it is a hydrophilic sample, therefore it adsorbs water and increases the k-value. Fluorinated silicon dioxide can react

and generate by product HF acid and/or fluorine based on the amount of water adsorb. HF molecules can also react with Si and give a SiF_4 byproduct, which is a gas at room temperature. This leads to device failure by changing the dielectric constant value or electrical performance. For carbon doped SiO_2 (C-SiO_2), a small amount of carbon is incorporated into SiO_2. C-SiO_2 possesses lower *k*-values (2.6 – 3.2) which is better than F-SiO_2. However, the silanol group is formed in the sample during the etch processes, hence increasing the dielectric constant value. For polymeric dielectric films, there are many materials available to use as a low-*k* film via spin-on deposition technique. The materials are polyimides, spin-on organosilicates and PTFE (Teflon). The polymer films have lower dielectric constants and are easy to deposit by using spin-on deposition technique. They are also easy to characterize. However, polymer film is a very soft material and this leads to difficulties in the next steps of integration process. The polymer requires a etch-stop to avoid or minimize damage during etch/chemical mechanical planarization (CMP). Also, spin-on polymers exhibit high thermal expansion as compared to copper and aluminum which creates cracks or delamination during heating/cooling process. A porous SiO_2 and aerogel/xerogel films consists of voids in SiO_2 molecules. In general, the pre-cursor is spin-coated on subtrate, followed by baking process to link SiO_2 together and to remove excess solvent. Highly porous dielectric materials have a major advantage in terms of their low-*k* value. However, porous dielectrics are not ready in production and many advantages and disadvantages are yet to be discovered. The property of porous film needs to be investigated, such as their reliability with chemical mechanical planarization (CMP), surface topography, water adsorption over time and pore size distribution.

Material	Dielectric constant k-value	Technique
SiO_2	4.0	Chemical Vapor Deposition (CVD)
F-SiO_2	3.2-3.6	CVD
C-SiO_2	2.6-3.2	CVD
Polyimide	3.0-3.5	Spin On (SO)
Silsesquioxanes	2.7-3.0	SO
Porous Amorphous C	2.1-2.5	CVD/SO
PTFE (Teflon)	~1.9	SO
Xerogel	1.8-2.2	SO
Aerogel	1.8-2.2	SO
Porous Organics	<2.2	SO

Table 1-1 Shows listed available low-*k* dielectric layer

1.3 Introducing porosity to lower k-value

In this research, the properties of nanoporous organosilicates thin films prepared via so-called sacrificial porosity generators (porogens) approach or inorganic-organic nanohybrid technique are investigated. These hybrids are basically phase-separated organic and inorganic poly(methylsilsesquioxane) (PMSSQ) polymers where the organic phase is entrapped between the crosslinking inorganic matrix [8,9]. Conventional thermal annealing process is typically used to volatize the sacrificial porogen, hence, creating

nanoporous thin film. Nevertheless, this conventional process has several disadvantages due to high temperature (~ 430-450°C) and long process times (up to 5 hr). The high temperature and long duration often lead to pore-collapse and thickness shrinkage. Also, the choice of organic and inorganic polymer is limited such that the glass transtition (T_g) of the organic polymer has to be lower than the T_g of the inorganic polymer [10]. An alternative extraction process at lower temperature is needed to replace the conventional thermal annealing.

1.4 $SCCO_2$ to Generate Pores

Lubguban *et al*. 2004 have shown that Supercritical CO_2 ($SCCO_2$) treatment is a good alternative as compared to thermal annealing process in porogen removal. This Gangopadhyay's group is the first group to utilized $SCCO_2$ process for pore generation in thin film. In this proposal, $SCCO_2$/co-solvents (Methyl ethyl ketone, tetrahydrofuran, and methanol) process are used to effectively remove the porogens and water in a significantly lower temperature of ≤160°C and lower time (≤1 hr). The effects of $SCCO_2$/co-solvent treatments on the processed sample are investigated via spectroscopic ellipsometry, Fourier Transform Infra-red spectroscopy and electrical characterization.

Supercritical CO_2 ($SCCO_2$) treatment is an excellent tool in generating nanoporous low-*k* thin films. At supercritical state, CO_2 possesses dual liquid-like solvating strength and gas-like diffusivity and viscosity at temperatures above 31°C and pressures above 1050 psi. Moreover, supercritical fluid has a very low (~0) surface tension to allow penetration into nanoporous materials. $SCCO_2$ is an attractive process because it is a low-cost process, is non-toxic, does not support combustion and is benign

to environment. The addition of a small amount of co-solvents or modifier can enhance the $SCCO_2$ solvating strength and extraction performance [11]. Due to these interesting properties, $SCCO_2$ has been researched vigorously in many applications such as thin metal lines deposition [12,13,14], photoresist and ash-residue removal [15,16], O_2 ash-damaged repair [17, 18,19] and porogen removal [20,21].

1.5 $SCCO_2$ Process to Solve Low-k Integration Issues

Besides challenges in generating porous film, adopting porous film also poses many difficulties in the next step of integration process. One of the many challenges in adopting porous film occurs during the photolithography process. Patterning of low-*k* porous films for Cu deposition exposes the film to oxygen-based plasma etching and plasma ashing for resist residue removal. The typical ash process causes oxygen diffuses into the film, which attacks the Si-CH_3 (methyl) group and converts it to Si-OH (silanol). This results in carbon depletion and increase of silanol groups that modify the surface properties into hydrophilic, thereby increasing the sensitivity of sample to moisture. Due to the free –OH bond, the ash-damaged porous sample will adsorb water at a faster rate as compared to a non-damaged porous sample over time. The uptake of moisture generally increases the dielectric constant value significantly, destroying the properties of the porous film.

It has been shown that silylating treatment can be used to overcome the integration process issue of porous film by several researches. Silylating agent such as Hexamethylsilizane (HMDS) and trymethylcholosilane (TMCS) can be used to repair the porous sample that undergoes the photoresist removal process. The TMCS treatment

plays two important roles in curing the porous insulator. First, it removes water from the porous dielectric. Second, it converts the sample surface by terminating Si-OH group with Si-CH_3. This phenomenon prevents water re-adsorption into the porous sample. Similar to the TMCS treatment, the HMDS treatment also can remove water and convert sample properties to hydrophobic surface functionalities. In addition, the HMDS treatment can seal the pores by forming a dense layer on the top of sample surface. This dense layer can help in preventing copper diffusion into the porous low-*k* dielectric layer. This research shows a multi-step based on $SCCO_2$ extraction process can be utilized to create nanoporous low dielectric constant thin film by removing porogen, removing water and terminating silanol group with methyl group along with pore sealing treatment via vapor treatment process.

1.6 Problems in Porous Film Characterization

Incorporating porosity in insulator layers reduces the dielectric constant values. This is desirable because it reduce the time constant RC delay. The pore size should be carefully controlled and should be smaller than the minimum features size to prevent electrical short and to achieve mechanical stability. It is also preferable to have a homogenous pore size distribution to prevent *k* anisotropy. Thus, characterizations of porous films are becoming crucial and increasingly difficult. Conventional measurement techniques have become unreliable because of very small pore sizes in the order of few nanometers.

Well-known methods to determine the pore size distribution, pore volume fraction and whether it is an open- or closed-pore structure are based in different physico-

chemical principles [22]. The available techniques can be divided into three main categories: (1) scattering techniques – small-angle x-ray spectrometry (SAXS) and x-ray reflectivity (XRR), (2) adsorption techniques – ellipsometric porosimetry (EP) and (3) positron annihilation lifetime spectroscopy (PALS). SAXS is based on diffuse scattering of x-rays from heterogeneous electron density distributions. This scattering technique is normally used in combination with XRR that gives the information of total porosity [23,24]. Adsorption porosimetry is a widely used method in characterizing pore structure [25]. EP is a combination of non-intrusive (wave propagation) and intrusive (adsorption – gas) method. The main goal of EP is to measure the optical constant of a porous material when the pores adsorp/desorp vapor with known optical constant [26,27]. PALS is based on positronium lifetime during collisions with the pore surfaces. PALS has the capability to determine the pore size distribution and to distinguish pore structure (open or closed) [28]. The techniques summarized above may be time consuming, requiring difficult sample preparation and may render the sample unusable after measurements.

1.7 VASE™ as a Good Measuring Technique to Porous Film

By using SE, important properties of the films like depth profile, thickness, refractive index and pore volume fraction can be found to understand the effects of the treatments. FT-IR results and scanning electron microscopy (SEM) imageries will be used to correlate the SE results. In this proposal, we report variable angle spectroscopic ellipsometry (VASE™, J.A. Wollam, Inc.) as a tool to investigate properties of porous films such as pore volume fraction and refractive index depth profile in addition to thickness and refractive index usually obtained by ellipsometry. The refractive index

profile is suggestive of the distribution of pores in the films. Spectroscopy ellipsometry also provides an accurate measurement of ellipsometric data which are required for adequate characterization of unknown sample. With an accurate modeling, we can determine the percentage porosity at the interface and bulk porous. We can also distinguish whether a porous sample has a graded or non-graded refractive index throughout the sample thickness. We modeled processed samples with Cauchy and Bruggeman Effective Medium Approximation (BEMA) layer. Cauchy layer is commonly used to describe a transparent layer of an insulator [29]. BEMA layer is used to calculate the porosities percentage of processed film [30]. We then converted those two layers into graded layer to examine the changes of refractive index through out the sample thickness after each treatment. We also added a surface roughness simulation on certain sample to improve the fit.

1.8 Objective of the Dissertation

The main objective of this research is to utilize variable angle spectroscopy (VASE™) as a novel means to analyse the porous film properties in a quick, effective and non-destructive technique in contrast to conventional ways. The porous films were produced in a new technique developed by IBM called porosity generator (porogen). In contrast with conventional annealing to remove porosity generators, $SCCO_2$ was used. This technique is first used by Gangopadhyay *et al*. Other treatments were also done to solve other issues in low-k films like moisture absorption, pore sealing and plasma-damaged due to photoresist ashing. The overview of this dissertation proposal is shown in the flow chart Table 1-2.

1. Films were prepared by sacrificial porogen technique: (i) Open-pore, and (ii) closed-pore morphologies.
2. These two samples were subjected to two type of porogen removal:
    a. Conventional thermal annealing
    b. Supercritical CO_2 technique
3. For thermally annealed sample, the samples were subjected to O_2-based plasma to simulate damage during photoresist removal followed by HMDS vapor treatment to cure the damage and seal pores.
4. For $SCCO_2$ processed sample, the samples were divided into two sets:
    a. Ascured plasma, followed by various $SCCO_2$ and vapor treatments.
    b. Ascured plasma exposed to plasma process, followed by various $SCCO_2$ and vapor treatment.
5. The function of various $SCCO_2$ and vapor treatments are given as follows:
    a. $SCCO_2$/MEK, Butanol, Methanol – porogen and water removal.
    b. $SCCO_2$/TMCS - termination of –OH with methyl group.
    c. Vapor treatment/HMDS – remove water and seal pore

The focus of this research is to utilize $SCCO_2$ process in preparation of nanoporous film. The $SCCO_2$ process is utilized for porogen removal, water removal, silanol group termination. All of the mentioned $SCCO_2$ process is done in sequence followed by HMDS vapor treatment to seal pores.

$SCCO_2$ process is used to remove porogen and water from nanohybrid porous film. This proposal investigates the performance of $SCCO_2$ with the addition of co-

solvents as compared to thermal annealing process in generating nanoporous film. The silylation agent (TMCS) injected in supercritical fluid is used to remove the remaining bonded water and to terminate silanol group with methyl group. This proposal studies the effects silylating agents in vapor treatment on O_2 ash-damaged porous film. The silylating agent (HMDS) in vapor treatment is used to seal pores and prevent copper diffusion.

Processed samples are characterized via variable angle spectroscopy ellipsometry (VASE™), FT-IR and Capacitance-Voltage (C-V) measurement. FT-IR and C-V measurement are fairly straight forward measurements, which mean that the output measurement describe the sample properties. However, for spectroscopy ellipsometry, it only measures the state of polarization light changes upon reflection on sample surface. It does not directly give the film properties such as film thickness, surface roughness, refractive index or non-homogeneity. A model is needed to analyze the ellipsometry data. The constructed model is then generated a set of data which is then compared with measured data. The analysis procedure is called data fitting, because the model parameters are varied to find the best fit between generated and measured data. The most common fit parameters are optical constant and thicknesses. The fitting algorithm used in VASE™ is the Marquardt-Levenberg algorithm. The root mean square error (MSE) is used to quantify the difference between the experimental and predicted data. Therefore, this proposal emphasizes analytical techniques used in modeling ellipsometry measurements of porous samples. This designed analytical technique was accepted for publication in Journal of Applied Physics (April 2006).

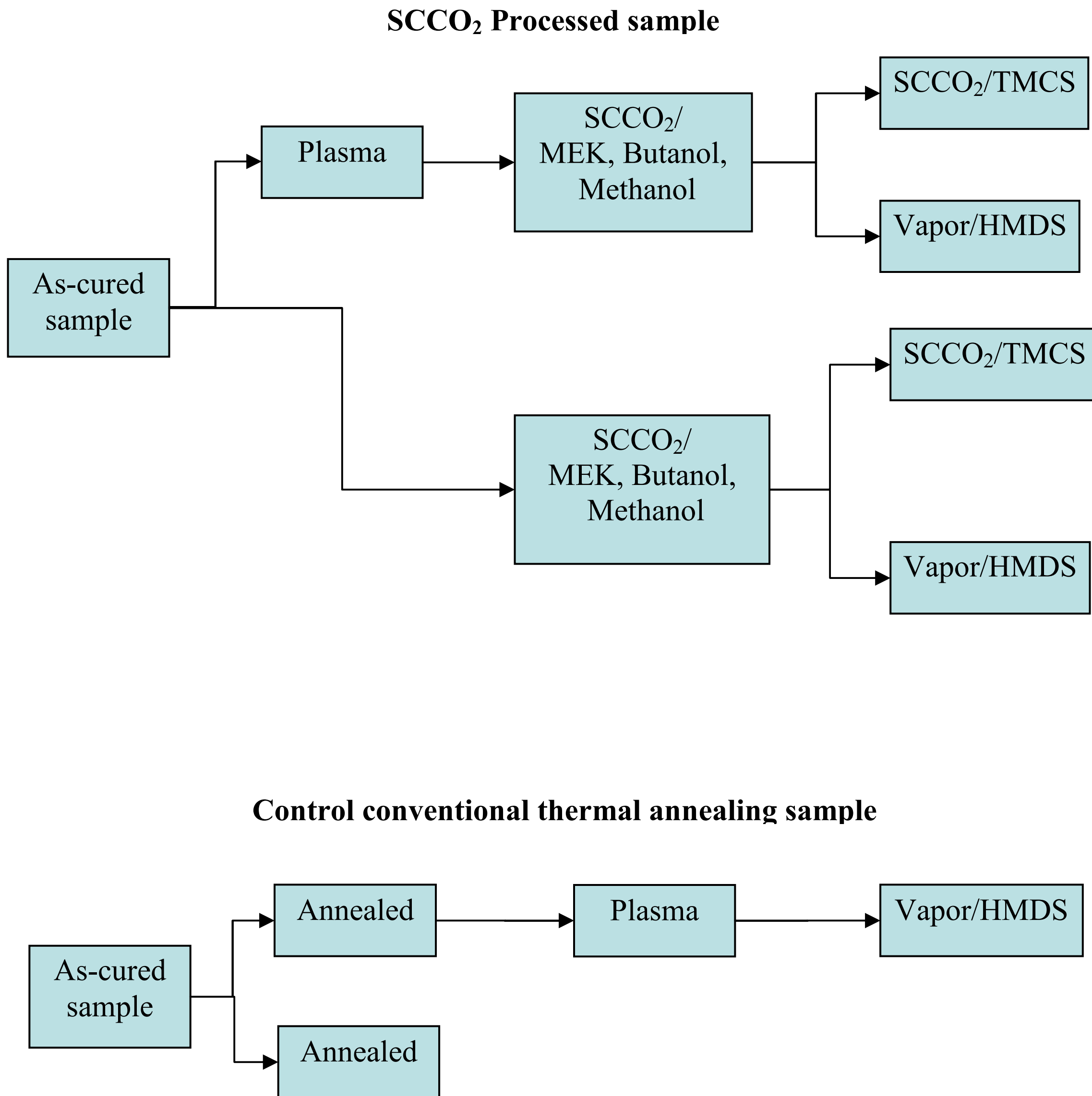

Table 1-2 Flowchart overview dissertation research work.

Figure 1-2 (a) shows the typical process flow implemented in industry for manufacture of integrated device [31]. The PPO/PMSSQ solution (dielectric material) is first spin coated on silicon, followed by porogen and water removal. Initially, this sample has good properties of nanoporous material (i.e: low-k, no water). The sample was then subjected to lithography process for patterning which includes plasma exposure for photoresist residues removal. This plasma process damages the nanoporous dielectric film. Metal were then deposited on this patterned samples followed by chemical mechanical polishing to remove the excess metal. This process flow leads to some disadvantages such as degrading the good quality of nanoporous material (increase k value, and increase water content).

In this dissertation, I am suggesting the following process flow. Similar as Figure 1a, the PPO/PMSSQ solution is coated on silicon. However, the sample is subjected to photolithography process, photoresist residue removal by plasma process, metal deposition and then CMP process. Then, in the final step, this patterned sample is subjected to porogen and water removal process creating nanoporous low-k dielectric layer. In this dissertation, it is found that this proposed process flow can reduce the damages on the nanoporous low-k film as compared to process in Figure 1-2(a).

Figure 1-2(b) shows the ascured open-pore samples exposed to plasma treatment, these processed samples were then subjected to SCCO2 treatment for porogen and water removal. These samples were divided into two for TMCS and HMDS treatment: 1- $SCCO_2$/TMCS and 2- VT/HMDS.

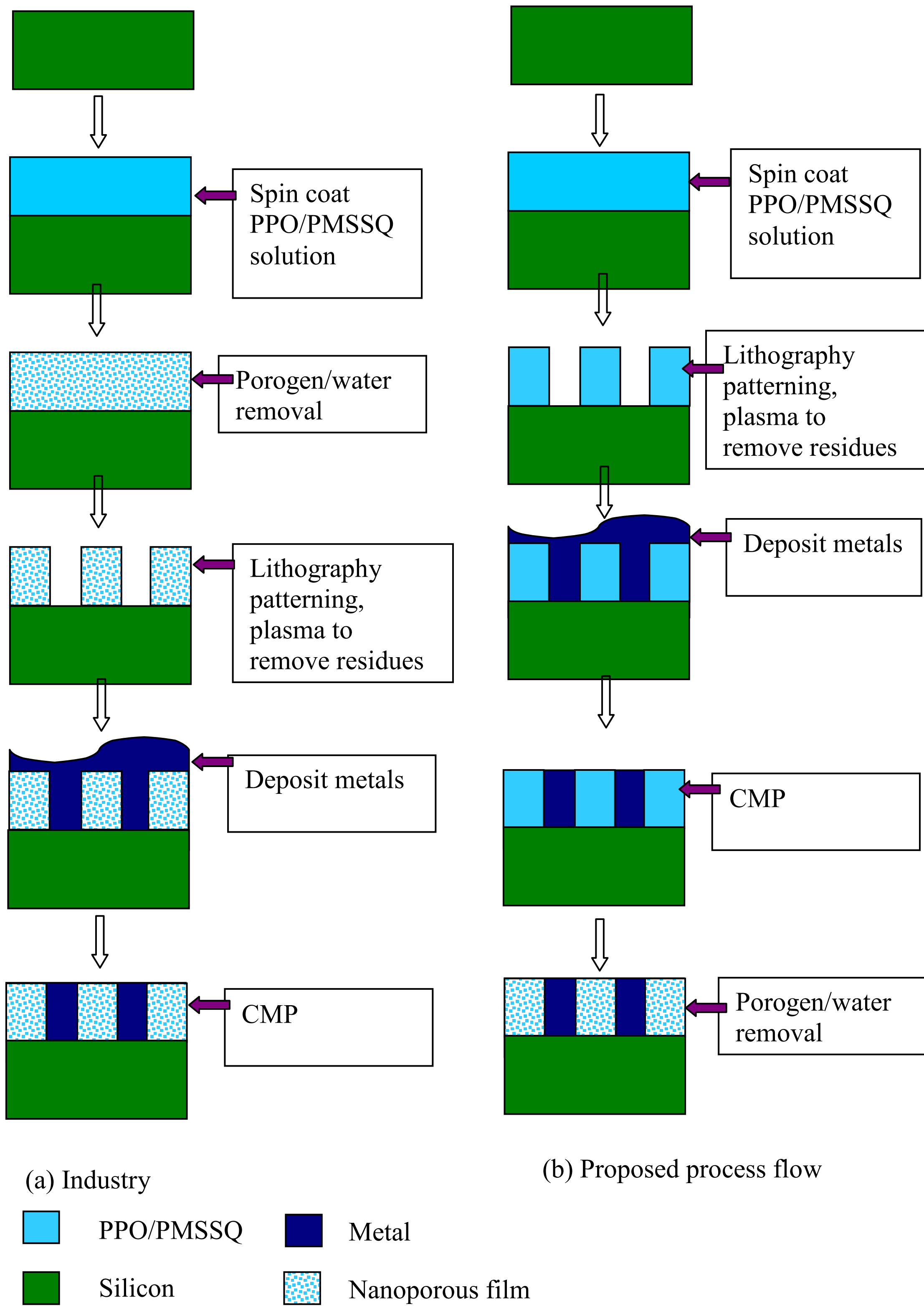

Figure 1-2 Process flow (a) industry and (b) proposed in this dissertation.

1.9 Dissertation Organization

Chapter 2 describes the definition of $SCCO_2$ and properties in supercritical fluid. This chapter presents the literature review of $SCCO_2$ treatment in preparing porous low dielectric constant thin films. It also reviews silylation (HMDS/TMCS) process via $SCCO_2$ treatment to cure plasma-damaged porous sample. This chapter describes other $SCCO_2$ applications.

Chapter 3 describes the methodology and theory background of optical and electrical characterization. This chapter first explains the theory of light in derivation of the Fresnel reflection/transmission equation at planar interface that leads to description of thin film properties. It also reviews spectroscopy ellipsometry analysis in modeling of the porous film by other research group. This section explains the designed analytical methods used in spectroscopic ellipsometry modeling for various types of porous films (i.e: single layer, bi-layer, graded single layer and graded bi-layer). In addition, this chapter briefly explains FT-IR and also C-V measurements.

Chapter 4 explains the fabrication of nanoporous organosilicate thin films via the sacrificial porogen approach. This chapter describes the porous samples used in this research (i.e: open-pore and closed-pore). It also explains conventional thermal annealing procedure to remove porogen. This chapter describes various modes (static, dynamic and static/dynamic) of the $SCCO_2$ process, high pressure $SCCO_2$ experimental system, experimental procedure and experimental parameters.

Chapter 5 presents the results and discussion obtained from this research. This chapter reviews the implemented spectroscopy ellipsometry analytical method for characterizing different type of porous film (i.e: single layer, bi-layer, graded single layer

and graded bi-layer). It also discussed thermal annealed and SCCO2 processed sample in generating nanoporous film. This chapter studied the effect of HMDS vapor treatment on nanoporous organosilicates film using spectropscopy ellipsometry. This chapter also discussed the results of the plasma exposure (for patterning process) prior to porogen/water removal process.

Chapter 6 presents conclusion and future directions of this research.

Chapter 2

Literature Reviews

2.1 Supercritical CO_2 Process to Generate Porous Film

Supercritical CO_2 is CO_2 with unique properties by employing properties in between a gas and liquid. Figure 2-1 is a pressure-temperature (P-T) phase diagram that shows the phase transition of CO_2. The phase of CO_2 refers to its form that is uniform in chemical composition and physical state, for instance a solid phase, liquid phase and gas phase. A phase transition refers to a spontaneous transition from one phase to another phase such as a solid phase converts to a liquid phase or a solid phase converts to a gas phase. This phase transition occurs at a certain temperature and pressure. The P-T diagram shows the three lines describing melting, sublimation and boiling line in which refers to the gas, solid and liquid phase. These lines are phase boundaries separating different region of phases. Along the line, the two phases are co-existed. For example, the two phases of liquid phase and gas phase are existed in the boiling line. Same goes to sublimation line, both solid phase and gas phase existed. In other word, the two phases are separated and can be distinguished from each other along these lines at certain temperature and pressure.

As the temperature and pressure increase, CO_2 reaches a point called critical point. Critical temperature (Tc) is the highest temperature in which CO_2 gas can be converted to liquid as pressure increases. Critical pressure (P_c), on the other hand, is the highest pressure at which liquid phase can be converted to gas phase as temperature increases. CO_2 is known as in its supercritical state at any temperature above Tc and pressure above Pc. There is only one phase exists, which is called the supercritical fluid. At this stage neither liquid phase nor gas phase existed in supercritical region. The CO_2 supercritical fluid possesses both properties of gas and liquid. At this region, no matter how much temperature is applied, CO_2 fluid in this region will never boil and no matter how much pressure is applied, CO_2 fluid in this region will never condense. Supercritical CO_2 occurs at temperature above 31°C and pressure above 1050 pounds per square inch (psi).

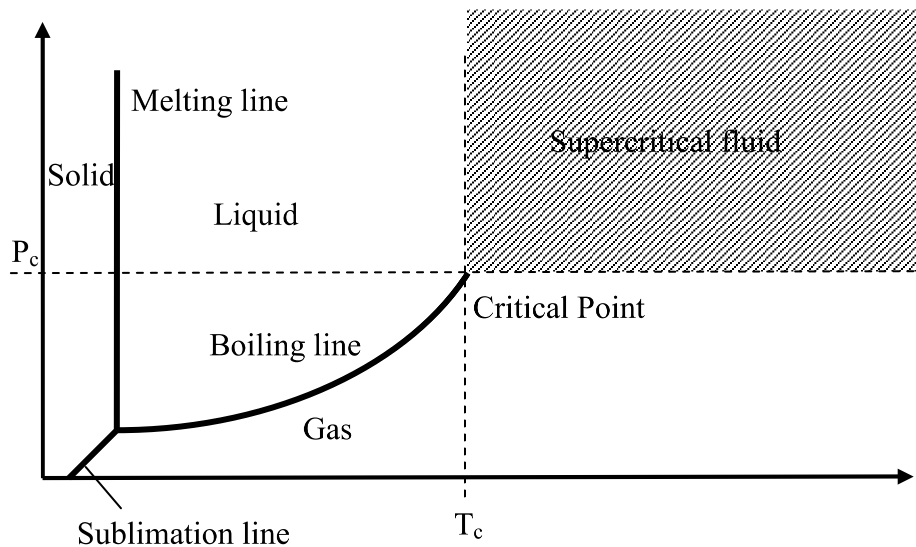

Figure 2-1. A phase diagram showing the different phase and supercritical region.

For a better understanding of the difference between supercritical state and any other states, the comparison between liquid-vapor transitions at a constant pressure (open vessel) and a constant volume (closed sealed vessel) is reviewed. Figure 2-2 illustrates the behavior of CO_2 heated in both open and closed sealed vessel. In an open vessel, the liquid is vaporized freely into the surrounding as the temperature increases. At this moment, the interface between vapor and liquid are still exist. This condition is known as boiling. In a close sealed vessel, boiling process does not occur. Instead, the vapor density increases as temperature increases, but the liquid density decreases. Similar to the open vessel, the phase boundaries or interface between vapor and liquid are still exist at this stage. This process is known as vapor treatment. However, as the temperature and pressure continue to rise, the vapor and liquid density become closer and closer to each other until it reach the critical point where there is no phase boundary between the two. At this point, the liquid-gas line or phase boundaries disappear and there is no interface between the two. This condition is known as supercritical treatment.

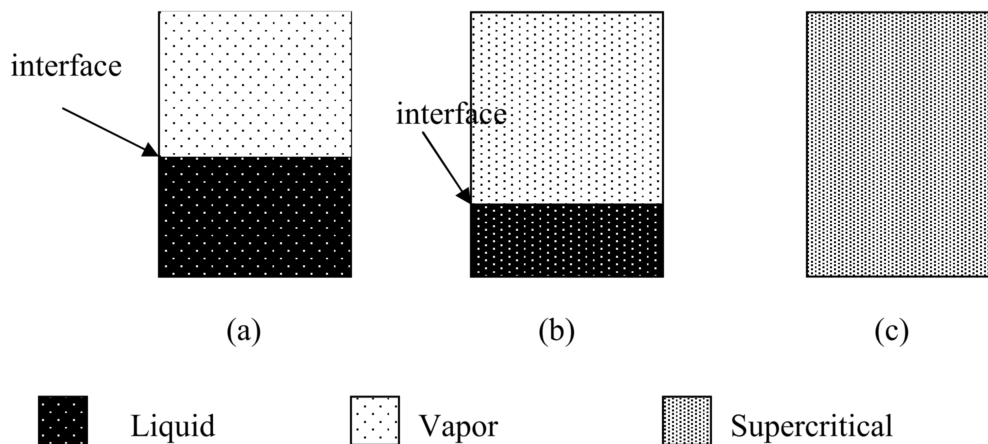

Figure 2-2 The behavior of CO_2 in open and closed sealed vessel.
(a) A liquid in equilibrium with its vapor [boiling process] (b) Liquid heated in sealed container [vapor treatment] (c) Liquid heated in sealed contained above the critical temperature and critical pressure [supercritical treatment].

Supercritical fluid (SCF) exhibits both properties of gases and liquids. Supercritical fluid has high solvent strength due to its liquid-like density characteristic. In addition to that, SCF exhibits gas-like transport properties of diffusivity and viscosity. The diffusion coefficient (cm/s^2) is somewhere in the middle of gases and liquid and viscosity(g/cm-sec) is similar to the gases Moreover, supercritical fluid have very low (~0) surface tension allowing facile penetration into microporous materials. Table 2-1 shows typical physical properties of gas, liquid and supercritical fluids in the orders of magnitude. It can be seen that viscosity of SCF is closer to the viscosity of gas. Also, diffusivity of SCF is somewhere in between gas and liquid. The density of SCF is closer to liquids.

	Density (g/ml)	Diffussion coefficient (cm^2/sec)	Dynamic Viscosity (g/cm-sec)
Gas	$1x10^{-3}$	$1x10^{-1}$	$1x10^{-4}$
Liquid	1	$5x10^{-6}$	$1x10^{-2}$
Supercritical Fluid	$3x10^{-1}$	$1x10^{-3}$	$1x10^{-4}$

Table 2-1. Physical properties of a gas, liquid and supercritical fluid.

Supercritical CO_2 is a good solvent to dissolve nonpolar solids; however it can not dissolve polar molecules. Adding a small amount of polar compounds can enhance the solvating power of $SCCO_2$. The substance that is incorporated into supercritical system is known as co-solvents or modifiers. This co-solvent, which is a liquid under ambient condition, has been used intensively to alter $SCCO_2$ solvating properties. With the

addition of particular co-solvent, a supercritical process can be customized into certain application. Supercritical CO_2 process is an advantageous from environmental stand point of view because CO_2 gas is inert, relatively non-toxic, does not support combustion, cheap, commercially available in high purity and is not an ozone depleting compound. Furthermore, there are no excess used liquid after $SCCO_2$ process as compared to aqueous cleaning.

Lubguban *et al*. (2004) demonstrated a $SCCO_2$ process for the preparation of nanoporous organosilicated thin films. The supercritical CO_2 for porogen extraction was performed without co-solvents at pressure of 7000 psi and temperature of 200°C for 14 hour. Films with both open- and closed- pore structure were studied. These researches show that the thicknesses of the two samples remained the same after the $SCCO_2$ process. Based on the multiple Gaussian curve fitting of FT-IR analysis, the percentage porogen removal of closed- and open-pore film was found to be 85% and 92% respectively. This proved that $SCCO_2$ is a promising tool in fabricating nanoporous thin film. It is believe that adding appropriate co-solvents into $SCCO_2$ system and using static/dynamic $SCCO_2$ mode will enhance porogen removal efficiency.

Similar as Lubguban *et al*. (2004), Rajagopalan *et al*. (2003) presented his work in Applied Physics Letter to describe $SCCO_2$ treatment for porogen removal, hence creating nanoporous film. Two set of sample prepared via sacrificial porogen approach: (1) open- and (2) closed-pore sample. These samples consisted of phase-separated porogen that entrapped between crosslinked PMSSQ matrix. This performance porogen removal via $SCCO_2$ treatment was compared with high temperature thermal annealing. It was found that SCCO2 treatment can extract porogen at temperature less than 200°C; whereas, the

conventional thermal annealing process for porogen decomposition occurred at high temperature of 430°C.

Lubguban et al. (2002) showed a $SCCO_2$ treatment to extract unbonded and loosely bonded low molecular weight and CO2 soluble species in creating voids for low-*k* film. The experiment parameters are pressure of 8650 psi and temperature of 200°C for 8 hours. In this experiment, the matrix films used were composed of organosilicates and of a low molecular weight a-C:F. These samples were deposited by plasma enhanced chemical vapor deposition with C_4F_8 (gas), tetravinyltetramethylcyclotetrasiloxane (liquid) and H_2 (gas). This research found $SCCO_2$ process can extract low molecular weight species (CF) or larger CO_2-soluble species containing CF_x moieties. This reduced the dielectric constant value of the material from 2.87 – 2.48.

Xie and Muscat (2004) investigated SiO-H condensation on porous methylsilsesquioxane film using co-solvents dissolved in $SCCO_2$ process. Three types of co-solvents were used: molecules with polar functional groups, non-polar functional groups and low vapor pressure. $SCCO_2$ with addition of alcohol as co-solvents is found to remove hydrogen-bonded silanols and replace it with isolated silanol on surface efficiently. For example, methanol contains polar functional groups (O-H) that bond with polar water molecules and increases the solubility of water in the supercritical fluid phase and reacts with silanol group. It is shown that $SCCO_2$ with addition of methanol removed silanol group significantly.

Pai *et al*. (2004) prepared mesoporous silicate films using preorganized templates in supercritical fluids. A block co-polymer template containing hydrophobic and hydrophilic block is spin-coated on substrate. Upon drying and annealing to induce

microphase separation, the template is exposed to supercritical fluid. A solution metal alkoxide is used as precursor in $SCCO_2$ to diffuse into the template and react selectively with hydrophilic segments to form metal oxide network. The catalyst is localized in the hydrophilic segments without reacting with hydrophobic domains. The by-product of alkoxide condensation is carried away by CO_2. Finally, the sample is taken out from supercritical system. The template is then removed via calcination and degradation in reactive plasma to create mesoporous structure.

2.2 Supercritical or Vapor Treatment with HMDS to Repair Porous Film

Capani *et al*. (2005) observed intrusion rate of hexamethyldisilazane (HMDS) during $SCCO_2$ process functionalization of triethoxyfluorosilane (TEFS - xerogel based film). The difference between $SCCO_2$/HMDS processed at pressure 2500 psi and temperature of 40°C versus samples processed at 2500 psi and 60°C were studied. At higher temperature, there were less silylation as compared to lower temperature such that the depth penetration is lesser. This research showed that the depth penetration of HMDS via $SCCO_2$ into porous film is not significant. However, supercritical fluids did offer an effective means of repairing ash damage to porous low-*k* film. By reacting the silanols with HMDS silylating agent in supercritical fluid, it increased the film hydrophobicity and removed adsorb water.

Reidy and Matz (2005) demonstrated the performance of supercritical process with addition of silylating agent (HMDS) in repairing the damaged low-*k* film and

sealing pores. The O_2 ash-damaged underwent two sets of $SCCO_2$ processing conditions. First, the samples were reacted under pressure of 2700 psi and temperature of 60°C in a clean room environment. Second, the experiment was performed under pressure of 1400 psi and temperature of 40°C (not in a clean room environment). At a lower pressure process (1400 psi), the contact angle increased up to 63° and saturated within 1 minute. At high pressure process, the contact angle increased up to 50° within 1 minute and continued to increase as a function of time. The surface carbon species was examined via x-ray photoelectron spectroscopy (XPS). From the XPS analysis, it is found that there is a significant loss of carbon species (i.e. methyl group) during oxygen plasma and an increased of carbon species during silylation process. The $SCCO_2$/HMDS process incorporated trimethylsilyl ((CH_3)Si-O-) group at the surface. Dynamic secondary ion mass spectroscopy analysis demonstrated that the depth of the silylation repair is very limited. As the time of HMDS exposure increases, no change in carbon depth profile was found. This may due to the initial surface silylation that block further diffusion of HMDS into pores, and thus prevent reactions with silanol deepers inside the film.

Orozco-Teran *et al*. (2003) studied the effects of $SCCO_2$ in combining with silylating agents (HMDS) on O_2 ash-damaged MSQ sample. Films were exposed to oxygen plasma at certain time interval, which simulate varying degrees of damage. The $SCCO_2$/HMDS process was performed at pressure of 1200 psi and temperature of 60°C for 1 minute. Based on SEM imageries, a loss of 40 nm thickness is found after oxygen plasma ashing. However, the increase in thickness is recovered after silylation process due to the reactions with Si-OH in the ash-damaged porous film. The thicknesses before plasma, after plasma and after $SCCO_2$ silylation are given as 533 nm, 491 nm and 520 nm

respectively. $SCCO_2$/HMDS also allows the porous films to withstand subsequent wet etch processes without significant material loss. A thickness loss (~14 nm) occurs after the HF wet etch treatment of O_2 plasma-damaged sample. However, there is no significant thickness changes perceived for the $SCCO_2$/HMDS treated films. The hydrophobic of sample surface may permit the reaction of the HF solution with the porous film.

Mor *et al*. (2002) studied a repair of plasma damage in porous organosilicates (POSG) films using HMDS vapor treatment. Methods of film properties characterization used in this study are N&K analyzer 1200, FT-IR spectra and C-V Keithley Model 82 (at 1 MHz). N&K analyzer is a film thickness measurement using the knowledge of film reflectance spectrum. HMDS vapor treatment was performed at 80°C for 15 min at a pressure of 760 Torr. Three samples were investigated: POSG film without plasma treatment, POSG film with plasma treatment and POSG film with plasma treatment followed by HMDS vapor treatment. Mor *et al.* also showed the POSG film properties changes with O_2 plasma treatment time duration. The thickness of POSG film decreases with the increased of O_2 plasma exposure time (30s, 60s and 90s). The sample –OH contained also increases with time. The decrease in film thickness is due to the reduction of methyl group which caused by O_2 plasma process. This is confirmed by FT-IR results. The O_2 plasma is an excellent oxidant which oxidize methyl group. Mor *et al*. believed that O_2 radicals can diffuse into porous film reacting with methyl group and replacing it to hydroxyl group. The removed of the function methyl group from porous film degrades dielectric of POSG. To overcome this problem, HMDS vapor treatment is performed to convert –OH group to methyl group. After the HMDS treatment, it is found that methyl

group in sample increased as well as film thickness. Film thickness is increased by 20 nm. Mor *et al*. believed the increase in thickness after the HMDS treatment is due to two reasons. First, the incorporation of Si-CH_3 group when HMDS reacts with Si–OH groups. Second, the deposition of HMDS species set on the film surface. The authors concluded that this HMDS vapor treatment reduced –OH group, increased methyl group and improved film dielectric constant.

Gorman *et al*. (2004) studied a rapid repair of plasma damage in low-*k* dielectrics films using $SCCO_2$ process. Plasma damage degrades quality toward wet etch process. This is undesirable because it increases water absorption; hence increases the dielectric constant value. Gorman *et al*. compared the performance of curing plasma ash-damaged sample via silylation process at supercritical state and under ambient pressure process. The silylation process passivated plasma-damaged surface by changing the sample properties from hydrophilic to hydrophobic. This passivated surface exhibits enhanced resistance toward wet etches processes owing to the nature of hydrophobic. Characterization methods of film properties for this study were spectroscopic ellipsometry (Variable Angle Spectroscopy Ellipsometry - J.A. Woollam Co., Inc), FT-IR and contact angle measurement. The $SCCO_2$ experiment was performed at pressure of 1400 psi and temperature of 40°C. The silylating agent used was HMDS mixed with Hexane. Hexane is a good solvent due to its low supercritical pressure (1200 psi) and high HMDS solubility. In this experiment, $SCCO_2$/solvents process was found to increases contact angle to 90° within 1 min process. However, under ambient pressure process required 12 - 24 h to increase contact angle to 90°. After silylation $SCCO_2$

process, it is found that the processed sample is resisted towards HF wet etches with no significant thickness changes.

2.3 Supercritical or Vapor Treatment with TMCS to Repair Porous Film

Lahlouh *et al*. (2004) studied the $SCCO_2$ process with the addition of butanol treatment to remove silanol group followed by silylation via $SCCO_2$ with TMCS to restore methyl group in O_2 plasma-damaged porous samples. The experiment was done at pressure of 7000 psi and temperature of 150°C. First, the O_2 plasma-damaged porous samples underwent $SCCO_2$ process with 7 injections of Butanol. Each butanol injection was lasted for 5 minutes. Thus, Butanol is discovered to increase both the polarity of the supercritical fluid and the solubility of water. Second, the silylation process was done with 3 injections of TMCS. Each TMCS injections was lasted for 30 minutes. It is found that TMCS treatment has successfully replaced silanol groups with alkylsilyl.

Xie *et al*. (2004) dissolved alkyldimethylmonochlorosilanes (silylation agents) in supercritical fluid to cure oxygen plasma-damaged porous sample. Three silylation agents were used: TMCS, butyldimethylcholorosilane (BDMCS) and octyldimethylcholorosilane (BDMCS). The supercritical fluid processes were performed at pressure of 2100 – 4300 psi and temperature of 50°C – 60°C. Among the three agents, TMCS performed the cleanliness without forming a physisorbed layer and generated the largest reduction in dielectric constant values. After TMCS treatment, a strong peak at 1068 cm^{-1} show that TMCS react with silanol group and convert it to siloxane (Si-O-Si)

bonds. This research also showed that adsorption of surface SiOH band at 3745 cm^{-1}, 3400 $cm^{-1}$and 942 cm^{-1} were decreased along with the increased in methyl absorption at 2964 cm^{-1} (CH_3 asymmetric) and 2906 cm^{-1} (CH_3 symmetric). This is due to the replacement of silanol group with methyl group. Xie *et al*. claimed that TMCS is an excellent molecule to repair damaged film, however owing to its short 1 carbon chain length it is not expected to seal pores.

Liu et *al*. (2002) studied a repair of plasma ash damage film by hydrogen plasma and TMCS vapor treatment. Three samples were prepared in this experiment: as-cured POSG film, POSG followed by O_2 plasma, POSG plasma treated followed by furnace degassing, POSG plasma treated followed by TMCS vapor treatment and two-step recipe. The two-step recipe consists of H_2 plasma and TMCS vapor treatment. Prior to O_2 plasma, the as-cured POSG sample underwent H_2 plasma, followed by O_2 plasma and finally TMCS vapor treatment. Hydogen plasma was performed to passivate the inner porous structure. This step prevented porous film to adsorb polar contamination and also to protect the inside pores against the oxygen radicals penetration. It is found that furnace degassing and TMCS vapor treatment technique does not remove water efficiently. Large amount of –OH contained left after those 2 treatments contributed to high *k*-value. The two-step recipe provided the best result. There are no water contained is found in sample and its dielectric constant is low (*k*=2).

Chang *et al*. (Journal of Vaccuum Science and Technology) (2002) and Chang *et al*. (Journal of The Electrochemical Society) (2002) investigated a repair of plasma ash damaged porous film by TMCS vapor treatment. Methods of film properties characterization used in this study are N&K analyzer 1200, FT-IR spectra and C-V

Keithley Model 82 (at 1 MHz). TMCS vapor treatment was performed at 60°C for 25 min at a pressure of 760 Torr. Five samples were prepared: ascured POSG film, POSG followed by plasma treatment, POSG plasma treated followed by TMCS treatment, POSG with wet stripper dipping and POSG wet stripper dipped followed by TMCS treatment. It is found that TMCS can convert Si-OH to Si-O-Si$(CH_3)_3$ group for both O_2 plasma ashed sample and wet stripper dipped sample. The sample surface became more hydrophobic with reducing moisture uptake in porous sample.

2.4 Other applications using supercritical fluid technology

Martinez *et al*. (2003) showed that supercritical process can be used as a cleaning fluid to remove any contaminants in porous methylsilsesquioxane film. The porous MSQ blanked is subjected to immersion in deionized (DI) water for the purpose of testing the drying effectiveness of $SCCO_2$. The $SCCO_2$ static/dynamic (or pulsation) mode was performed in this research. The pulsation term in Martinez's work, refers to the quick ramp down of pressure from 3200 psi to 1500 psi for a time less than 15 seconds, then a quick repressurization back up to the 3200 of starting pressure. It is found that static/dynamic (pulsation) method works well in drying the porous sample.

Gougousi *et al*. (2005) demonstrated supercritical fluid can be used in depositing metal oxide including Al_2O_3 and ZrO_2 where the metal organic precursor and oxidizing agents were delivered in liquid into $SCCO_2$ system. Gougousi discovered that hydrogen peroxide is a viable O source for oxide deposition. The $SCCO_2$ solvation properties were found to aid in the delivery of precursors and in the removal of by-products for advanced low-temperature processing of oxides.

Cabanas *et al*. (2004) studied the deposition of gold film in supercritical fluid system. The high-purity gold films were deposited onto metal, ceramic and polymer substrates. The supercritical CO_2 static mode was performed at pressure of 2200 psi and temperatures between 60°C and 125°C. Gold was also deposited in silicon trench giving a homogenous deposition. Ye *et al*. (2005) utilized supercritical CO_2 to selectively deposit copper and palladium onto silicon substrate.

Chapter 3

Methodology and Theory of Optical and Electrical Characterization

3.1 Overview

Variable angle spectroscopy ellipsometer (VASE™) [J.A. Woollam Co.] is used to characterize optical properties of processed films (optical constant, thickness and refractive index depth profile). A Nicolet 4700 Thermo Electron Corporation Fourier Transform Infrared (FT-IR) is utilized to study the structural properties of film. Capacitance-Voltage (C-V) measurement is used to measure the capacitance value of porous insulator layer, hence calculating the dielectric constant value. This chapter overview basic concept on how do ellipsometer work, ellipsometer configuration, reflection/refraction at planar interface and technique of VASE™ analysis. Spectroscopy ellipsometric models used in describing processed porous film are discussed. This chapter also reviewed basic theory of FT-IR absorption and Beer-Lambert law. The quantitative analysis technique by using multiple Gaussian curve fitting is also explained.

3.2 Variable Angle Spectroscopic Ellipsometry

Spectroscopic ellipsometry is an attractive method because it is noncontact, non destructive and does not require sample preparation. Many material properties can be characterized such as: thin film thickness (single or multilayer), pore volume fraction, depth profile of material properties, surface and interfacial roughness. Thin film thickness, optical constant and porosity are commonly used in this research. The combination of incident angles and spectroscopic measurement allow the user to acquire large amount of data from the sample. Hence, ellipsometry has advantages in researching optical constant of new materials.

3.2.1 Basic concepts: How do ellipsometers work?

Ellipsometry involves the light making a reflection from the surface of interest. Figure 3.1 shows the important optical physics of ellipsometry. In general, the incident or incoming beam from a light source is hitting on sample surface. The light suffers multiple internal reflections within film thickness and reflected off from the sample to detector. The reflected light is analyzed for its changes of polarization state. These incident and reflected beam that lie one the same plane are known as Plane of Incidence (POI). The electric field wave of the incident light beam, which is typically a linearly polarized, can be decomposed into two vector components. The two vector components are characterized as parallel to the plane of incidence (E_p) and perpendicular to the plane of incidence (E_s). These vector components are referred to as *p*-wave and *s*-wave. The

subscript p and s stand for German word, "parallel" and "senkcrecht" respectively. Similar to the incoming beam, the electric field of the reflected or transmitted beam are also decomposed into p-plane and s-plane components [29].

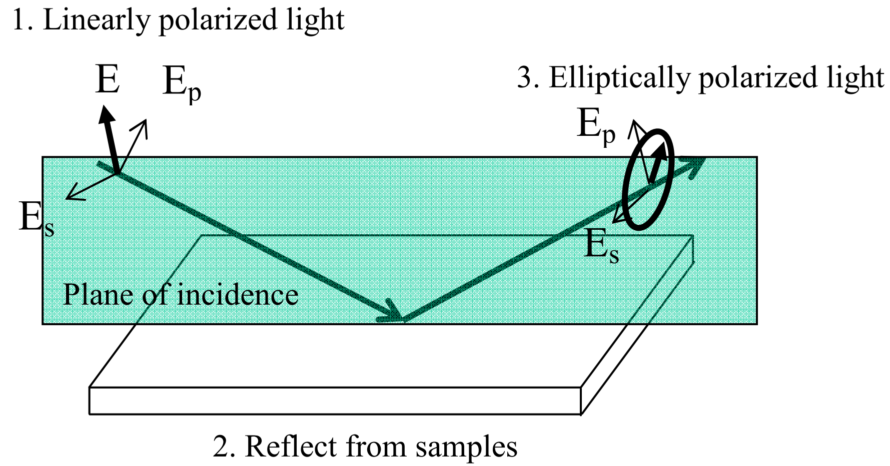

Figure 3-1. Interaction of polarized light with sample of interest.

The fundamental equation of ellipsometry is based on the changes of the polarization state from incoming and reflected off the surface. Spectroscopic ellipsometry measures Ψ and Δ values as a function of wavelength and incident angle [32]. These numbers are related to the complex Fresnel coefficient for p and s polarized light.

$$\rho = \frac{R_p}{R_s} = \tan(\Psi)e^{i\Delta} \qquad \text{[Eqn. 3-1]}$$

Where,

Rp and Rs are the total reflection coefficients for a plane wave polarized light parallel (p) and perpendicular (s) to the plane-of-incidence, respectively [33,34].

Ψ is the amplitude of total Fresnel reflection coefficient,.

Δ is differential phase change upon reflection, $\Delta=\delta_{rp}-\delta_{rs}$

The mathematical expression of *Rp* and *Rs* are derived from Maxwell's equations for electromagnetic radiation that applied to the boundary between dissimilar materials related to the Fresnel reflection coefficient and layer thickness; hence, interrelated with optical constant of materials [35, 36 and 37].

3.2.2 Ellipsometer Configuration

Ellipsometer is an optical instrument used to measure polarization states changes upon reflection. An ellipsometer consists of several optic components that come with many different set of configurations. All ellipsometer configurations consist of four basic optic devices element: light source, polarizer, analyzer and detector. The five main ellipsometer configurations are: Rotating Analyzer Ellipsometer (RAE), Rotating Polarizer Ellipsometer (RPE), Rotating Compensator Ellipsometer (RCE), Polarization Modulation Ellipsometer (PME) and Null ellipsometer. The RAE is utilized to analyze the samples in this work. The differences between each of the ellipsometer configurations are beyond the scope of this work. The details are well described in ellipsometry and polarized text book [38]. Thus, a brief description of the optics devices used in building an ellipsometer is illustrated in this section.

First – light source, spectroscopy ellipsometry requires a broad spectrum light. There are several light sources available and each of the light sources provides different spectrum of wavelength. For example, Xenon lamp covers 190 nm – 2 um spectral range (UV-VIS-NIR), Quartz Tungsten Halogen provides 350 nm – 2 um spectral range (VIS-

NIR) and Silicon Carbide Globar covers 1.5 um – 40 um (NIR-IR). Among all these light sources, Xenon lamp is installed in the ellipsometer for this work. Second – monochromator is used to convert an arbitrary light into a specific wavelength. Third – polarizer is used to transform any form of lights polarization state into linearly polarized light. Fourth – compensator is typically used to convert a linearly polarized light into circularly polarized light. The compensator retarder works by retarding the phase 90° or ¼ wave. Fifth – analyzer is used to analyze the output state of polarization light. Sixth – detector is used to measure the intensity of light that passing through the analyzer. Figure 3.2 shows the ellipsometer configuration (Variable Angle Spectroscopy Ellipsometer) used in this research.

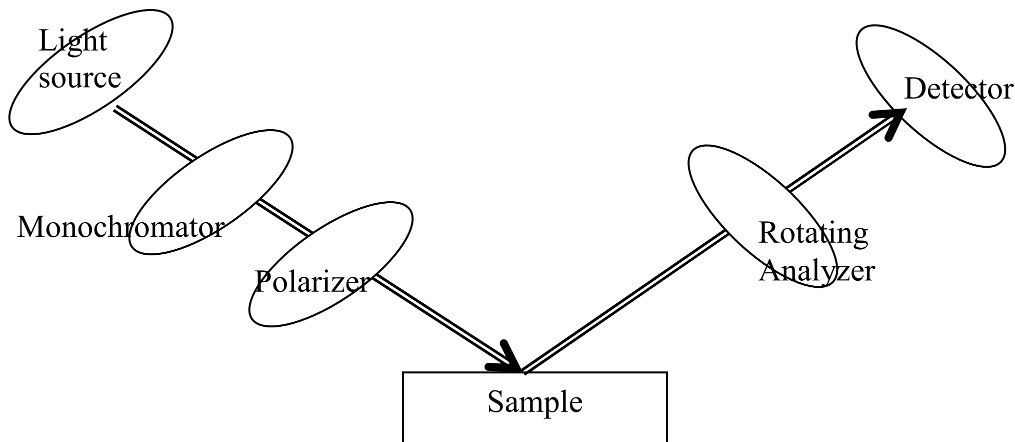

Figure 3-2. Rotating Analyzer Ellipsometer, Variable Angle Spectroscopy Ellipsometer VASE™ (J.A. Woolam Co. Inc.) used in this work.

3.2.3 Reflection/refraction at the planar interface

In order to make use of the ellipsometer measured data to describe the optical properties of thin film, electromagnetic theory should be used to derive reflection and

transmission coefficient in terms of its amplitudes and phase. These coefficients contain information of optical properties the film. Huge amount of theoretical work on derivation electromagnetic theory of light have been done in depth in many text book and papers [29, 35, 38]. In order to understand how ellipsometry work, it is important to understand a basic knowledge on how the light interacts with matters, leading to derivation of reflection and transmission coefficients.

Notations used in ellipsometry are introduced. Wave propagating in isotropic medium can be described as a complex index of refraction. It contains a real and imaginary number given as:

$$N = n + jk \qquad \text{[Eqn. 3-2]}$$

Where n is the index of refraction describing the ratio of phase velocity (v) within a material to the speed of light in vacuum (c=3x10^8 m/s), n=c/v. k is the extinction coefficient describing the amount of light being absorb by the material. The light intensity decreases as it travels through an absorbing material. The decrease in the light intensity per unit length z can be described as:

$$I(z) = I_0 e^{-\alpha z} \qquad \text{[Eqn. 3-3]}$$

Where,

I_0 is the light intensity before it hits the film surface

α is the absorption coefficient.

The extinction coefficient, k is related to the absorption coefficient, α given as:

$$k(\lambda) = \frac{\lambda}{4\pi}\alpha \qquad \text{[Eqn. 3-4]}$$

k is in the function of wavelength. Electric field vector traveling in a plane can be described as below:

$$E = E_0 e^{j(\omega t+\delta)} e^{-j\omega \frac{N_z}{c}} \quad \text{[Eqn. 3-5]}$$

By inserting equation [$n+jk$], the above equation can be re-written as:

$$E = E_0 e^{j(\omega t+\delta)} e^{-j\omega \frac{n_z}{c}} e^{-j\omega \frac{k_z}{c}} \quad \text{[Eqn. 3-6]}$$

where,

δ is a constant phase angle,

c is the free-space wave velocity

Eo is the general complex contains both amplitude and phase

Next, we reviews reflection and refraction occurs when incident light from medium *0* hit on another medium *1*. Figure 3-3 shows two materials with two different properties such as N_1 and N_2. The incoming beam at angle θ_i hitting on sample surface will reflected off at angle θ_r. Some of the incoming beam will refracted into the medium *2*. The total electric field inside medium *0* and medium *1* must obey the Maxwell's equation and satisfy the boundary conditions at the interface. First, the direction of all electric vectors (incident, refracted and transmitted) must lie on the sample plane, POI, perpendicular to the sample surface. Second, incident and reflected light must obey Law of Reflection such that the incident angle of incoming beam must equal to the incident angle of reflected light ($\theta_i = \theta_r$). Third, the relationship between the angles and refractive index (N) for both medium *0* and medium *1* for electric field traveling in isotropic medium can be described by Snell's Law, given as:

$$N_1 \sin\theta_1 = N_0 \sin\theta_0 \quad \text{[Eqn. 3-7]}$$

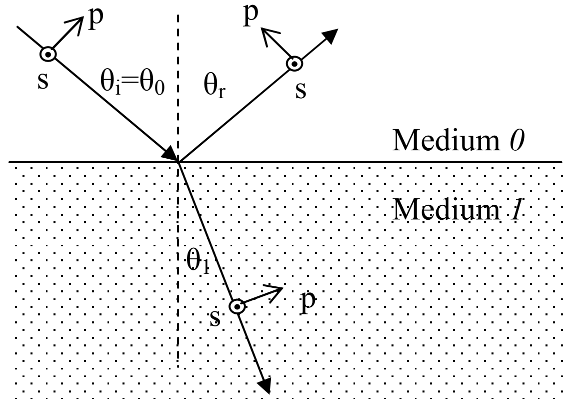

Figure 3-3. Illustrates oblique incident, refracted and reflected beam on planar surface from medium *0* to medium *1*.

As mentioned earlier, the incoming beam can be decomposed into two electric vector components, *p*-wave and *s*-wave. For an incoming electric vector vibrating perpendicular (*s*-wave) to the POI, the reflected and transmitted waves are also vibrating perpendicular to the POI. Same goes for incoming electric vector vibrating parallel (*p*-wave) to the POI, the reflected and transmitted waves are also vibrating parallel to the same plane. The complex amplitude of the component electric vectors of incident, reflected and transmitted for each of *p*-wave and *s*-wave is related to the index of refraction (N_x) and angles (θ_x) and given as:

$$r_p = \frac{E_{rp}}{E_{ip}} = \frac{N_1 \cos\theta_0 - N_0 \cos\theta_1}{N_1 \cos\theta_0 + N_0 \cos\theta_1} \quad \text{[Eqn. 3-8]}$$

$$r_s = \frac{E_{rs}}{E_{is}} = \frac{N_0 \cos\theta_0 - N_1 \cos\theta_1}{N_0 \cos\theta_0 + N_1 \cos\theta_1} \quad \text{[Eqn. 3-9]}$$

$$t_p = \frac{E_{tp}}{E_{ip}} = \frac{2N_0 \cos\theta_0}{N_1 \cos\theta_0 + N_0 \cos\theta_1} \quad \text{[Eqn. 3-10]}$$

$$t_p = \frac{E_{tp}}{E_{ip}} = \frac{2N_0 \cos\theta_0}{N_0 \cos\theta_0 + N_1 \cos\theta_1} \quad \text{[Eqn. 3-11]}$$

Where $r_{p \text{ or } s}$ and $t_{p \text{ or } s}$ are known as Fresnel Reflection and Transmission coefficients, respectively. By using Snell's Law equations r_p, r_s, t_p, t_s can be simplified in terms of amplitude and phase.

$$r_{p/s} = |r_{p/s}| e^{j\delta_{rp/rs}} \quad \text{[Eqn. 3-12]}$$

$$t_{p/s} = |t_{p/s}| e^{j\delta_{tp/ts}} \quad \text{[Eqn. 3-13]}$$

Where,

$|r_p|$ and $|r_s|$ is the ratios of amplitudes reflected over incident wave for *p*-wave and *s*-wave, respectively, and

δ_{rp} and δ_{rs} is the phase shift upon reflection for *p*-wave and *s*-wave, respectively.

Spectroscopy ellipsometry is based on polarization changes of incident light and reflected light on a material. This leads to the determination of the complex Fresnel reflection coefficients ratio *p*-wave over *s*-wave.

$$\rho = \frac{r_p}{r_s} \quad \text{[Eqn. 3-14]}$$

Or also known as,

$$\rho = \tan\psi e^{i\Delta} \quad \text{[Eqn. 3-15]}$$

Where,

$$\tan\Psi = \frac{|r_p|}{|r_s|}, \text{ and} \quad \text{[Eqn. 3-16]}$$

$$\Delta = \delta_{rp} - \delta_{rs} \qquad \text{[Eqn. 3-17]}$$

Ψ determines the differential amplitude changes of incoming wave upon reflected wave by the electric vector components vibrating parallel and perpendicular to the POI. Δ measures the phase different upon reflection between *p*-wave and *s*-wave.

The objective in spectroscopy ellipsometry equations is to relate the complex amplitude of the incident wave to reflected/refracted wave vector components. The interactions of incoming wave components from ambient (medium *0*) to a film (medium *1*) with t_1 thickness deposited on a substrate (medium *2*) are shown. For a simple case, the film is assumed to have parallel-boundaries between both interfaces (i.e: film-air and film-substrate). Next, the substrate is assumed to be a thick adsorbing material (not transparent) such that the refracted light that transmitted into the substrate will never reflected off to detector.

Figure 3-4 shows the physical pictures that described the behavior of electric vector components within a film. The incoming oblique incident wave from ambient (medium *0*) on a material medium *1* resulted in multiple internal reflections within parallel-plane boundaries (medium *1*-medium *0* and medium *1* – medium *2*). Two things occurred when wave hit on the film-air interface. Part of wave component is reflected off (r_{01}) on the same medium *0* (air) and part of it is refracted into the film (t_{01}). These wave vector components (incident, reflected and refracted) can be described by Fresnel reflection/transmission equations. Next, the refracted wave inside film thickness suffers multiple internal reflections. At film-substrate interface, part of wave component is refracted into the substrate (t_{12}) and part of the wave is reflected off (r_{12}). At the film-air interface, part of wave is refracted (t_{01}) into air and reflected off (r_{01}). The interfaces are

not purely reflecting, thus at film-substrate and film-air interface, the light is leaked (refracted). This phenomenon will keep occurring, results in multiple internal reflections within film thickness. The partial waves refracting out to air will goes to detector.

Spectroscopy ellipsometry measures the output wave reflected/refracted off from the film itself known as the total reflected amplitude. This total reflected amplitude is the sum of partial waves leading to the infinite geometries series, given as:

$$R = r_{01} + t_{01}t_{10}r_{12}e^{-j2\beta} + t_{01}t_{10}r_{10}r_{12}^{2}e^{-j4\beta} + t_{01}t_{10}r_{10}^{2}r_{12}^{3}e^{-6j\beta} + \ldots \qquad \text{[Eqn. 3-18]}$$

Where,

r_{xy}, and t_{xy} are the Fresnel reflection and transmission coefficient,

β is the film phase thickness,

$$\beta = 2\pi\left(\frac{t_1}{\lambda}\right)N_1 \cos\theta_1 \qquad \text{[Eqn. 3-19]}$$

t_1 is the film thickness (medium 1),

N_1 is the complex index of refraction of film, and

λ is the wavelength.

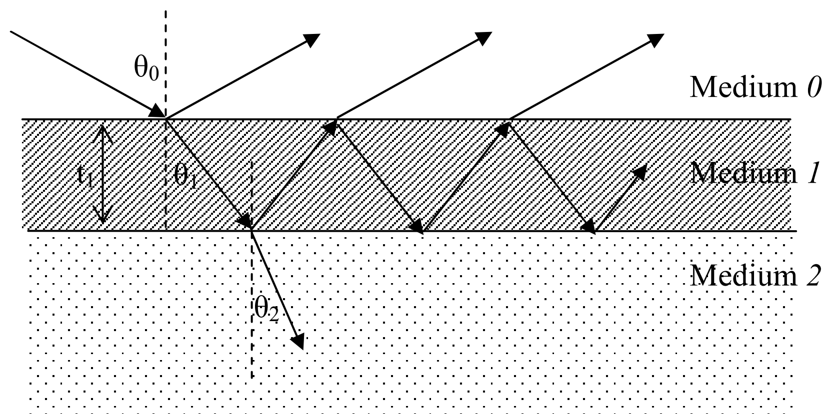

Figure 3-4. Incident beam refracted into film resulted in multiple internal reflection and reflected out to medium *0*.

3.2.4 Variable Angle Spectroscopic Ellipsometry (VASE™) Measurement and Analysis

Spectroscopy ellipsometry does not directly measure the above properties like refractive index or pore volume fraction but it measures Ψ and Δ., it is necessary to perform a model dependent analysis of the measured Ψ and Δ to extract these parameters [44]. After the data are acquired over the desired spectral range at different incident angles, the models for the optical structure of the substrate and sample are constructed. Then, the Fresnel equations based on the model are used to predict the expected Ψ and Δ values and compared to the measured Ψ and Δ values.

Figure 3-5 shows the flow chart of spectroscopy ellipsometry data analysis. First, spectroscopy ellipsometry measurement of unknown sample is taken to give the information of Ψ and Δ as a function of wavelength and incident angles. The Ψ and Δ data are analyzed in order to obtain optical constant, thickness and other desired thin film properties. A model is then constructed to describe the measured samples by supplying an initial guess of thickness and optical constant to describe the properties of the unknown film. Based on this model, Ψ and Δ values of the same wavelength and angle of incidence with the measured values are generated. The measured and generated data are then compared using a comparator function – the mean square error (MSE) given as:

$$MSE = \frac{1}{2N-M}\sum_{i=1}^{N}\left[\left(\frac{\Psi_i^{\text{mod}} - \Psi_i^{\text{exp}}}{\sigma_{\Psi,i}^{\text{exp}}}\right)^2 + \left(\frac{\Delta_i^{\text{mod}} - \Delta_i^{\text{mod}}}{\sigma_{\Delta,1}^{\text{exp}}}\right)^2\right] = \frac{1}{2N-M}\mathrm{X}^2 \qquad \text{[Eqn. 3-20]}$$

Where,

N is the number of Ψ and Δ data points,

M is the number of variable parameters in the model, and

σ is the standard deviation of the i-th data point.

The good fit between the measured and generated data is desirable in ellipsometry analysis. It shows that the build model provides correct information of the processed sample's optical properties such as: thickness, refractive index or surface roughness information.

Details and source code for implementing Levenberg-Marquardt algorithm is described in other research paper [39]. The important element of the fitting procedure is the curvature matrix given as:

$$\alpha_{kl} = \sum_{i=1}^{N}\left[\frac{1}{\sigma_{\Psi,i}^2}\frac{\partial\Psi_i^{\text{mod}}}{\partial a_k}\frac{\partial\Psi_i^{\text{mod}}}{\partial a_l} + \frac{1}{\sigma_{\Delta,i}^2}\frac{\partial\Delta_i^{\text{mod}}}{\partial a_k}\frac{\partial\Delta_i^{\text{mod}}}{\partial a_l}\right] \qquad \text{[Eqn. 3-21]}$$

The curvature matrix is related to the covariance matrix such that $C=[\alpha]^{-1}$. Once the final fit parameters have been determined, the standard 90% confidence limit (SCL) and the figure of merit (FOM) are used to describe the confidence limit of the ith fit parameter that is given as:

$$SCL_i = 1.65\sqrt{(C_{ii})} \qquad \text{[Eqn. 3-22]}$$

$$FOM_i = SCL_i \times MSE \qquad \text{[Eqn. 3-23]}$$

WVASE32® is an ellipsometry analysis software that generates the confidence limit FOM value after each fitting procedure. This FOM value is also known as error bar. The error bars obtained from this work are: ±0.1 for thickness, $\pm 5x10^{-5}$ for refractive index, and $\pm 1x10^{-2}$ for porosity.

Measurement or experimental data of unknown sample.

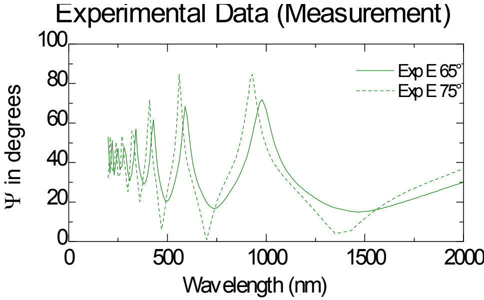

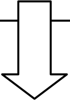

Create model to best describe the properties of unknown sample.

Cauchy	900 nm
Silicon	1 mm

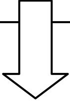

Generate Ψ and Δ (related to Fresnel Reflection/Transmission Coefficients) values from the build model.

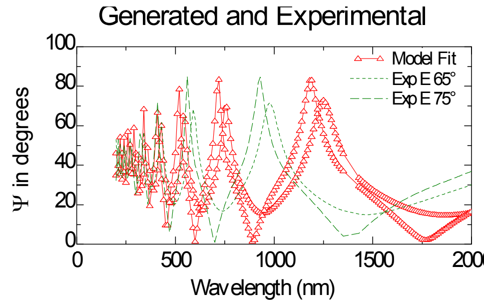

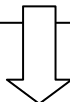

Fit the generated data with measured data.

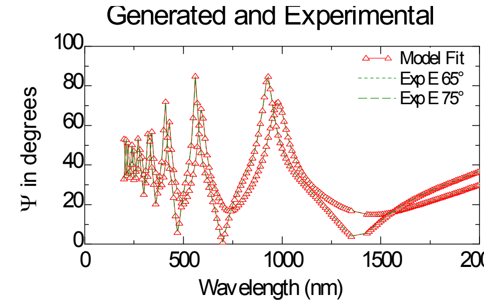

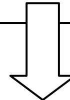

Results. Extract optical properties from build model.

Thickness = 705 nm,
Refractive index = 1.44
Surface roughness = 0
Grading layer = none

Figure 3-5. Flow chart of spectroscopy ellipsometry analysis.

3.3 Analytical method using spectroscopy ellipsometry to characterize thin film

3.3.1 Cauchy layer

The Cauchy dispersion relation is used to model transparent materials, such that the refractive index n decreases with an increase of wavelength. The Cauchy equation can be expressed as follows: [29,35]

$$n(\lambda) = n_0 + \frac{n_1}{\lambda^2} + \frac{n_2}{\lambda^4} \qquad \text{[Eqn. 3-24]}$$

where n_0, n_1 and n_2 are known as Cauchy coefficients. n_0 is the constant that dominates $n(\lambda)$ for long wavelengths, n_1 controls the curvature of $n(\lambda)$ in the middle of the visible spectrum and n_2 influences $n(\lambda)$ to a greater extent in shorter wavelengths. The parameters n_0, n_1, n_2 and thickness of the film are used to calculate Ψ and Δ values.

3.3.2 Bruggeman Effective Medium Approximation (BEMA) layer

BEMA is a model based on the intermixed composites made up of uniform cells, which all together fit the space completely [40]. The BEMA layer provides a method to combine two sets of optical constants together and the percentage of the mixture. The optical constants used for the porous film studied here are dense PMSSQ ($n_{\mathrm{PMSSQ}} = 1.39$) and air ($n_{air} = 1.0$). The Bruggeman expression is given as [41]:

$$f_a \frac{\varepsilon_a - \varepsilon}{\varepsilon_a + 2\varepsilon} + f_b \frac{\varepsilon_b - \varepsilon}{\varepsilon_b + 2\varepsilon} = 0$$ [Eqn. 3-25]

where, ε is the effective dielectric function of the composite material. ε_a and ε_b are the dielectric functions of phases a and b in their pure forms. $f_{(a \text{ or } b)}=n_{(a \text{ or } b)}/(n_a+n_b)$ are the volume fractions of the material *a* and *b*. Based on equation [Eqn. 3-25], the complex dielectric function of each material is required to calculate the percentage of the mixture using BEMA theory. The optical constants can be presented both in the form of complex dielectric form ($\hat{\varepsilon} = \varepsilon_1 + i\varepsilon_2$) and complex refractive index ($N = n + ik$), where *i* is the imaginary number [36]. The relationship between the complex dielectric function and the complex refractive index is given as follows:

$$\hat{\varepsilon} = N^2 = (n + ik)^2$$ [Eqn. 3-26]

Figure 3-6 shows the schematic representation of BEMA theory. Bruggeman expression describes particles of both material a and b mixed in random basis that is embedded in the host material. Thus, the host is now a mixture of material a and b.

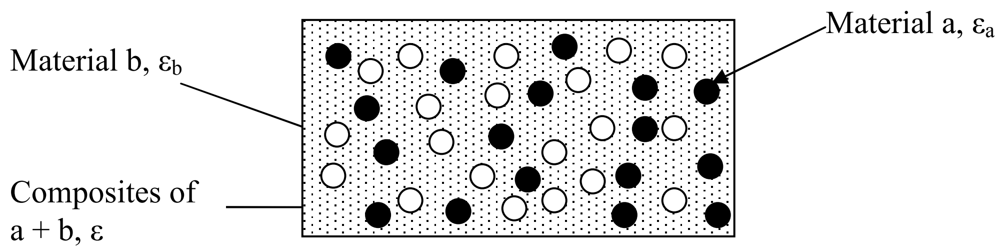

Figure 3-6. Illustrates schemative representative of Bruggeman Effective Medium Approximation theory.

3.3.3 Graded layer

The graded layer is used to simulate a film that does not have a homogenous optical constant throughout film thickness (i.e. from film-substrate interface to film-air interface). This graded model works by generating a series of thin homogenous layers with optical constants that change slightly in each layer. Figure 3-7 shows the schematic representation of (a) single non-graded layer and (b) graded layer. The graded model sliced the layer into certain number of sub layers (i.e.: N_1, N_2, N_3 … N_{500}). The optical constant of each thin layer is independent of each other.

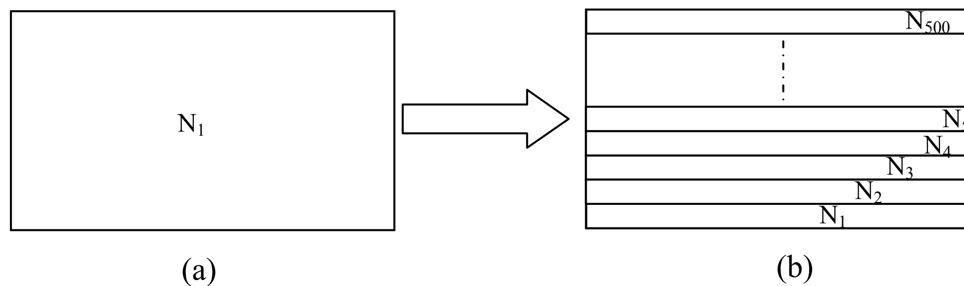

Figure 3-7. Shows the schematic representative of (a) single layer and (b) graded layer to describe a film.

3.3.4 Surface roughness

Surface roughness model is a BEMA model. It consists 50% of air (n=1) and 50% of film properties. Figure 3-8 illustrates the surface roughness on top of a film. Surface roughness model assumed a separate surface roughness layer from the film layer by drawing a parallel line in between the surface roughness and film. Both surface roughness and film has independent thickness value and optical constant.

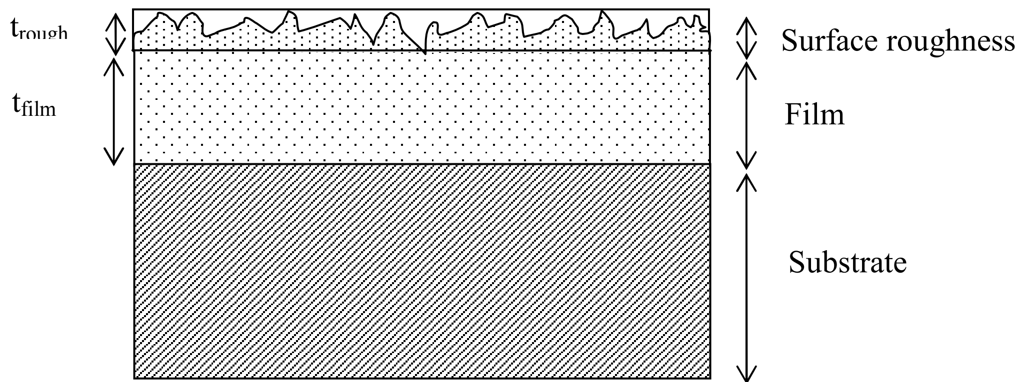

Figure 3-8. Illustration of surface roughness on film.

3.3.5 Silicon substrate

For the silicon substrate, we chosed the silicon optical constants by Herzinger *et al*. 1998 which cover a broader range (188 – 6200 nm) [42]. Similar optical constants were obtained by Jellison and Aspnes from the Palik's handbook can also be used [43]. The choice of optical constants depends on the wavelength range.

3.4 Ellipsometry Modeling for Porous Film

Himchinschi *et al*. (2002) and (2001) used variable angle spectroscopy ellipsometer (VASE™ J.A. Woollam Co.) to study the effect of treatment with HMDS on porosity of silica xerogel film. The ellipsometer spectra were taken in the spectral range of 250 nm to 800 nm at 5 nm step interval. The spectra were taken with four set of incidence angles– 60°, 70°, 75° and 80°. Cauchy layer is used to model the porous film and Lorentz-Lorenz effective medium approximation is utilized to calculate percentage

porosities. The porosity value decreases after HMDS treatment may due to the transformation of Si-O-Si$(CH_3)_3$ groups into Si-O-Si (siloxane) groups. The reduction of porosity after HMDS treatment leads to the reduction in refractive index as well [44,45].

Alvarez-Herrero *et al*. (2001) used a rotating-polarizer spectroscopic ellipsometer (SOPRA, Model ES-4G) to study adsorption water on porous Vycor glass. The ellipsometric measurement was taken in 400 – 835 nm spectral range and at 55° and 70° incident angles. Alvarez-Herrero *et al*. claimed that porous Vyvor glass has some degree of surface roughnesss. Thus, the amount amount of water adsorbed near the external surface supposedly should be greater than that adsorbed inside the porous sample. A rigorous ellipsometric model should include surface roughness and a certain inhomogeneity in refractive index through out the sample thickness. However, Alvarez-Herrero *et al*., did not include in homogeneity in refractive index and surface roughness in his ellipsometric model under assumptions that porous Vycor glass is isotropic (homogenous) and its surface is not rough to simplify ellipsometric calculations [46].

3.5 Fourier Transform Infrared (FT-IR)

Fourier Transform Infrared (FT-IR) spectroscopy is a technique derived from the vibration of the atoms of a molecule to analyze unknown components of the samples. Molecules that make up a sample are composed of atoms that bond together, where these atoms are always moving or ‘vibrating’. The intensity of this vibration increases when the molecule absorbs infrared radiation. An infrared spectrum is commonly found by passing through infrared radiation through a sample. A detector will detect the amount of incident radiation absorbed by molecule at a particular energy. The location of where the

absorption peak occurred refers to the frequency of vibrations of certain molecule of samples. The quantitative analysis in FT-IR spectra is crucial in analyzing processed sample.

3.5.1 Absorbance, Lambert-Beer's Law

Figure 3-9 illustrates an example of an infrared radiation with intensity I_o entering the sample. Some of the infrared is absorbed by sample molecules and transmitted out to detector with intensity of I. The length of the sample is given as l.

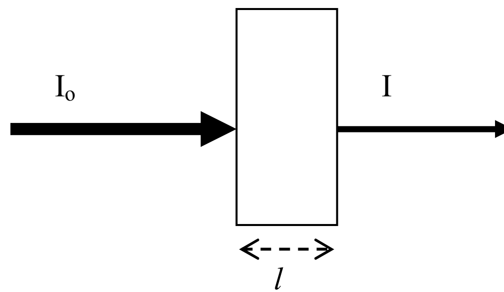

Figure 3-9. A simple absorption experiment showing some incident light is been absorbed by sample.

According to the Beer-Lambert law, the absorbance is proportional to the length of the sample thickness and to the concentration of the absorbing sample given as [47]:

$$A = \log\left(\frac{I_0}{I}\right) = \varepsilon \cdot c \cdot l \qquad \text{[Eqn. 3-27]}$$

Where

I is the intensity of the radiation entering the sample,

I_0 is the intensity of the radiation emerging from the sample,

ε is the molar absorption coefficient or molar absorptivity,

c is the molar concentration of the absorbing sample,

l is the thickness of sample,

The Beer-Lambert law given in Eqn 3-27, can be rewritten in terms of napierian logarithms ($\log e$ or ln):

$$A = \ln\left(\frac{I_0}{I}\right) = \kappa \cdot c \cdot l \qquad \text{[Eqn. 3-28]}$$

Where,

κ is the molar (napierian) absorption coefficient.

There are some cases where concentration value of the sample is unknown. If that is the case, then Eqn. 3-28 can be re-written as:

$$A = \ln\left(\frac{I_0}{I}\right) = \alpha \cdot l \qquad \text{[Eqn. 3-29]}$$

In an absorbing medium, the decrease in intensity I per unit sample length l is proportional to the value of I [29, 47]:

$$\frac{dI(l)}{dl} = -\alpha I(l) \qquad \text{[Eqn. 3-30]}$$

Solving this integration equation yields to:

$$I(l) = I_0 e^{-\alpha l} \qquad \text{[Eqn. 3-31]}$$

This equation can be simplified to:

$$\alpha = -\frac{1}{l}\ln\left(\frac{I}{I_0}\right) \qquad \text{[Eqn. 3-32]}$$

Simplify Eqn. 3-32 natural log to log base 10 gives:

$$\alpha = -2.303\frac{1}{l}\log\left(\frac{I}{I_0}\right) \qquad \text{[Eqn. 3-33]}$$

Or;

$$\alpha = 2.303\frac{1}{l}\left(\log\left(I_0\right) - \log\left(I\right)\right) \qquad \text{[Eqn. 3-34]}$$

A relationship between absorption and transmission is given as follows:

$$A = \log\frac{1}{T} \qquad \text{[Eqn. 3-35]}$$

Where,

T is the transmission value.

Transmission is defined as ratio of transmitted light through sample thickness over incident radiation of light:

$$T = \frac{I}{I_0} \qquad \text{[Eqn. 3-36]}$$

IR spectrum can be plotted in many ways and some of most common method to plot IR spectrum is either in absorption or transmission. Figure 3-10 illustrates typical graph for absorption and transmission FTIR. The presentation of IR spectral regions can be plotted in terms of wavelength as meters such as: 1 Å = 10^{-10}m, 1 nm = 10^{-9} m, 1 μm = 10^{-6} m. Another common unit used in IR spectral regions is in terms of wavenumber, υ in cm^{-1}. The relationship between wavenumber and wavelength in meter is given as:

$$\upsilon = \frac{c}{\lambda} \qquad \text{[Eqn. 3-37]}$$

Where,

c is the velocity of light (3 x 10^8 ms^{-1})

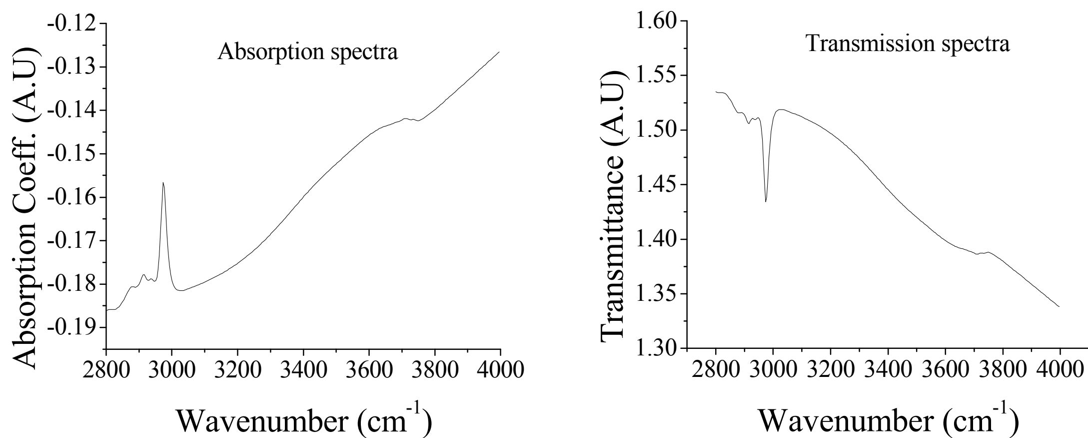

Figure 3-10. Comparison FT-IR spectra between (a) absorption and (b) transmission as a function of wavenumber (cm^{-1}).

3.5.2 Quantitative spectral analysis

Once the FT-IR spectrum is recorded, the next stage is interpretation of FT-IR spectrum. The absorption band appeared on the spectrum is assigned to a particular part of molecules within the film of interest (i.e. water, methyl group) which is known as a group frequency. In this research, a film is deposited on silicon substrate. It is important to compensate background absorption (silicon) by utilizing subtraction technique. Two FT-IR measurements are required to analyze the absorption band of film alone: (1) the infrared spectrum of silicon only and (2) the infrared spectrum of film deposited on silicon. The film spectrum is then subtracted from the silicon spectrum. The subtraction process is carefully done by making sure that the subtraction results of the two spectra yield ~0 value at the silicon absorption peak (620 cm^{-1}). At this stage, the subtracted absorption spectrum is solely based on the film alone which will be analyzed.

Table 1 listed the corresponding pertinent absorption bands that can be detected in the processed sample. After identification of group frequency, a quantitative infrared analysis can be carried out by performing a baseline correction on absorption spectra of film. The baseline correction is done by producing the flat parts of the absorption spectra. Figure 3-11 shows an example of a baseline correction spectra. The quantitative analysis can be used to calculate the percentage removal in the overall film composition. For instance, it can provide the information of how much porogen or water has been removed from the inorganic-organic nanohybrid film. Quantitative values for the specific absorption band (i.e. methyl group or water group) can be accomplished via multiple Gaussian curve fitting procedures. Figure 3-12 illustrates multiple curve fitting procedure of FT-IR spectra.

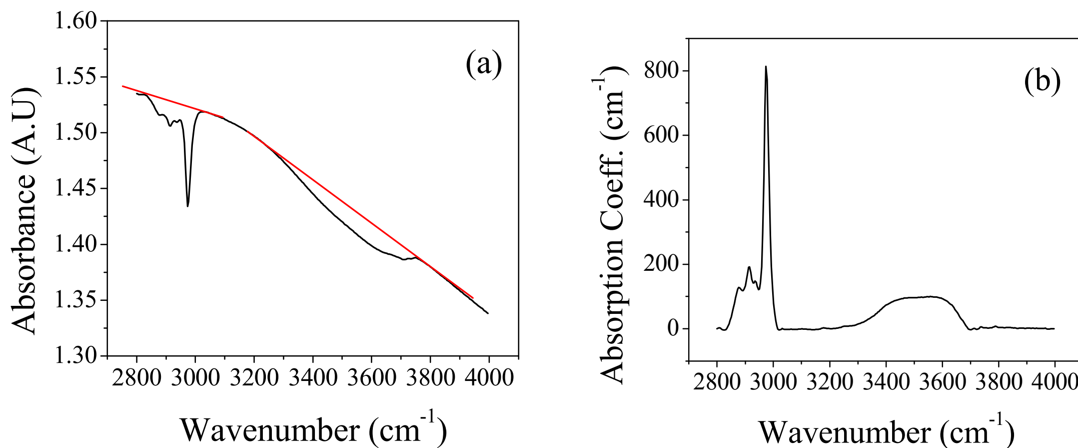

Figure 3-11. Example of FT-IR spectra (a) baseline construction and (b) baseline corrected.

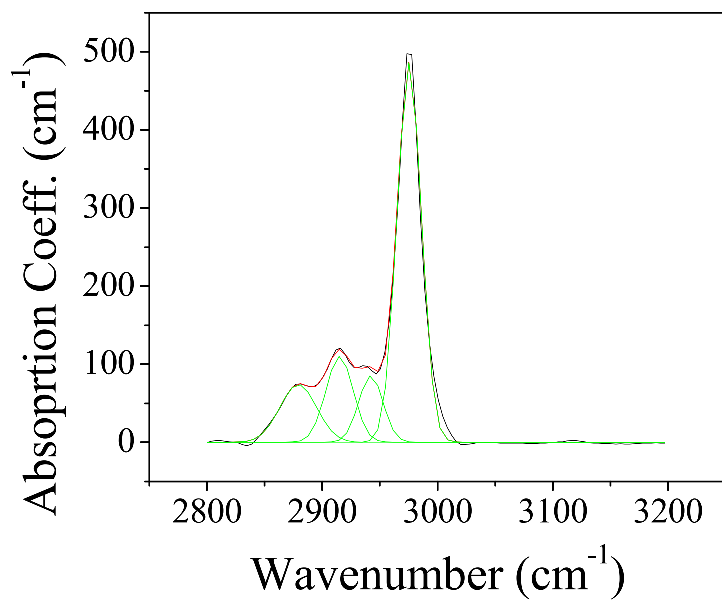

Figure 3-12. Demonstration of multiple Gaussian curve fitting of FTIR spectra.

Active bond	Position (wavenumber cm^{-1})	Description: Bond type
A. Water peak	3000-4000	
Narrow band	3600-3750	Silanol groups: (i) isolated (ii) geminal (iii) vicinal
Si-OH (isolated or geminal)	3749	Isolated / geminal
Si-OH (vicinal) Broad band	3655 3000-3600	Vicinal Physically adsorbed free water on the surface of the pores
B. Methyl group	2800-3000	
CH_3 symmetric CH_3 asymmetric CH_2 symmetric CH_2 asymmetric Si-O-Si Si-CH_3	2906 2964 2830-2855 2920-2925 1060 1240-1280	 Siloxane

Table 3-1. Selected FT-IR active band peaks used in this research.

3.6 Capacitance-Voltage (C-V) electrical measurement

Capacitance-voltage measurement is performed on Metal-Insulator-Semiconductor (MIS) structure using HP Agilent Model 4282. The capacitance measurement is performed on heavily doped Silicon (p-type) substrate and the capacitance values can be used to calculate the dielectric constant of material given as:

$$\varepsilon_{film} = \frac{C \times t}{\varepsilon_0 \times A} \quad \text{[Eqn. 3-38]}$$

Where C is the insulator capacitance value,

ε_0 is the permittivity of vacuum

t is the film thickness

A is the area of metal circle

Chapter 4

Experimental

4.1 Overview

The objective of this chapter is to present the fabrication of nanoporous organosilicates thin films via sacrificial porosity generators (porogens) approach or inorganic-organic nanohybrid technique. It also describes two sets of porous film with different morphology structure (i.e. open- and closed-pore films) used in this research. This chapter reviews the conventional thermal annealing process used to create porous film. In order to understand the concept of $SCCO_2$, the pressure-temperature phase diagram and properties in supercritical state is discussed. The schematic diagram of $SCCO_2$ system is shown. The experimental $SCCO_2$ parameters are described. This chapter also describes the reactions involves during silylation process by adding TMCS in supercritical and HMDS in vapor treatment.

4.1 Nanoporous organosilicates thin films

The generation of nanoporous thin films used in this research are based on the so-called sacrificial porogen (pore generator) approach by removing the organic macromolecular phase entrapped within crosslinked matrix selectively. This technique

has been developed by International Business Machines Corp. (IBM™) Almaden Research Center [48]. Figure 4-1 illustrates the basic schematic diagram of generating nanoporous thin film via sacrificial porogen approach. The process begins with a mixture of an appropriate amount of porogen and matrix (poly methyl sislsesquioxane – PMSSQ) solution that is spin coated homogenously on silicon wafer. The sample is cured at certain temperature and time duration to produce porogen phase-separated structure. At this stage, the cured sample is in its hybrid states such that the porogen is entrapped in the PMSSQ matrix. Next, entrapped porogen is removed via thermal annealing or supercritical, leaving behind nanoporous thin film.

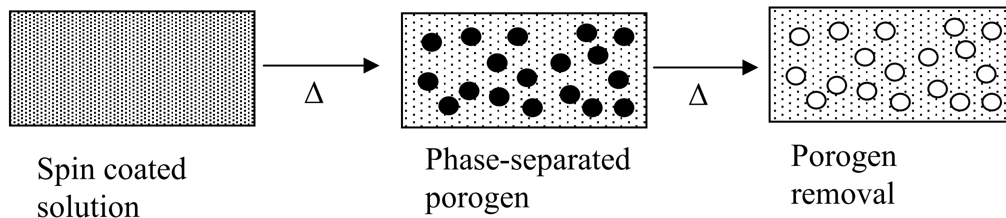

Figure 4-1. General procedure in preparing nanoporous film.

For nanoporous film, the pore volume fraction or percentage porosity of thin film describes its morphology structure which depends on the amount of porogen loading and matrix loading in the mixed solution. Larger amount of porogen loading leads to higher porosity. Likewise, less amount of porogen loading leads to lower porosity. There are two types of film morphology structures: 1. open-pore and 2. closed-pore structure. Higher porosity refers to interconnected pores within sample thickness. This is known as open-pore structure. Whereas, lower percentage porosity indicates that pores are separated

from each other and known as closed-pore structure. Figure 4-2 shows the difference between the open-pore and closed-pore morphology.

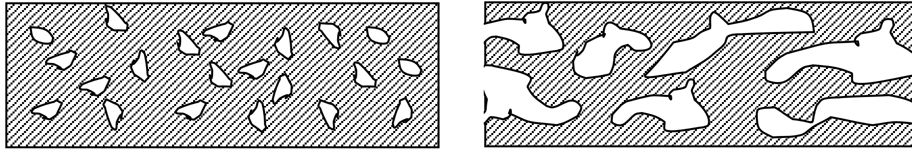

Figure 4-2. Nanoporous film with two different morphology structure (a) closed-pore and (b) open-pore.

4.1.1 Fabrication of sacrificial porogen approach

Figure 4-3 illustrates the procedure for preparing a nanoporous film. The sacrificial porogen used in this experiment is an organic polymer. The matrix, on the other hand, is an inorganic polymer – poly methylsilsesquixane (PMSSQ). Each of porogen and PMSSQ is first dissolved in solvent (propylene glycol methyl ether acetate - PGMEA) and sonicated for 10 minutes individually. Different morphology structure of the sample requires different amount of porogen loading. Depending on this desired structure, the dissolved porogen and PMSSQ is mixed at an appropriate amount and sonicated for 10 minutes to ensure it is homogeneously mixed. The mixed solution is then loaded into disposable syringe and filtered through 0.2 um polytetrafluoroethylene (PTFE) filter onto a clean silicon substrate.

Organic clean technique is used to clean the silicon substrate. The silicon substrate is soaked and sonicated in acetone for 5 minutes to remove organic contaminant and big particles on the sample surface. The sample is then rinsed with isopropanol and blew dry with compressed air. Once the silicon is cleaned, the silicon substrate is ready to

be used. The sample is spin coated at 3000 revolution per minute (rpm) for 30 seconds. After spin coating, the sample needs to be heated briefly on hot plate under Nitrogen (N_2) environment at 50°C to remove excess solvents. Next, the sample is cured for 2 hours at 200°C on a hot plate under N_2 environment to produce phase-separated structure of organic/inorganic hybrid. At this step, the porogen is phase-separated and entrapped within the crosslinked matrix. The reason to perform this process under inert N_2 environment is because porogen can decomposed at 150°C under ambient. If the porogen is decomposed prior to matrix crosslinking, there will be no phase-separated structure in the film, hence no porous film.

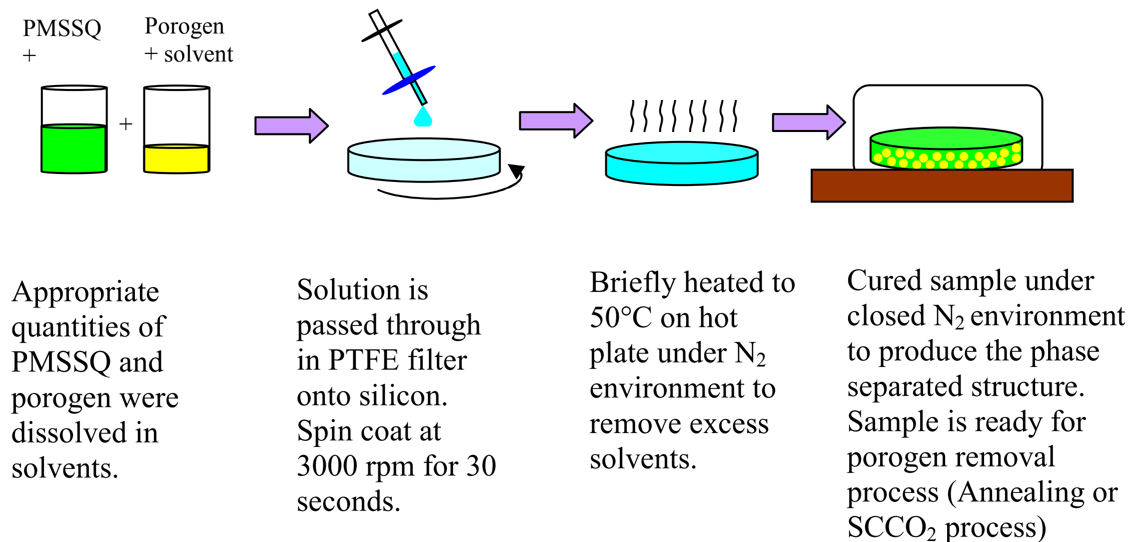

Figure 4-3. Procedures to prepare nanoporous film using sacrificial porogen approach.

4.1.2 Description of samples used in this research

In this research, two batches of samples that consist of both open- and closed-pores morphology structures are prepared. These films are fabricated by mixing

appropriate ratios of porogen and matrix precursor. Two types of porogen are used. The first batch is using poly propylene glycol (PPG) act as sacrificial porogen. Films with 25 wt% porogen loading gives closed-pore morphology structure (7525), whereas 55 wt% porogen loading gives open-pore morphology structure (4555).The second batch is using polypropylene oxide (PPO) act as porogen with 15 wt% (8515) and 45 wt% (5545) porogen loading for closed- and open-pore morphology, respectively. The molecular structure for PPG is $[–CH(CH_3)CH_2O-]_n$ with linear structure and molecular weight of 20, 000 g/mol. The matrix precursor for both batches is of poly(methyl silsesquioxane) (PMSSQ) with molecular structure of $[CH_3SiO_{3/2}]_n$. The solvent used for both PPG and PMSSQ solutions was propylene glycol methyl ether acetate (PGMEA). Table 4.1 shows the summaries of samples used in this study.

Samples	Morphology structure	Description
Batch #1. PPG/PMSSQ	Open, 4555	55 wt% porogen loading
	Closed, 7525	25 wt% porogen loading
Batch #2. PPO/PMSSQ	Open, 5545	55 wt% porogen loading
	Closed, 8515	15 wt% porogen loading

Table 4-1. Fabricated open- and closed-pore samples used in this study with either PPG or PPO as sacrificial porogen.

4.2 Thermal annealing process

A conventional thermal annealing process is used to vitrify entrapped porogen in matrix, hence creating nanoporous organosilicate thin film. Thermal annealing is a harsh process done at high temperature (430°C – 450°C) and longer time period (~5 hours). Typically the sample is put on hot plate and heat up from room temperature to ~450°C at

5°C/minute ramping under N_2 environment. Thermal annealing inherent several advantages. First, the PMSSQ matrix cannot withstand with high temperature, thus the pore may collapsed. Second, the processing temperature window can be narrow because the thermal decomposition of porogen must occur well below than the glass transition of matrix to avoid pore collapsed.

4.3 Supercritical CO_2 process

Supercritical CO_2 ($SCCO_2$) treatment is an excellent tool in generating nanoporous low-*k* thin film. At supercritical state, CO_2 possessed dual liquid-like solvating strength and gas-like diffusivity and viscosity at temperature above 31°C and pressure above 1050 psi. Moreover, supercritical fluid has a very low (~0) surface tension to allow penetration into nanoporous materials. $SCCO_2$ is an attractive process due to its low-cost process, non-toxic, does not support combustion and benign to environment. The addition of small amount of co-solvents or modifier can enhance the $SCCO_2$ solvating strength and extraction performance [49].

4.3.1 High Pressure $SCCO_2$ Experimental System

Figure 4-4 illustrats high-pressure system used in $SCCO_2$ research. This system is build with high pressure equipments type 316 stainless steel (i.e: tubing, pressure valve and connectors) rated to withstand pressure up to 20,000 psi under 200°C process. If the system temperature is above 200°C, the system capability is limited to 10,000 psi. Typically, the $SCCO_2$ process in this research is performed at temperature below 200°C

and pressure below 5000 psi. This system is equipped with high performance liquid chromatography (HPLC) pump that can handle pressure up to 7000 psi. The co-solvent is injected to the system by using HPLC pump at 1500 psi. High pressure vessel is placed in an oven and the tubing is wrapped with heating coil element to heat the system at certain temperature. Thermocouple is used to monitor the temperature. The dimensions of the stainless steel vessel are inner depth of 12.7cm, inner diameter of 2.5 cm and outer diameter of 6.3 cm. A sample holder with 12 pans slot is used to keep samples inside the vessel. This system is equipped with mechanical vacuum pump to exhaust out oxygen from the system prior to high pressure process. The $SCCO_2$ system is pressurized with CO_2 gas by air-driven gas booster pumps (Haskel, Burbank CA).

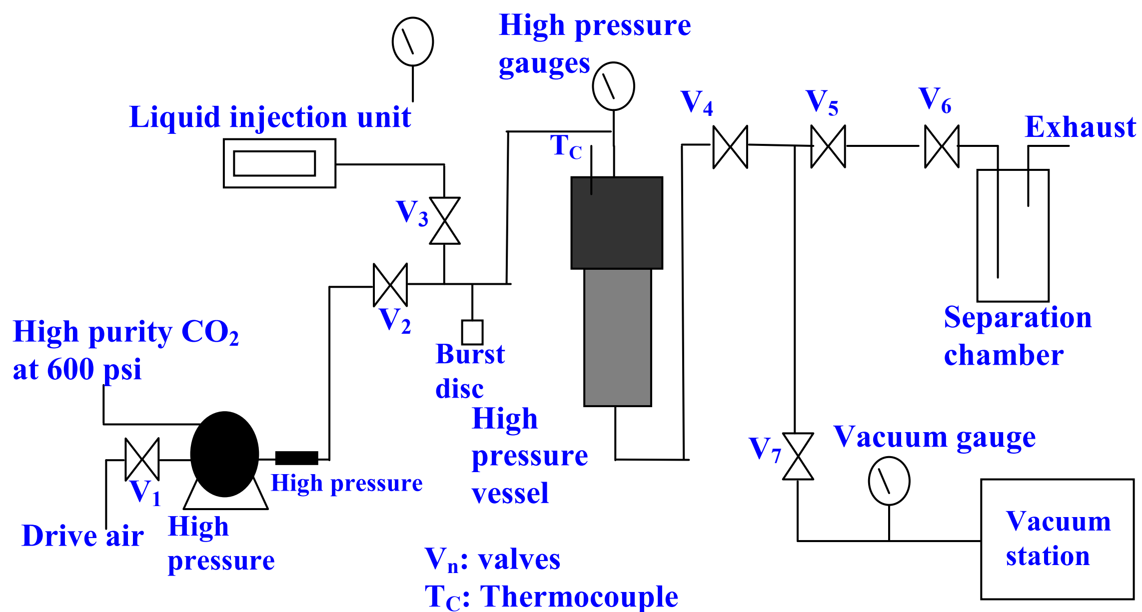

Figure 4-4. Schematic diagram of $SCCO_2$ system.

For safety purposed during performing high pressure experiment, the high pressure tubing is covered by ¼ inch thick polycarbonate (Lexan®) polymer which is a very durable material used as a bullet proof. Polycarbonate is a transparent and visible to light is often utilized as a protection in many places such as banks, warehouse, industries and also laboratories. A polycarbonate box enclosure with dimension of 42" x 35" x 64" is used to cover high pressure tubing. The mechanical vaccum pump is also covered by modified 3" thick of wooden cabinet. The wooden door is replaced by transparent polycarbonate to monitor the pressure sensor. The system is also installed with rupture disc for safety.

4.3.2 $SCCO_2$ treatment procedure

There are three modes of $SCCO_2$ process available such as static, dynamic and or combination of static/dynamic (pulse) mode. A static mode employs a supercritical system to hold at certain pressure and temperature for specified working time. In dynamic extraction mode, a fresh amount CO_2 at supercritical is continuously pass through the system. In static/dynamic or pulse mode, it requires an initial static period mode to inject co-solvent and followed by dynamic mode to flush out the contents of the system. Then, the fresh CO_2 and co-solvents is injected again into the system. This cycle is repeated based on the number of pulses needed [Martinez *at al*. 2003]. It is found that static/dynamic mode is favorable in a situation where co-solvents must diffuse into desired matrix to be extracted [50].In previous paper, $SCCO_2$ static mode is performed to remove porogen. However, this $SCCO_2$ static mode removal process took 14 hour [51].In this research, the static/dynamic mode $SCCO_2$ process is used. The pulsation

process requires pressurization and depressurization at every injection. The system is set at 1500 psi for solvent injections. Once injection is completed, the system is pressurized to 4500 psi. The system is then maintained at 4000 psi at a temperature of 165°C for a specified soaking time. The depressurization to 1500 psi is to ensure that the system is always at supercritical state. This cycle is continued until the third injection is completed. The system is pressurized and depressurized with fresh CO_2 to flush the excess solvent after each injection. Then, the system is prepared for another new injection. This cycle is repeated until all injections are completed. In final step, the $SCCO_2$ system is again flushed and then ramped down to 700 psi. The system has to cool down to room temperature (RT) at 700 psi prior collecting the samples for characterization.

The steps involved in the $SCCO_2$ extraction process is given as follows. First, the high pressure vessel and sample holder is cleaned with acetone and isopropanol. Samples are placed in the sample holder and keep inside the vessel. The system is vacuumed to minimize the oxygen contents inside the system. Then, the system is flushed with CO_2 at 550 psi twice repetitively. The system is then filled with CO_2 at 550 psi and the oven is ramped up to 165°C. Once the oven reached the temperature at 165°C, the heating element coil that is wrapped around the tubing will then be heated up to 90°C. The heating element coil took less time with approximately 5 minutes to heat up as compared to oven that needs around 40 minutes. The procedure of $SCCO_2$ static/dynamic mode used in this research follows the description mentioned above. Take note that solvent injection always occurred at supercritical state (i.e. CO_2 supercitical state is T_c = 31°C and P_c =1050 psi).

4.4 Experiment parameters

The $SCCO_2$ process is performed at temperature of 165°C and pressure of 3800-4000 psi. The vessel is heated in oven at 165°C. The high pressure tubing is wrapped with heating coil element and heated at temperature of 80°C to ensure that system is always in supercritical state. The solvent is injected at 1500 psi.

The vapor treatment is performed at 80°C for 30 mins under atmospheric pressure. The samples are placed in a leak-free chamber. The temperature is slowly raised from room temperature up to 80°C.

In the plasma treatment, samples are exposed to oxygen plasma with 20SCCM of CF_4 and 80SCCM of O_2 gas (SCCM denotes cubic centimeter per minute at STP) flows for 1 min at 200W plasma power and 600mTorr working pressure. The function of this plasma process is to simulate plasma damage in porous sample that occurs during next process integration (i.e: photoresist removal via plasma process).

Characterizations such as FT-IR spectroscopy and ellipsometery measurement are performed in ambient and room temperature.

Chapter 5

Preliminary Results and Discussion

5.1 Overview

This chapter overview preliminary result obtained from this research. Models used in spectroscopic ellipsometry analysis in characterizing porous thin film are presented. These models are designed to characterize several different types of porous film that would possibly being encountered throughout the research: single layer, bi-layer, graded single layer, graded bi-layer and film with surface roughness. The results are validated by other instruments such as Filmmetrics for thickness measurement and SAXS for pore volume fraction (percentage porosities). Scanning electron microscopy (SEM) imageries are also used to validate bi-layer ellipsometric model. Results of multiple co-solvents injections in $SCCO_2$ process are also included in this chapter. Preliminary results of $SCCO_2$ treatment for porogen and water removal are presented, along with the $SCCO_2$/TMCS treatment to remove the remaining of water in porous sample. Finally, this chapter presents the result of the HMDS vapor treatment to seal pores.

5.2 Implemented spectroscopic ellipsometry analytical method for characterizing porous thin film

The nonporous PMSSQ and SiO_2 were analyzed first as a reference for the porous films. The Cauchy model which worked well for transparent films was used for PMSSQ films. Since PMSSQ has a O-Si-O backbone based on its empirical formula of $[CH_3-SiO_{3/2}]_n$, the film may be transparent at the above wavelengths and Cauchy model may work. Figure 5-1(a) and Figure 5-1(b) show that the generated Ψ and Δ spectra for PMSSQ is nearly indistinguishable from the experimental data. Thus, the Cauchy model works well with PMSSQ films. Excellent agreement between the experimental and generated data (not shown here) for SiO_2 film were also found. The conversion of Cauchy to the graded Cauchy model did not change the Ψ and Δ fit spectra. This indicates that the nonporous PMSSQ and SiO_2 samples have the same refractive index across the film (i.e: non-graded) and thus, have uniform density.

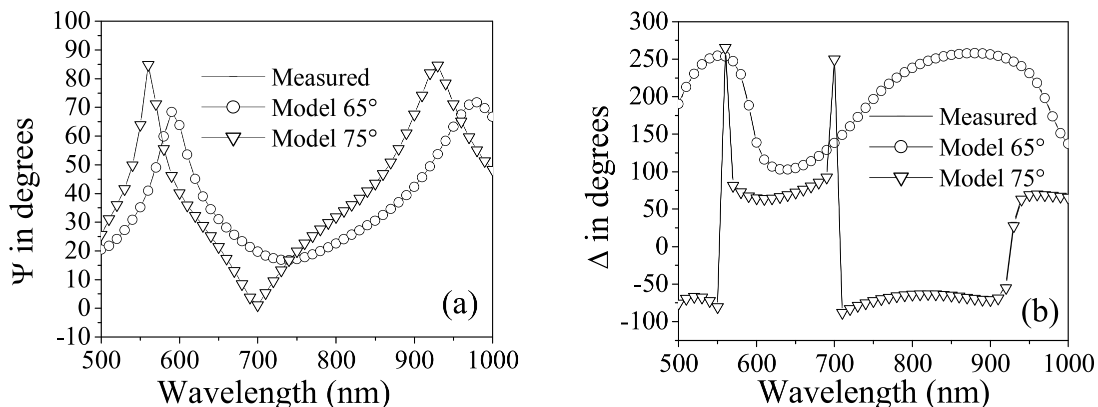

Figure 5-1. Nonporous PMSSQ (a) Ψ fit spectra (b) Δ fit spectra using Cauchy model. (MSE = 5.5).

Table 5-1 lists the thicknesses and optical constants for both PMSSQ and SiO_2 film obtained from Cauchy and graded Cauchy models. The value of the optical constants From Cauchy analysis, the PMSSQ has a thickness of 701 nm, refractive index of 1.38 and an MSE of 5.5. The conversion to a graded layer did not change the MSE significantly (4.9) resulting in similar thickness and refractive index. For SiO_2 film, modifying Cauchy to graded layer does not improve the MSE either. The thickness and refractive index for SiO_2 are 457 nm and 1.46, respectively.

Non-porous Sample	Model	Thickness (nm)	Refractive index (n)	MSE
PMSSQ	Cauchy	701.2	1.388	5.5
	Graded Cauchy	702.3	1.387	4.9
SiO_2	Cauchy	458.7	1.460	4.8
	Graded Cauchy	457.1	1.463	4.1

Table 5-1. List of optical constants and MSE for nonporous PMSSQ and SiO_2 film modeled as Cauchy and modified graded Cauchy layer.

Table 5-2 lists the thickness, refractive index, porosity and MSE values obtained by fitting the open- and closed-pore PMSSQ films using Cauchy, graded Cauchy and BEMA models. This summary of results will be referred throughout this section.

Sample	Model	Thickness (nm)	Refractive index (n)	Porosity (%)	MSE
Open-pore	Cauchy	637.1	1.137	–	3.1
	Graded Cauchy	638.6	1.137	–	1.5
	1 BEMA layer	637.1	1.137	63.3	3.0
	Graded 1 BEMA layer	638.7	1.137	63.5	1.6
	2 BEMA layers:				
	Top layer	595.5	1.137	63.5	1.5
	Bottom layer	43.2	1.125	66.5	
	Total thickness	638.7			
	Graded 2 BEMA layers:				
	Top layer	598.6	1.137	63.5	1.5
	Bottom layer	40.2	1.121	67.5	
	Total thickness	638.8			
Closed-pore	Cauchy	440.9	1.275	–	4.3
	Graded Cauchy	440.9	1.274	–	2.4
	1 BEMA layer	440.7	1.275	28.6	4.4
	Graded 1 BEMA layer	441.0	1.274	28.9	2.4
	2 BEMA layers:				
	Top layer	368.0	1.276	28.5	2.2
	Bottom layer	72.9	1.261	32.2	
	Total thickness	440.9			
	Graded 2 BEMA layers:				
	Top layer	370.3	1.276	28.4	2.2
	Bottom layer	70.4	1.259	32.7	
	Total thickness	440.7			

Table 5-2. List of thickness, optical constant, porosity and MSE for open- and closed-pore film using Cauchy and BEMA model with or without grading.

Figure 5-2(a) and Figure 5-2(b) show the measured and generated Ψ and Δ spectra for the porous PMSSQ film with open-pore structure. The Cauchy model also works well for the porous PMSSQ films. The spectra for closed-pore film were similar to open-pore film, hence, will not be shown. We obtained film thickness of 637 nm, refractive index of 1.13 and a relatively low MSE of 3.1.

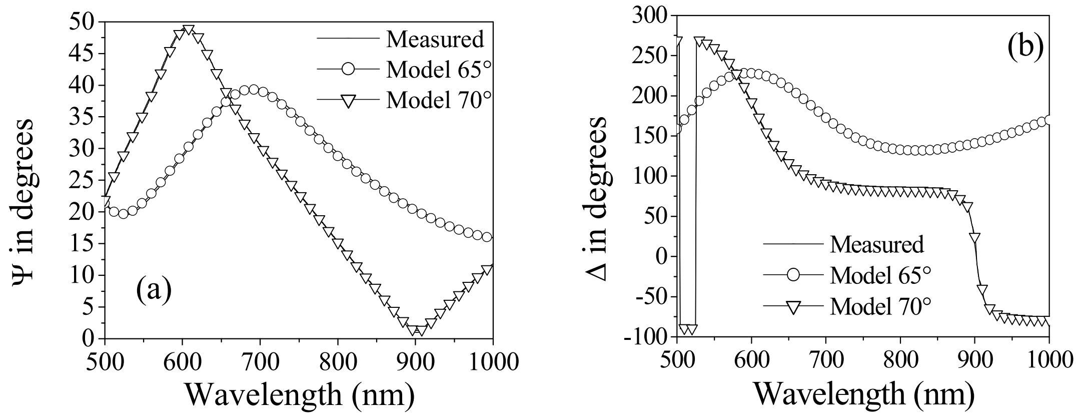

Figure 5-2. Generated and experimental (a) Ψ fit spectra and (b) Δ fit spectra using Cauchy model for open-pore sample with an MSE = 3.1.

For the supposedly open pore structure, the Cauchy model gives 637 nm with a low refractive index of 1.13 [Table 5-2], implying a lower density PMSSQ and confirming the porous nature of the film (nonporous PMSSQ has refractive index of 1.38). To calculate the porosity of the film, the BEMA model was used. Two sets of optical constants are used in BEMA calculation: (i) dense PMSSQ matrix and (ii) air. The BEMA model gave a similar Ψ and Δ behavior spectra with Cauchy model and is not shown here. This model gave 63.3% porosity with MSE value of 3.0 and thickness of 637 nm – values similar with the Cauchy model. This pore volume fraction obtained from ellipsometer analysis is lower by 3% than previously obtained. Surface roughness

simulation was added on the above models, but it did not improve the fit and MSE. This also mean that the porous film surface is relatively smooth (<1 nm roughness). The Cauchy and BEMA model is then modified to graded layers in order to study the behavior of porous sample. The graded layer model is created by subdividing 100 thin homogenous film layers. At each layer, the optical constant will slightly change. The depth profile is analyzed at 633 nm wavelength. Modifying both Cauchy and BEMA models to graded models has improved the fit by 50% (i.e. MSE decreased from 3.1 to 1.5).

Figure 5-3 shows the grading profile of the refractive index at 633 nm from single and double BEMA layers model for open-pore sample. For open-pore film fitted with single BEMA layer model, the depth profile shows an abrupt increase in refractive index at the silicon-film interface from 1.12 to 1.135. Then, the refractive index change very slowly towards the bulk of the film and became almost constant up to the surface (1.137). Thus, the bulk film may not have the same porosity compared with the thin interface layer based on figure 5.3.

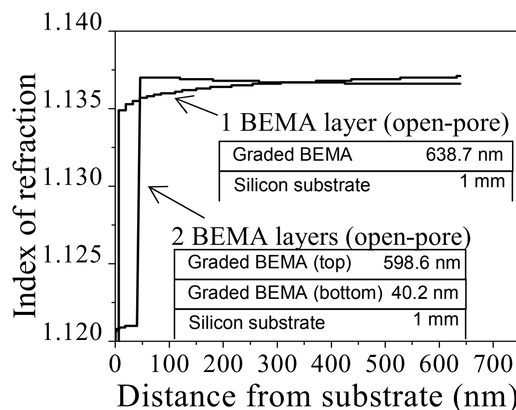

Figure 5-3. Depth profiles at 633 nm wavelength for open pore film using single BEMA with grading [MSE = 1.5] and two BEMA layers with grading [MSE = 1.5].

The material was then modeled as two BEMA layers to find the porosity and thickness values of the thin layer at the interface and bulk, respectively. During the fitting process, the percent porosity and the thickness of the two BEMA layers are left to vary or float. The result from Table 5-2 shows that the interface layer is 43 nm with a porosity of 66.5% whereas the bulk has 3% less porosity (63.5%). The MSE value for this modeling is 1.5, which, is equivalent with graded BEMA (1.5). We have also graded the two BEMA layers with the goal of lowering the MSE and have a more specific description of the film. Figure 5-3 shows depth profile for open pore structures film using two independent graded BEMA layers. The porosity at the silicon-film interface is 67.5% and 63.5% porosity at the bulk – a difference of 4%. The interface layer thickness was 40.2 nm while the bulk was 598 nm. The MSE for this modeling (1.5) is the same with the graded BEMA and two BEMA layers models. Since all three models gave the same MSE, either one can be used to physically describe the film. One common conclusion that can be derived in all three models is that the interface is 3 – 4% more porous than the bulk. The maximum thickness of this interface layer is 43 nm.

For the closed-pore film, similar analysis was performed as the open-pore film. The thickness of the film was 440 nm with a refractive index of 1.275 and MSE of 4.3 [Table 5-2]. The BEMA layer gives a porosity of 28.6% and similar thickness, refractive index and MSE. This pore volume fraction obtained is higher by 2% from previous measurements. The generated and experimental Ψ and Δ fit spectra show a similar characteristics with the open pore films. We then converted the models into graded layers. Figure 5-4 shows the grading profile for closed-pore sample and show the same behavior as the open-pore film. The interface has a lower refractive index and it gradually

increases towards the surface of the films. The resulting MSE of the graded layers were 2.4, a 50% improvement of the fits. The film was also modeled as two BEMA layers, but the MSE fit improvement is similar with graded model (2.2). The bottom layer (72.9 nm) show a porosity of 32.2% and the bulk is 28.5%. Both BEMA layers were also graded but the MSE fit remained unchanged. Figure 5-4 also shows depth profile for closed pore structure using both graded BEMA layers. The bottom layer shows a thickness of 70.4 nm and a porosity of 32.7% while the bulk has a porosity of 28.4%. Following the same arguments as the open-pore films, either the graded BEMA or Cauchy, two BEMA, and two graded BEMA models could be used to describe the closed-pore films because of similarity of MSE. However, it is clear that the substrate-film interface of the porous samples is 4% more porous than the bulk with a maximum thickness of 73 nm. Spectroscopic ellipsometry could not distinguish between open or closed- pore samples. The wavelength of the incident light (197 ~ 2000 nm) is far too broad to be affected with the pore sizes of the samples (2~8 Å)[22]. All of the models used have given almost the same total thickness.

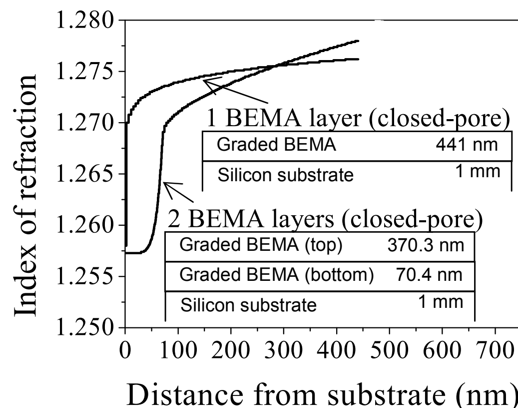

Figure 5-4 Depth profiles at 633 nm wavelength for (1) closed pore films using single BEMA with grading [MSE = 2.2], two BEMA layers with grading [MSE = 2.2] and (2) single porous film using single BEMA grading [MSE = 1.0]

Not all porous films are graded as we will be shown next. For directly baked porous sample (PPG MW=600 g/mol), we obtained an excellent agreement between generated and experimental data by using Cauchy and BEMA model (MSE=1). We then converted Cauchy and BEMA models to graded layers giving the same fit as non-graded fits (MSE =1). This suggested that the directly baked porous sample has a uniform refractive index throughout the sample and not graded.

For the bi-layer porous samples, similar technique is performed in the analysis. The bi-layer sample is first modeled as a single Cauchy layer and BEMA layer. As expected, the experimental and generated data does not fit very well given an MSE of 77 (see Figure 5-5(a) and Figure 5-5(b)). The single layer model modified to graded model does not improved the fit very well (MSE = 29). The model is then modified to two independent Cauchy layers and BEMA layers improving the experimental and generated spectra significantly reducing the MSE fit to 3.5 (see Figure 5-5(c) and Figure 5-5(d)). The ellipsometer results for bi-layer sample are compared with Filmetric-F20 thin film measurement system. This technique is based on light reflectance. For the top film, our measurements show 199 nm thickness with a 1.197 refractive index and for bottom film, 884.7 nm with 1.263 refractive index. This results agree with Filmetric measurement (top film: thickness = 228 nm, n = 1.21, bottom film: thickness = 948 nm, n = 1.27). The porosity of the bi-layer film obtained from two BEMA models (MSE = 3.5) were 48.1% for the top film and 31.8 % for the bottom film.

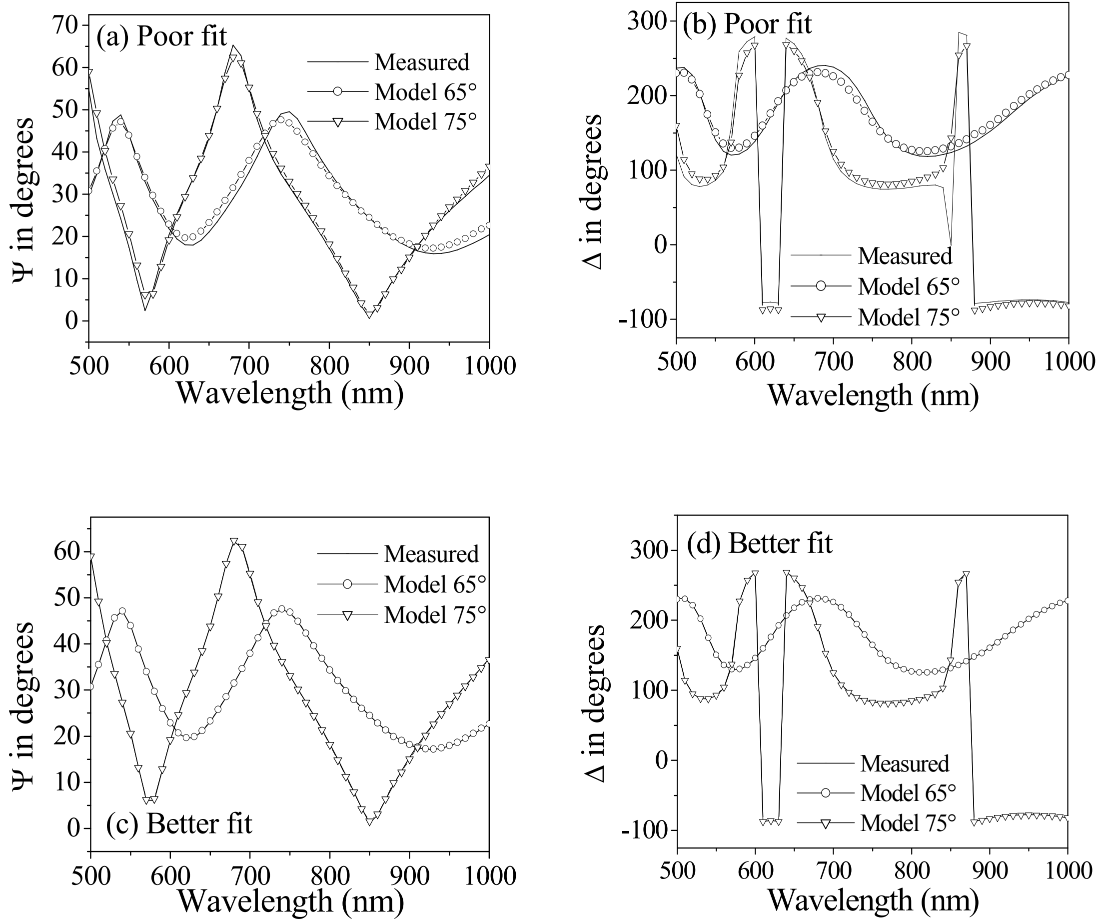

Figure 5-5. Generated and experimental (a) and (b) using single BEMA model (MSE=77) and (c) and (d) using double BEMA model (MSE=3.5).

Figure 5-6 shows the depth profile of the graded bi-layer films at 633 nm wavelength using two BEMA layers. The bi-layer model is also modified to graded layer giving MSE of 3.1 (top film: thickness = 197.4 nm, n = 1.195, percent porosity = 48.6%, bottom film: thickness = 886.2 nm, n = 1.262, percent porosity = 31.8%). The profile show two distinct thicknesses and refractive index.

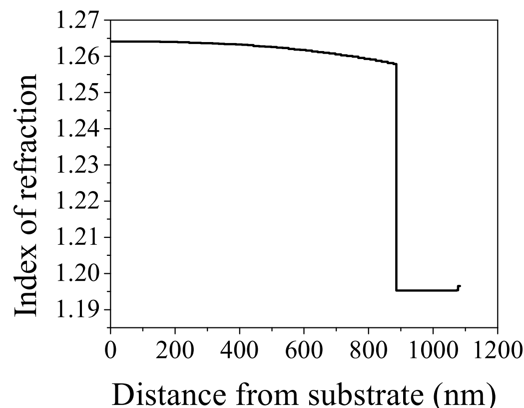

Figure 5-6. Depth profile at 633 nm wavelength for bi-layer porous film with different porogen loading.

In the following discussion, we will show that a porous film can eventually be graded depending on different treatments the film undergoes. The closed-pore (OS7525) sample underwent Supercritical CO_2 ($SCCO_2$)/co-solvent process to remove the porogen, thus, making the film porous. The details of $SCCO_2$ treatment are in reference 22. This processed film was then O_2 plasma-ashed [CF_4/O_2 (20sccm/80sccm) for 1 min at 200W plasma power)]. It is suggested that O_2 plasma ashing replaces -CH groups from the pore surface by substitution reaction causing the formation of polar Si-OH in the following mechanism,

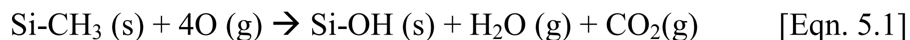

$$\text{Si-CH}_3\text{ (s)} + 4\text{O (g)} \rightarrow \text{Si-OH (s)} + \text{H}_2\text{O (g)} + \text{CO}_2\text{(g)} \qquad \text{[Eqn. 5.1]}$$

The OH-substituted endgroup is very favorable to attract moisture which in effect would increase the refractive index in time [Liu *et al*. (2002), Xie *et al*. (2004)]. Since treatment is at the surface of the film, CH groups would be reacted more at the topmost and closer regions where O diffusion accessibility is high. Consequently, O_2 plasma damage (by OH substitution) is expected to be higher at the topmost layer of the film and decreases with respect to film depth, thus, a graded film is created.

For O_2 plasma-ashed sample, we found that modeling it as a single layer gave a poor fit with MSE of 25. The model is then modified to graded layer which improved the fit significantly with MSE of 4. We have also tried modeling the sample as bi-layer and graded bi-layer, but it gave a poor fit with MSE of 30 and 20, respectively.

Figure 5-7 shows depth profile for O_2 plasma-ashed film. We observed that this sample was indeed graded with a large variation in refractive index. We found that plasma damage occurs not only at the surface but into 3/4 of the film thickness. The top surface of the ashed sample has higher refractive index; indicating the presence of Si-OH bands. The above discussion shows the versatility of spectroscopic ellipsometry. Since the interlayer dielectric (ILD) films are exposed to O_2 plasma and solvent cleaning to remove organic residual photoresist, it is important to understand the behavior of porous sample after the treatment. This ellipsometric analysis is crucial because it shows that oxygen plasma destroyed the film which may create a reliability problem.

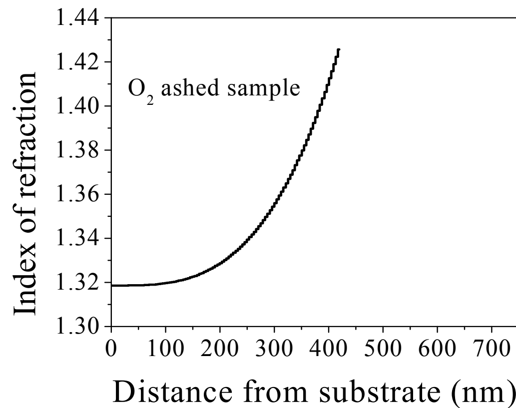

Figure 5-7. Depth profile at 633 nm wavelength for O_2 ashed.

In next section, the preliminary results of $SCCO_2$ treatment for porogen and water removal in inorganic-organic hybrid porous film is presented.

5.3 $SCCO_2$ with Pulsing Mode to Remove Porogen Effectively

5.3.1 Overview

As mentioned in chapter 4, there are three modes of $SCCO_2$ process available such as static, dynamic and or combination of static/dynamic (pulse) mode. Previously, Rajagopalan *et al*. (2003) have successfully removed porogen from inorganic/organic hybrid film via $SCCO_2$ static mode. However, the $SCCO_2$ static mode process was operated at longer time duration (14 hour) and at higher working pressure (7000 psi) to remove porogen. The $SCCO_2$ static mode is not efficient. The combination of static/dynamic mode has been performed widely for $SCCO_2$ extraction strategy with a better performance as compared to single static or single dynamic mode [52]. It is believed that $SCCO_2$ with pulsing mode could extract porogen and water efficiently. In this research, the performance of $SCCO_2$ static/dynamic (pulse) mode for porogen removal is evaluated.

5.3.2 Experimental Procedure

In this study, the performance of $SCCO_2$ process with multiple injections is evaluated. Porous sample of PPO/PMSSQ of open-pore structure is used. The sample is subjected to $SCCO_2$ process at four sets of pulses: 1 pulse, 4 pulses, 6 pulses and 10 pulses. The processing $SCCO_2$ parameters are at temperature of 165°C and working pressure of 3800 – 4000 psi. The solvent must be injected at supercritical state, thus the injection only occurs at pressure of 1500 psi. After each injection, the system is hold at

desired working pressure and soaking time. Then, the system is flushed with CO_2 by raising the pressure to 3000 psi and depressurize down to 1500 psi. This process is repeated twice. Then the system is ready for another injection. The objective of flushes is to ensure that the system is clean from excess solvent prior to a new set of solvent injection. MEK is used as a co-solvent for this process. 2 ml of MEK per pulse is injected into the system. The total time for each of this $SCCO_2$ process is 1 hour. These results are then compared to before extraction and annealed sample.

5.3.3 Results and Discussions

Figure 5-8 shows the changes of refractive index values after multiple co-solvents injections into the $SCCO_2$ system for porogen removal in comparison with annealed sample. For before extraction (as-cured) sample, the refractive index and thickness value is 1.44 and 846 nm, respectively. The lower n value indicates that more porogen has been removed creating porous structure. From the graph, we can see a trend such that as number of pulses increases, the refractive index value decreases. The $SCCO_2$ process with 6 pulses technique produced the lowest n value of 1.19 which is comparable with the annealed sample (n = 1.18). Notice that the refractive index for 10 pulses process is high. This may be due to the excessive solvent injected into the system which leads to less efficient extraction process. This information is validated by $-CH_n$ absorption band from FTIR spectra.

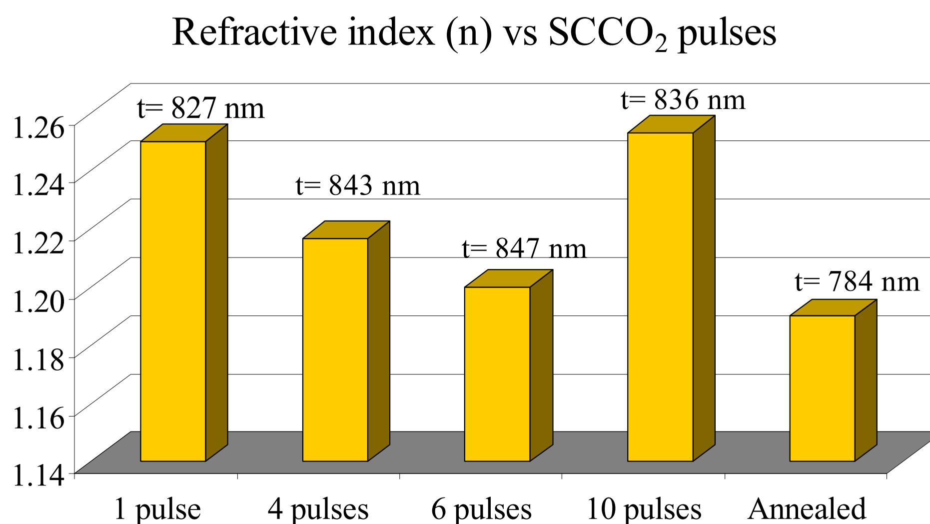

Figure 5-8. Multiple co-solvents injections $SCCO_2$ process in comparison with annealed sample.

Figure 5-9 shows the FTIR –CH absorption band spectra of multiple injections applied during the $SCCO_2$ treatment as compared to before extraction and thermal annealing process. Upon thermal annealing process, the entrapped porogen and water is completely removed. The annealed spectrum is then used as a reference to the $SCCO_2$ processed in order to evaluate how much porogen/water has been removed from sample. From Figure 5-9, it can be seen that as number of co-solvents injections increases the –CH_n peak decreases. This indicates that more pulses yields to a better extraction process. We conclude that multiple injections in the $SCCO_2$ process is more efficient in extracting porogen as compared to static mode. Hence, $SCCO_2$ static/dynamic (multiple co-solvents injections) technique is used through in this research.

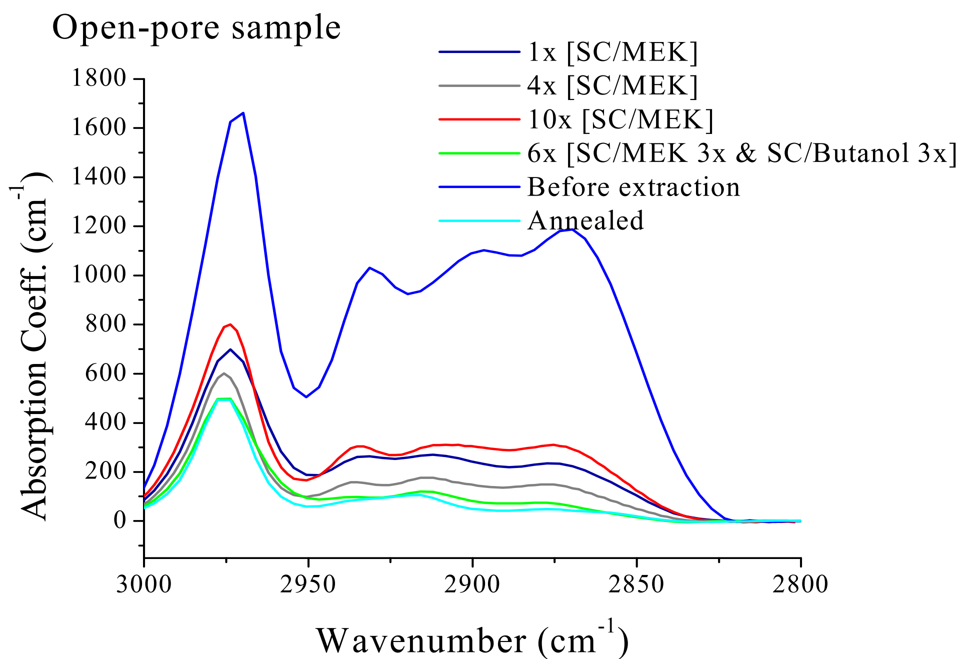

Figure 5-9. FTIR –CH absorption spectra for multiple injections in $SCCO_2$ process

5.4 Porogen and Water Removal via $SCCO_2$

5.4.1 Overview

This section presents a two step $SCCO_2$ process to remove porogen and water effectively from nanohybrid thin film at lower temperature and shorter time period. The first step is a $SCCO_2$ process with the addition of co-solvents to remove porogen. After $SCCO_2$/co-solvents process, the refractive index is still high due to –OH bonded in porous sample which can be later verified via FTIR analysis. Previous studies have shown the $SCCO_2$ treatment with addition of alcohol increases the water solubility which

enhances the water extraction from porous sample [53]. Therefore, the second step is a $SCCO_2$ process with the addition of methanol or butanol to remove water.

5.4.2 Experimental Procedure

In this section, $SCCO_2$/co-solvents followed by $SCCO_2$/methanol is used to remove porogen and water. Two separate experiments are performed. First, we evaluate the performance after the individual $SCCO_2$ process. Second, we evaluate the performance of the two $SCCO_2$ process in sequence. For the individual $SCCO_2$ process, both closed- and open- pore morphology with 25 wt% and 55 wt% porogen loading is used. The MSSQ is used as a matrix, whereas PPG is used as sacrificial porogen. Here, we performed three injections and 3 ml of solvents per injection. The soaked time for the three injections were 15 min, 15 min and 30 min for a total time of 1 hour. For the two $SCCO_2$ process in sequence, both closed- and open- pore morphology with 15 wt% and 45 wt% porogen loading is used. The MSSQ is still used as a matrix, however PPO is used as sacrificial porogen. The processing parameters are still the same as above [3 ml, 3 injections, 1 hour process].

5.4.3 Results and Discussions

5.4.3.1 Part A: Depth profile analysis of porous sample individual $SCCO_2$ process.

This section shows ellipsometric analysis to obtain percentage porosities and the refractive index depth profile of nanoporous samples. Figure 5-10 shows the refractive

index depth profile at 633 nm wavelength for closed-pore samples after several treatments: before extraction of porogens (as-cured), directly annealed, $SCCO_2$/co-solvents and $SCCO_2$/methanol treatments. The as-cured and annealed samples are used as the reference points to evaluate the performance of $SCCO_2$ process in creating nanoporous film. The refractive index depth profile shows that as-cured sample have a homogenously refractive index (n=1.44) distributed throughout the sample thickness (t=580nm). This indicates that the as-cured sample is a dense material. Previous study has shown the dense as-cured sample is consisted of phase-separated porogen entrapped in the PMSSQ matrix within film thickness via FTIR analysis [21]. The depth profile of ellipsometric analysis in Figure 5-10 shows that the refractive index of the processed samples increases abruptly from the silicon-film interface to bulk film, and becomes stable at the bulk to film-air interface. This indicates that the nanoporous PMSSQ film does not have the same porosity at both the silicon-film interface and bulk layer. A rigorous ellipsometric analysis in modeling the nanoporous PMSSQ sample as two layers has been presented recently [54]. The two layer model provides the percentage porosities of the silicon-film interface and bulk film. From our previous analysis, we found that the annealed closed-pore sample has 4% more porous at the silicon-film interface as compared to bulk film. In a separate study, the neutron reflectivity (NR) analysis on nanoporous PMSSQ film was discovered to have higher porosity at the interface between porous film and silicon substrate [55]. For this NR method, the porous sample is exposed to toluene (vapor or liquid) and then reflected incident beam through silicon substrate. The NR analysis include the reflectivity data measurement as a function of scattering vector, which presents the information on the depth profile of pore distribution in

nanoporous PMSSQ. It is believed that higher porosity at the silicon-interface is due to the interaction between the organic polymer and the substrate.

The conventional thermal annealing at high temperature (450°C) indeed removed all entrapped porogen as shown in Figure 5-10 by the decrease in refractive index of 1.27 from 1.44 and by the film porosity of 29.8%. Direct thermal annealing, water was also removed. However, this process leads to significant thickness shrinkage up to 23% as verified by SE. This is an indication of pore collapse (i.e: before and after annealing is 580 nm and 444 nm, respectively). For the same film treated with $SCCO_2$/MEK-THF co-solvents, *n* is reduced to 1.291 with 25.7% porosities. We suspect that the incomplete water removal causes high refractive index as compared to the annealed sample. This assumption is later verified by FTIR spectra.

$SCCO_2$ process with addition of Methanol has further reduced refractive index as compared to $SCCO_2$/MEK-THF process. However, the refractive index of the process with Methanol treatment is slightly higher than annealed sample. The nature of the closed-pore film structure with separated pores may results in incomplete porogen and/or water removal. Similar as $SCCO_2$/co-solvent process, the film thickness after $SCCO_2$/methanol does not change as compared to before extraction (t=~570 nm). This result is good because thickness shrinkage and pore collapse creates stress and delamination in the device creating reliability problems.

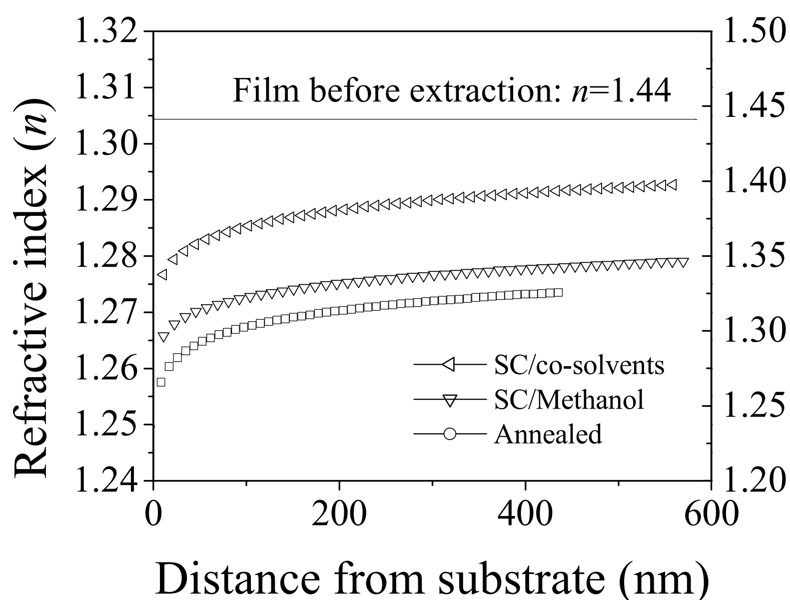

Figure 5-10. Refractive index depth profile at 633 nm wavelength for closed-pore film after several treatments: before extraction, $SCCO_2$/co-solvents and $SCCO_2$/Methanol process.

Figure 5-11 shows the baseline corrected FTIR –OH absorption spectra of the closed-pore film before extraction, $SCCO_2$/co-solvents and $SCCO_2$/Methanol treated. For the quantitative FTIR spectra analysis, multiple Gaussian curve fittings are utilized to calculate the percentage of water removal after each treatment. It is found that only 34% water has been removed after $SCCO_2$/co-solvent treatment. However, it is necessary to remove silanol (–OH) group completely because it destroys porous sample properties by raising the refractive index and *k*-values. Previous experiments have found that adding alcohol has increase water solubility, and thus enhancing water extraction [53]. In this paper, we injected methanol in $SCCO_2$ to remove silanol group. After $SCCO_2$/methanol treatment, the –OH group has indeed reduced significantly with 98% water removal. The

performance of $SCCO_2$/methanol is comparable with annealed process such that both samples have negligible zero amount of –OH absorption.

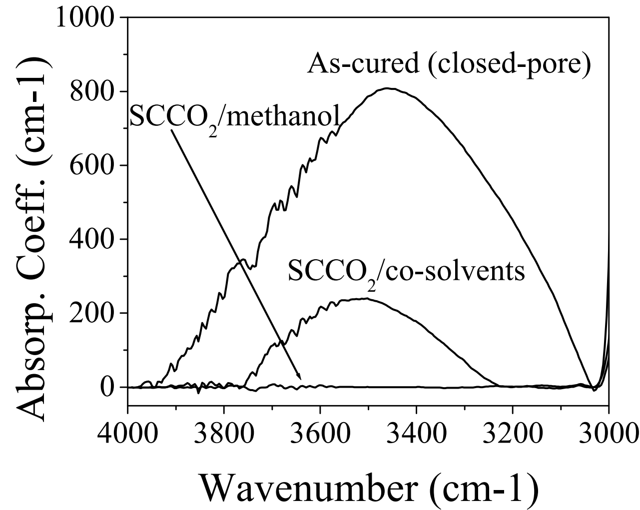

Figure 5-11 FTIR spectra of –OH absorption band after several treatments: as-cured, $SCCO_2$/co-solvents and $SCCO_2$/Methanol process.

We also performed the same process and analysis on an open-pore porous sample. Figure 5-12 shows the refractive index depth profile at a wavelength of 633 nm for the open-pore sample under several treatment conditions: before extraction, after $SCCO_2$/co-solvents and $SCCO_2$/Methanol. Similar to closed-pore sample, the film thickness after each $SCCO_2$ process remain the same as before (i.e. as-cured sample, t = 940 nm). The $SCCO_2$/co-solvents process removed porogen, and hence reducing *n* value from 1.44 to 1.145 with 63.6% porosities. The *n* value for the open-pore sample is still slightly higher than annealed sample, which is similar to the closed-pore sample. Based on the multiple Gaussian curves fitting, 90% of –OH are found remaining in the sample (FTIR for open pore is not shown here). This scenario leads to a higher refractive index value. The same

samples underwent $SCCO_2$/methanol process to remove –OH group, we found that 100% of –OH has been successfully removed. Referring to Figure 5-12, it is found that the *n* value has reduced to 1.137 which is similar as annealed sample (n=1.137) with equivalent percentage porosities (63.6%). This $SCCO_2$ processed sample possessed the same properties as annealed sample such that –OH is completely removed with low refractive index value. This may be due to the open-pore morphology, such that co-solvents and methanol can diffuse easily and react into the pore so as to remove porogen and water. Moreover, $SCCO_2$ process has no reduction of film thickness as compared to the annealed sample. The annealed sample has a reduction of film thickness by 32% (i.e. ascured, t = 940 nm, and annealed, t=640nm).

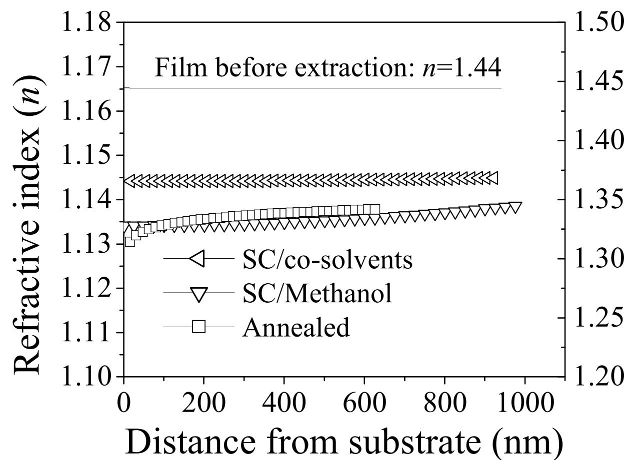

Figure 5-12. Refractive index depth profile at 633 nm wavelength for open-pore film after several treatments: before extraction, $SCCO_2$/co-solvents and $SCCO_2$/Methanol process.

5.4.3.2 Part B: Two Steps of $SCCO_2$ Process in Sequence

As discussed in Part A, $SCCO_2$ with addition of co-solvents helped in removing porogen, whereas $SCCO_2$ with addition of methanol assisted in extracting –OH bond from porous sample. In this section, we combine the two chemicals in sequence without removing the sample from $SCCO_2$ chamber after each treatment. Two types of alcohol, butanol ($C_4H_{10}O$) and methanol (CH_3OH), are used in the water removal process. Figure 5-13 shows the FT-IR absorption spectra of –OH and –CH region after each process. For simplification, Butanol* refers to $SCCO_2$/MEK followed by $SCCO_2$/Butanol, whereas Methanol* refers to $SCCO_2$/MEK followed by $SCCO_2$/Methanol. It is shown that Methanol indeed lowering the amount of -OH significantly. The addition of alcohol increases the polarity of the supercritical fluid and increases the solubility of water. Hence, $SCCO_2$ with addition of alcohol can diffuse and extract the silanol group out of the porous sample easily which leads to reduction of –OH absorption. Methanol treatment does not helped in removing porogen due to the existed high absorption of –CH band after the treatment. Butanol, on the other hand, removed a significant amount of –CH but not –OH band. This shows that Butanol indeed contributes in porogen removal process. Based on these results, the next experiment will be a sequence of MEK, followed by Butanol and Methanol.

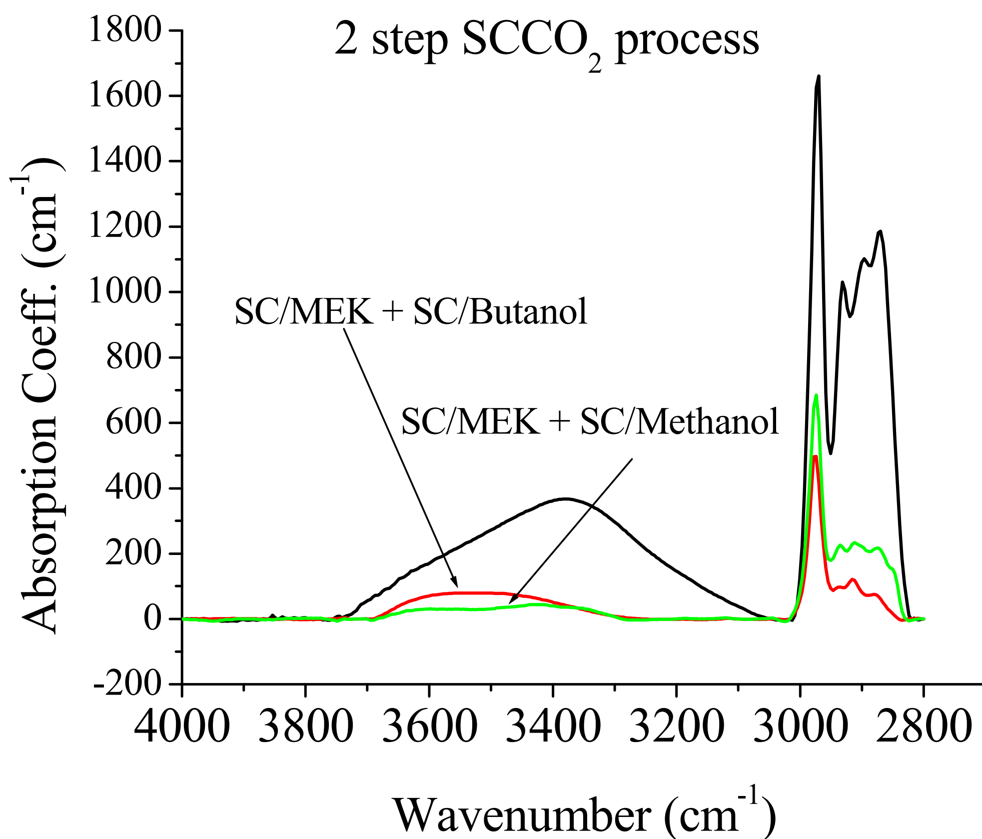

Figure 5-13. FTIR absorption spectra of -OH and -CH band after Butanol* and Methanol* $SCCO_2$ treatment.

5.5 Silylation (TMCS) to Restore Hydrophobicity in Porous Film via $SCCO_2$

5.5.1 Overview

$SCCO_2$ process with addition of co-solvents and alcohol is found to remove water and porogen efficiently. Although a complete water removal is achieved, high porosity film, by nature, possesses a large surface area making it vulnerable towards moisture

uptake. It will adsorb moisture easily from the environment over time that results in increased the –OH bond back. Water in the form of –OH (silanol) group is responsible in increasing refractive index and dielectric constant of material, hence it will eventually deteriorating the properties of porous thin film.

In the next process, the performance of silylation process using TMCS to terminate porous film with methyl group is investigated. The termination of the sample surface involves in changing the remaining polar –OH in sample to nonpolar $–CH_3$ group. The TMCS treatment helps in converting the sample properties to hydrophobic hence blocking water adsorption.

5.5.2 Experimental Procedure

A set of PPO/PMSSQ for both open and closed-pore sample is used in this work. The TMCS treatment was done as follows: $SCCO_2$/MEK, $SCCO_2$/Butanol, $SCCO_2$/Methanol and followed by $SCCO_2$/TMCS. For simplification, the term TMCS* treatment refers to the described $SCCO_2$ process in sequence is used throughout the text. Each of these individual $SCCO_2$ process was done with the same procedure [2ml/injections, 5min/pulse, 3-4 flushes in between injections].

5.5.3 Results and Discussions

Figure 5-14 shows –OH spectra of (a) open-pore and (b) closed-pore sample after Butanol*, Methanol* and TMCS* treatment as compared to before extraction (as-cured).

In general, both open-pore and closed-pore sample has encounters reduction of water peak after treated with $SCCO_2$ treatment. Figure 5-15 shows the percentage water remained in the sample after the treatments. There are huge reduction in –OH spectra for both open-and closed pore structure. There is a small amount of silanol absorption for closed-pore structure. However, this may due to the closed-pore structure (15 wt% porogen loading) blocking TMCS molecules to react with silanol group in the sample. Figure shows the percentage water remaining the sampler after SCCO2 treatment. The calculated values are obtained from multiple Gaussian curve fitting analysis.

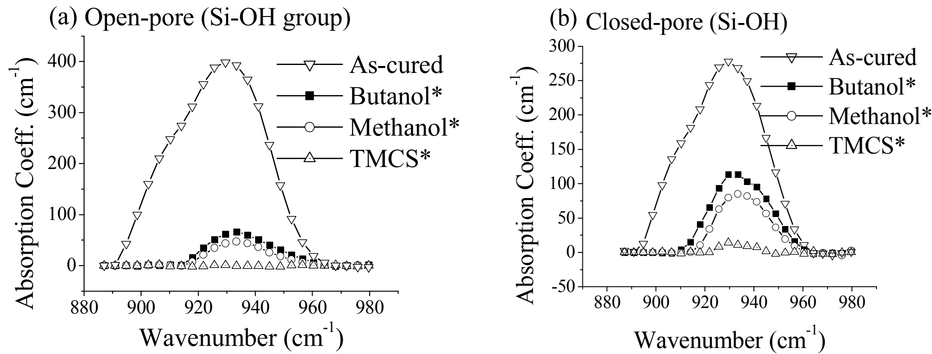

Figure 5-14. Absorption spectra of -OH region after several treatments including TMCS treatment for (a) open-pore and (b) closed-pore sample.

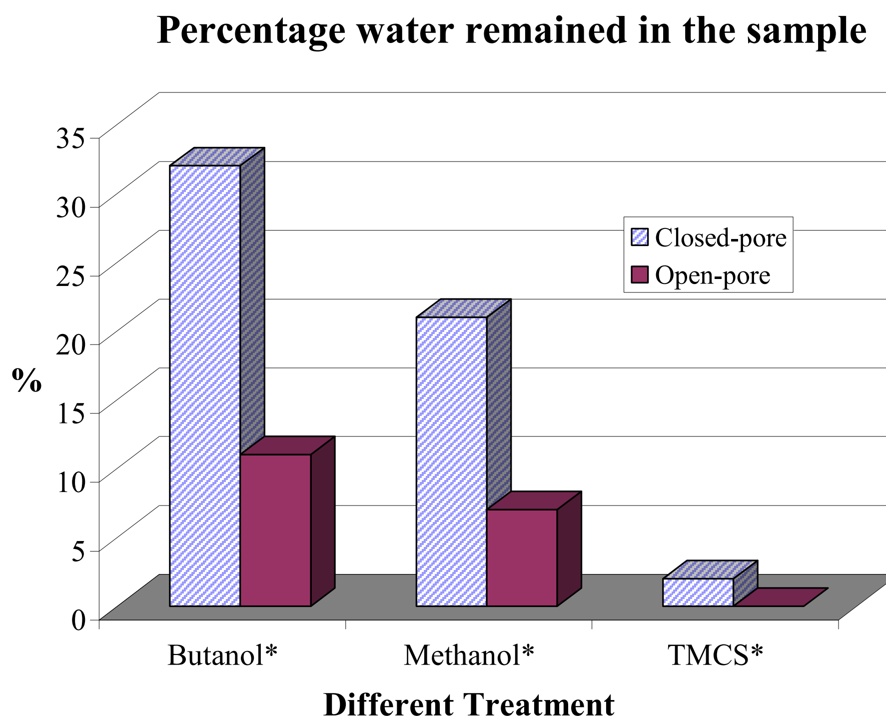

Figure 5-15 Percentage water remained in the sample after different treatments.

Figure 5-16 illustrates the FTIR methyl group absorption spectra within 3100 cm^{-1} to 2800 cm^{-1} spectra after methanol* treatment, Butanol* and TMCS* treatment for open-pore film. It shows there is an increased CH_3 absorption peak of after TMCS treatment. $SCCO_2$ is used to deliver trymethylcholorilane (TMCS) into the sample and removed –OH bond. After TMCS silylation in $SCCO_2$, silanol (Si-OH) group is removed and converted to methyl group (Si-O-Si(CH_3). It is suggested that the mechanism of TMCS silylation on porous sample follows the following reactions:

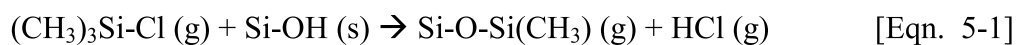

$$(CH_3)_3\text{Si-Cl (g)} + \text{Si-OH (s)} \rightarrow \text{Si-O-Si}(CH_3)\text{ (g)} + \text{HCl (g)} \qquad \text{[Eqn. 5-1]}$$

It is anticipated that after TMCS silylation process the sample surface will become hydrophobic due to the change in termination surface from polar –OH to nonpolar methyl group (–CH_3). This anticipation can be verified via FT-IR spectra. It can be seen that the silanol group (see Figure 5-14) is reduced due to the replacement of $Si(CH_3)$ (see Figure 5-16). Figure 5-17 illustrates the FT-IR methyl group absorption spectra within 3100 cm^{-1} to 2800 cm^{-1} spectra after the methanol* treatment, Butanol* and TMCS* treatment for closed-pore film. Similar absorption is found with an increased of CH_3 absorption spectra after the TMCS* treatment. Further details of chemical reaction and FTIR spectra analysis will be discussed in the final dissertation.

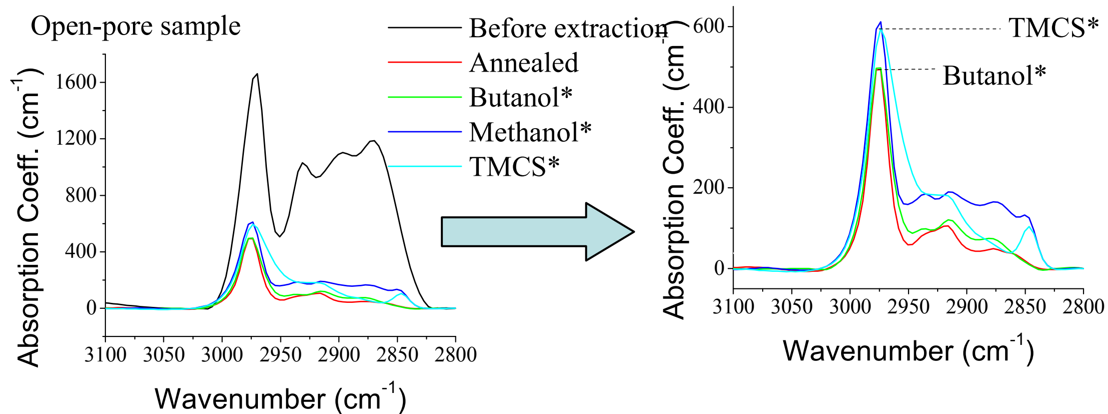

Figure 5-16. Absorption spectra of CH region after several treatments including TMCS treatment for open-pore sample.

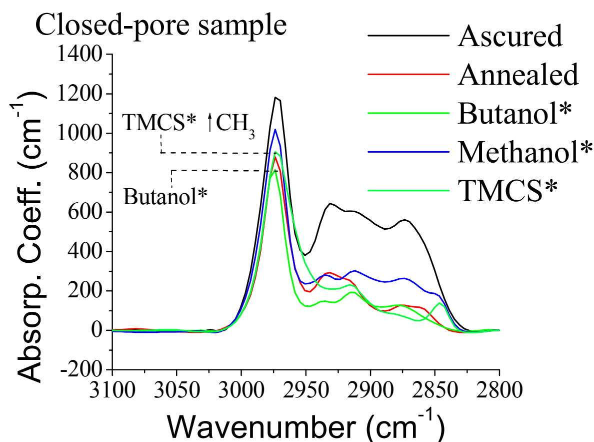

Figure 5-17. Absorption spectra of CH region after several treatments including TMCS treatment for closed-pore.

5.6 Spectroscopic ellipsometry study of the reduction in porosity of open-pore organosilicate films after hexamethyldisilazane treatment

5.6.1 Overview

Plasma processing plays an important role in pattern transfer during circuit integration process. CF_4/O_2 and O_2 plasma processing have been commonly used for photoresist and ash residue removal. However, oxygen-based plasma induces damage to hybrid orgranic porous film by changing the sample properties from hydrophobic to hydrophilic. The oxygen molecules diffuse into dielectric layer and reacts with $-CH_3$ by converting it to –OH. This phenomenon increases the damaged sample sensitivity towards moisture; hence increase the *k*-value. Several researches have reported repairing moisture uptake of plasma damaged porous films using silylating agents. In this research,

we investigated the effects of HMDS treatment at the surface and the bulk of the plasma damaged porous films by using VASE.

5.6.2 Experimental Procedure

Two sets of samples that represent the open- and closed-pore morphology of nanoporous organosilicates thin films were used in this experiment. These films were prepared based on the so-called sacrificial porogen (*pore generator*) approach developed by International Bussiness Machines Corp. (IBM™) Almaden Research Center. This technique involves the removal of the entrapped phase-separated organic macromolecular porogen within the crosslinked matrix selectively. Both open- and closed-pore samples were prepared by mixing with an appropriate amount of porogen loading into the matrix solution. Separate study has shown that higher porogen loading (45% in this study) leads to interconnected open-pore morphology, whereas lower porogen loading (15% in this study) leads to closed-pore structure [56]. The illustration of the 3-D pore structure was done by analyzing small-angle x-ray scattering data. Poly(propylene) oxide (PPO) with molecular weight, MW=12000 g/mol was used as the sacrificial porogen, whereas poly(methylsilsesquioxane) was used as the PMSSQ matrix precursor. Propylene glycol mono-n-propyl ether was used as a solvent for both porogen and matrix. The open-pore film was prepared by mixing 45 wt% of PPO porogen, whereas the closed-pore sample was prepared by mixing 15 wt% PPO into the PMSSQ solution. These PPO/PMSSQ mixtures were then filtered and spin coated homogenously on both heavily-doped (0.005 – 0.01 Ω-cm) and low-doped (9 – 18 Ω-cm) silicon wafers. The heavily doped sample was used for the dielectric constant measurement, whereas the low-doped sample was

used for the ellipsometric and FT-IR characterization. These samples were cured for 4 hours at 200°C under N_2 environment to produce porogen-phase-separated structure or "as-cured sample". The samples were then cut into smaller pieces (1 cm x 1.5 cm) for the studies presented in this paper.

The small pieces of as-cured samples underwent three different processes in sequence: thermal annealing, plasma etching and HMDS treatment. For annealing process, the as-cured samples underwent a direct thermal anneal of 430°C for 2 hours at 5°C/min ramping on a hot plate under N_2 environment. This process is for a complete porogen removal to generate nanoporous thin film. To simulate plasma damage during photoresist removal in the actual integrated circuit process, the annealed samples were exposed to CF_4/O_2 plasma (20 sccm/80 sccm) for 1 minute at 200W RF power. To repair the plasma-damaged samples, the films underwent silylation through HMDS treatment. The treatment was done inside a leak-free stainless steel reaction chamber (volume of chamber is 134.3 cm^3) with 3 ml of HMDS solution. The chamber was placed inside an oven. The temperature is raised from room temperature up to 80°C to enhance the vapor pressure of HMDS. After the 30 minutes of treatment, the chamber temperature was ramped down to room temperature.

The chemical structure of the porous films was investigated using FT-IR spectroscopy (Nicolet 4700, Thermo Electron Corp.) in 400 – 4000 cm^{-1} wavenumber range. The visual images of film were taken by a scanning electron microscope (SEM) (S4700, Hitachi Field Emission SEM) at 3 kV and 3.6 mm working distance. The refractive index, thickness and pore volume fraction were obtained by VASE™. The

ellipsometer measurements were taken at 4 incident angles of 60°, 65°, 70° and 75° in 400 – 1700 nm range with 5 nm step interval.

In ellipsometric analysis, a model is needed to generate Ψ and Δ spectra. A good match between experimental and generated spectra allows the extraction of optical constant and film thickness information. Spectroscopic ellipsometer can also be used to model a bilayer and graded porous sample showing the refractive index of film as a function of distance from silicon-film interface to film-air interface. The details of modeling single layer, bilayer, graded layer of nanoporous organosilicate films have been published recently [57].

5.6.3 Results and discussion

Process	Model	Thickness (±0.6 nm)	R.I. (±0.001, n)	Porosity (±2%)	Dielectric constant (k)
		Open-pore sample			
As-cured	Single	842.4	1.447	0	4.34±0.01
Annealed	Single	803.3	1.183	51	1.57±0.01
Plasma	Single	472.7	1.177-1.301	51*	2.51±0.1
HMDS	Bilayer-like				
	Top	178.0	1.25	33	2.06±0.01
	Bottom	312.9	1.185-1.25	51	
	Total thickness	490.9			

*Bottom layer

Process	Model	Thickness (±0.6 nm)	R.I. (±0.001, n)	Porosity (±2%)	Dielectric constant (k)
		Closed-pore sample			
Ascured	Single	856.7	1.420	0	4.22±0.01
Annealed	Single	709.2	1.307	20	2.30±0.01
Plasma	Single	564.3	1.315	18	2.26±0.02
HMDS	Single	562.4	1.319	18	2.28±0.02

Table 5-3 List of thickness, refractive index (R.I.), porosity and dielectric constant for both open- and closed-pore films of as-cured, annealed, plasma processed and hexamethyldisilazane treated

Process	Model	Thickness (±0.6 nm)	R.I. (±0.001, *n*)	Porosity (±2%)	Dielectric constant (*k*)
		Open-pore sample			
As-cured	Single	842.4	1.447	0	4.34±0.01
Annealed	Single	803.3	1.183	51	1.57±0.01
Plasma	Single	472.7	1.177-1.301	51*	2.51±0.1
HMDS	Bilayer-like				
	Top	178.0	1.25	33	2.06±0.01
	Bottom	312.9	1.185-1.25	51	
	Total thickness	490.9			

*Bottom layer

Process	Model	Thickness (±0.6 nm)	R.I. (±0.001, *n*)	Porosity (±2%)	Dielectric constant (*k*)
		Closed-pore sample			
Ascured	Single	856.7	1.420	0	4.22±0.01
Annealed	Single	709.2	1.307	20	2.30±0.01
Plasma	Single	564.3	1.315	18	2.26±0.02
HMDS	Single	562.4	1.319	18	2.28±0.02

Table 5-3 summarizes the thicknesses, refractive indexes, porosities and dielectric constant values for both open- and closed-pore films after exposure to various processes. This table will be referred throughout the text.

Figure 5-18 show the SEM images and depth profile analysis of the processed open-pore samples: (a) thermally annealed, (b) plasma exposed, (c) HMDS treated and

(d) depth profile of the mentioned processed samples. The pores appear to be randomly distributed and the film has a thickness around 700 nm. SE measurement gives a film thickness of 803.3 nm, refractive index of 1.183 and porosity of 51% (Figure 5-18(d) and Table 5-3(d)). The depth profile analysis shows an abrupt increased in refractive index at the silicon-film interface. We have already shown previously using ellipsometric analysis that the silicon-film interface has higher localized porosity (3 - 4%) as compared to the bulk [57]. IBM™ has also shown this using neutron reflectivity technique [58]. The thinner SEM thickness may be due to compression when the sample was cleaved because the open-pore film is relatively soft.

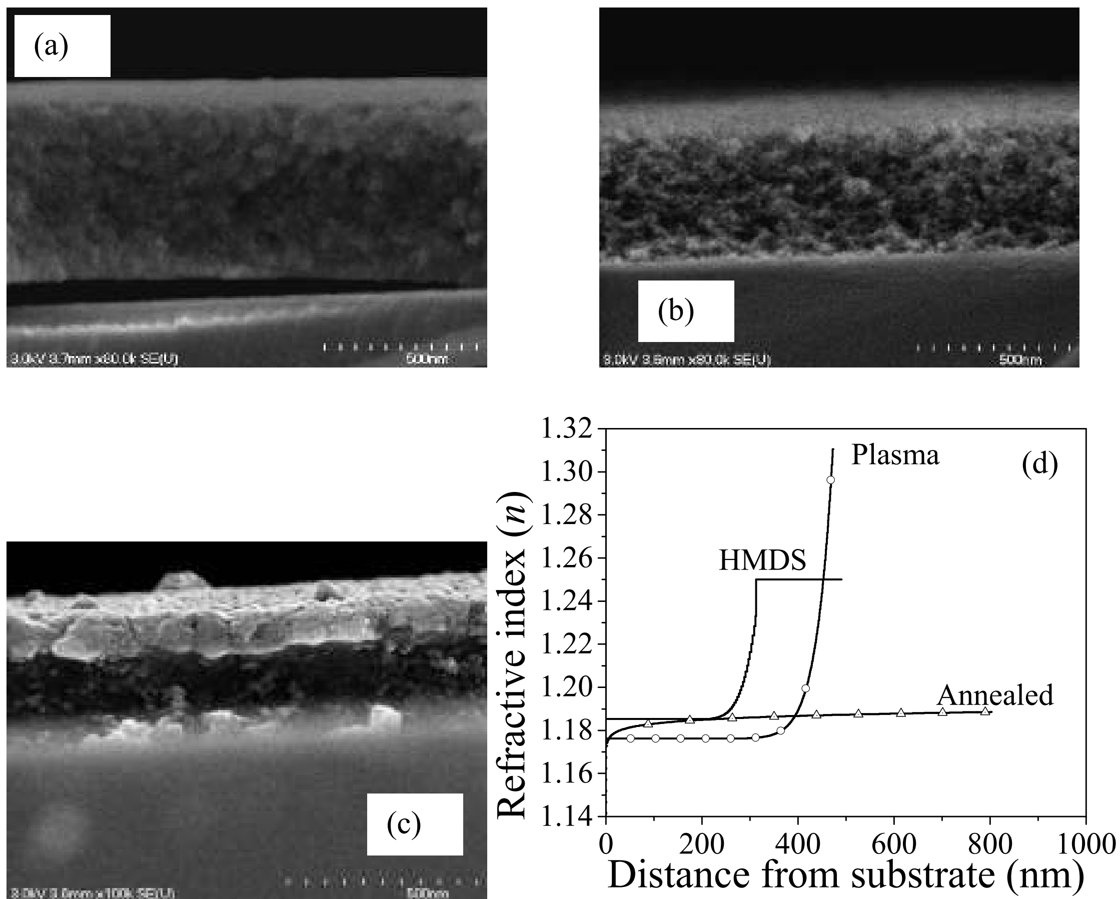

Figure 5-18 SEM images of open-pore sample after (a) annealing, (b) plasma treatment and (c) HMDS treatment and the correspondence (d) refractive index depth profile.

Figure 5-18(b) and (d) show the SEM cross section image and refractive index depth profile of the sample in Figure 5-18(a) after exposure to O_2/CF_4 plasma. The SEM thickness is around 465 nm which is comparable with ellipsometer thickness (472.7 nm). For ellipsometric analysis, the sample was first modeled as a single Cauchy layer. Details of SE modeling were thoroughly discussed in the paper that was published earlier [57]. However, the Cauchy model does not match well with the measured Ψ and Δ spectra as reflected by the relatively higher mean-squared error. The Cauchy model was then modified to a graded layer which improved the fit. Based on Figure 5-18 (d), it is found that the plasma damaged sample has non-uniform refractive index values at the top 1/3 layer. The refractive index values at the lower 2/3 layer remained almost constant at 1.177 (porosity of 51%) and then drastically increased towards the top up to 1.301. The thickness for O_2/CF_4 plasma treated film is reduced by 41% from 803.3 nm to 472.7 nm because of etching (Table 5-3). During the plasma treatment, we speculate that O_2 diffuse through the highly interconnected pore structure to a significant depth (upper 1/3 layer) removing $-CH_n$ groups from the pore surface by substitution reaction causing the formation of polar Si-OH in the following mechanism [59]:

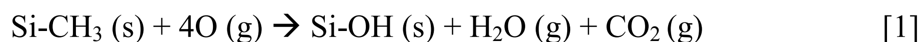

$$\text{Si-CH}_3\text{ (s)} + 4\text{O (g)} \rightarrow \text{Si-OH (s)} + \text{H}_2\text{O (g)} + \text{CO}_2\text{ (g)} \qquad [1]$$

This reaction leads to increasing refractive index values of the top layer as seen in Figure 5-18(d). Thus, raising the effective *k*-values of the films as shown later and causing electrical reliability problems in actual devices. The formation of silanol group at significant depth could also lead to more moisture adsorption. We also observed the depletion of –CH and increased of silanol group using FT-IR. The FT-IR spectra for this

study are not presented here, since many researchers have reported analysis on plasma-damaged samples [59,60,61].

Figure 5-18(c) and (d) shows the SEM image and refractive index depth profile of HMDS treated open-pore film. The image shows two distinct contrasts suggesting the presence of two layers after the HMDS treatment. Based on the SEM image, the top surface has thickness of 175 nm, while the bottom layer has thickness of 250 nm. The ellipsometric analysis showed that the bottom porous layer has almost constant refractive index of 1.185 and bottom/top layer interfaces. The top layer has constant refractive index of 1.25. The difference of refractive index indicates that the top 178 nm layer has less porosity than the bottom layer. By converting the Cauchy model to Bruggeman Effective Medium Approximation (BEMA) model, we calculated the pore volume fraction of the two layers. The BEMA model gave porosities of 51 ± 2% and 33 ± 2% for the bottom and top layers of the HMDS treated sample, respectively (Table 5-3). Before the treatment, the film porosity was 51% throughout the film. The results show that HMDS reactions in open-pore samples occur not only on the surface but also deeper into the upper 178 nm layer. The bottom 312.9 nm layer was unaffected with the treatment due to the presence of the denser top layer which, acts as barrier. However, the bilayer property after HMDS treatment means that the *k*-value will not be fully recovered to its initial value before plasma damage in open-pore films. The decrease in porosity on the top layer may be due to the reaction between HMDS and silanol that produces a byproduct of siloxane as suggested by Himchinshi [62,63]. HMDS reactions with silanol are given in the following reactions:

$(CH_3)_3Si\text{-}NH\text{-}Si(CH_3)_3\ (g) + HO\text{-}Si \rightarrow$

$$(CH_3)_3\text{-Si-O-Si (s)} + (CH_3)_3\text{-SiNH}_2\text{ (g)} \quad (2)$$

$$(CH_3)_3\text{-SiNH}_2\text{ (g)} + \text{HO-Si (s)} \rightarrow (CH_3)_3\text{-Si-O-Si(s)} + NH_3\text{(g)} \quad (3)$$

The results in Figure 5-18 (c) implies that although HMDS treatment is beneficial to create hydrophobicity, the silylation is not limited to the sample surface but penetrate into a certain depth as shown in the bilayer-like SEM image and spectroscopic ellipsometry analysis. This is contrary to the cited references above which stated that the silylation reaction occurs only at the surface. However, they did not specify if their sample has open-pore morphology like the ones used in this study. The dielectric constants of the processed films are also shown in. The dielectric constant of plasma-damaged sample is increased to 2.51. After the HMDS treatment, the dielectric constant is only 2.06 and not fully recovered to 1.57 (thermally annealed sample) because of the denser 187 nm top layer.

For closed-pore samples, the effects of plasma and HMDS treatment are different from open-pore sample. Figure 5-19 show SEM images of (a) thermally annealed, (b) plasma exposed and (c) HMDS treated sample. Figure 5-19 (d) shows the depth profiles of the processed sample. The thermally annealed closed-pore sample has 20% porosities with film thickness of 709.2 nm and refractive index of 1.307. After plasma exposure, only 20% of film thickness has been etched as compared to 41% to open-pore sample. This is because the closed-pore PMSSQ matrix is denser compared to open-pore sample, resulting in less plasma damage. It is also notable that there is no significant difference between the film properties of plasma-damaged and HMDS-treated closed-pore sample.

Both processed sample have equivalent porosities (18%) and refractive indexes (~1.32) with a slight variation of film thickness (i.e: plasma treated – 564.3 nm and HMDS treated – 562.4 nm). This may be due to the closed-pore nature of the film preventing further damage by plasma treatment. The O_2 plasma could not diffuse into the bulk because the pores are not interconnected. Based on Figure 5-19 (d), the depth profile analysis shows that the processed closed-pore samples are not graded indicating no plasma damage. In addition, the dielectric constant of closed-pore samples remained approximately unchanged after plasma and HMDS treatments ($k \sim 2.3$). The SEM images (Figure 5-18 (c)) of the treated closed-pore films also show evidence of a single layer. Based on the above discussion, we believed that the plasma-damaged sample repaired by HMDS treatment indeed depends on the pore morphologies of the samples.

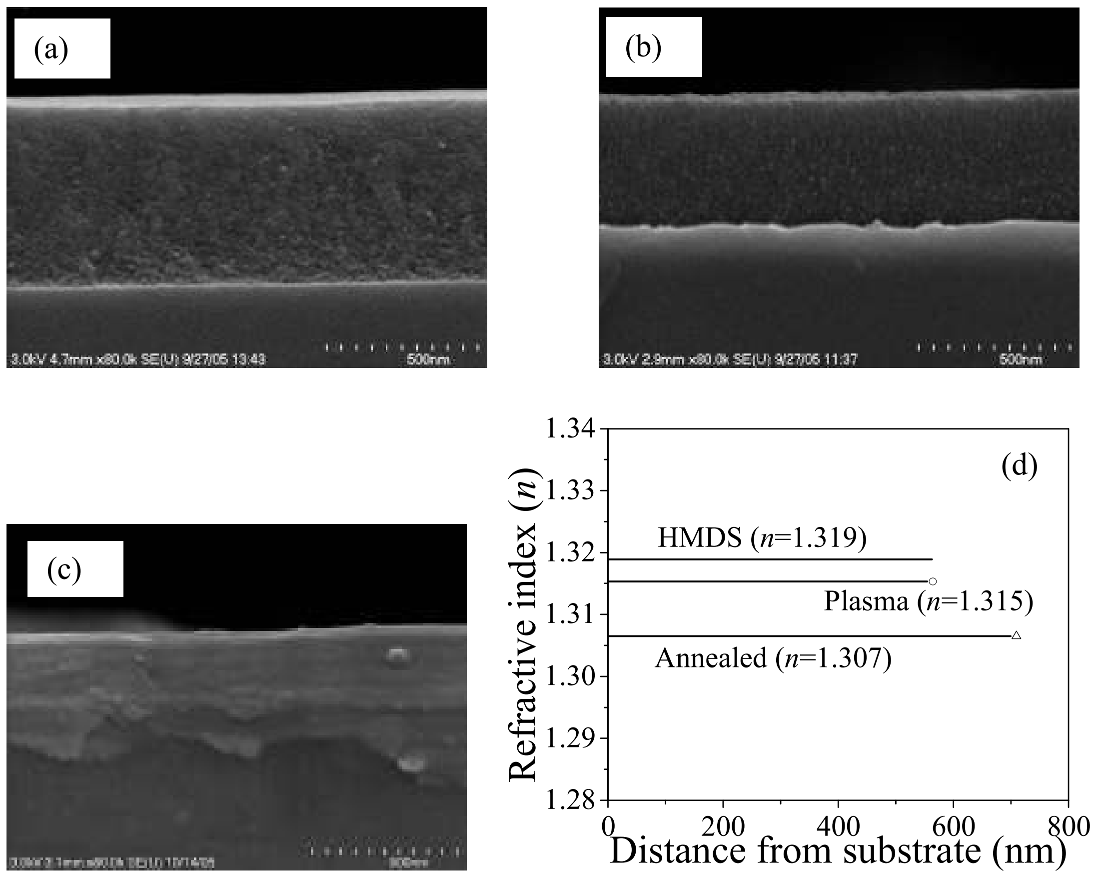

Figure 5-19 SEM images of closed-pore sample after (a) annealing, (b) plasma treatment and (c)HMDS treatment and the correspondence (d) refractive index depth profile.

5.7 Characterization of plasma exposed samples followed by porogen/water removal.

5.7.1 Overview

The conventional process for manufacture of integrated circuit devices involves in generating nanoporous film, followed by patterning process (photolithography and plasma process). However, this process flow leads to some disadvantages such as degrading the good quality of nanoporous material (increase *k*-value, and increase -OH content). In this dissertation, the ascured sample is first subjected to patterning process followed by generating nanoporous film process. This techniques can minimizes the damages occurs to sample after the plasma process.

5.7.2 Experiment

Similar as in previous experiments, two sets of open- and closed-pore organosilicates films are used here. The experimental procedures have been described in earlier section (see Table 1-2 Flowchart overview dissertation research work.). There are two sets of experiments:

(1) $SCCO_2$ process without plasma treatment (set #A)

(2) Plasma process followed by $SCCO_2$ process. (set #B)

5.7.3 Results and discussion

Figure 5-20 shows the refractive index depth profile of open-pore processed samples (a) with plasma process and (b) without plasma process. These samples underwent several processes such as $SCCO_2$ for water and porogen removal, VT/ HMDS and $SCCO_2$/TMCS treatment. Based on Figure 5-20 it can be seen that depth profile of sample with plasma process (set #B) is slightly grading from silicon/film interface to the top surface as compared to sample without plasma process (set #A). This suggests that the plasma process still damages the film top surface. Interestingly, the total film thickness of this sample is reduced by 9% from 803.3 nm to 728nm as compared to annealed samples with plasma process (41% etched: from 803.3 to 472.7nm) (see chapter 5.6). For $SCCO_2$ process sample without plasma process (set #A), the film refractive index is homogenous throughout film thickness because of no plasma damage. Figure 5-21 shows FT-IR spectra of 2800 cm-1 – 4000 cm^{-1} and 950 cm^{-1} – 1250 cm^{-1}, open-pore pore processed samples (a) and (c) with plasma process (b) and (d) without plasma process. For Si-O-Si (950 cm^{-1} – 1250 cm^{-1}) spectra, there are no differences between plasma processed and without plasma process. This indicates that the plasma processed prior to porogen/water removal process does not affect the Si-O-Si crosslinking which is desirable leading to a good mechanical strength. For methyl and silanol (2800cm^{-1} – 4000cm^{-1}) spectra, the –OH content after plasma exposure is increased. However, the silanol group can be removed by $SCCO_2$ and HMDS treatment. This shows that it is possible to first pattern the ascured sample, remove the photoresist residues and finally remove the porogen/water. This technique can minimize the plasma damage on

nanoporous film. The k-value of sample with plasma (set #B) (k= 1.76 ± 0.01) and without plasma (set #A) (k=1.8 ± 0.18) are almost equivalent.

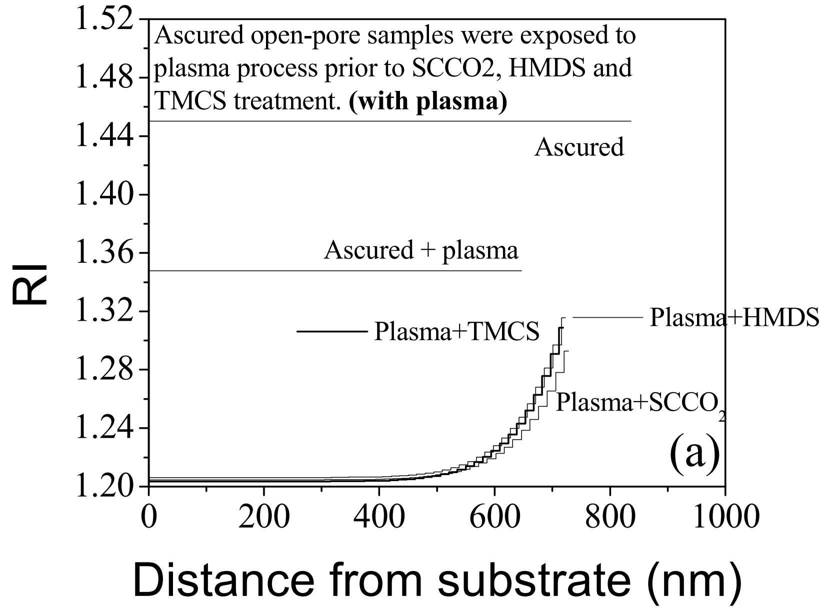

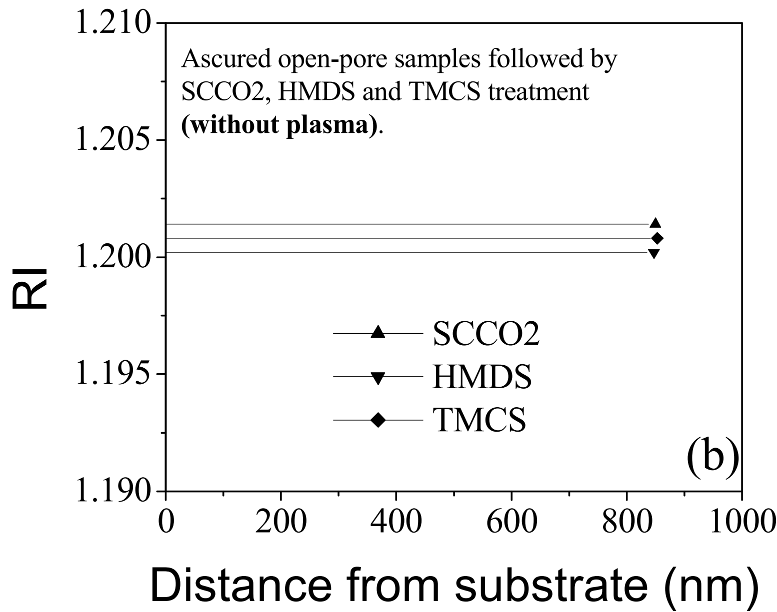

Figure 5-20 shows the refractive index depth profile of open-pore processed samples (a) with plasma process and (b) without plasma process.

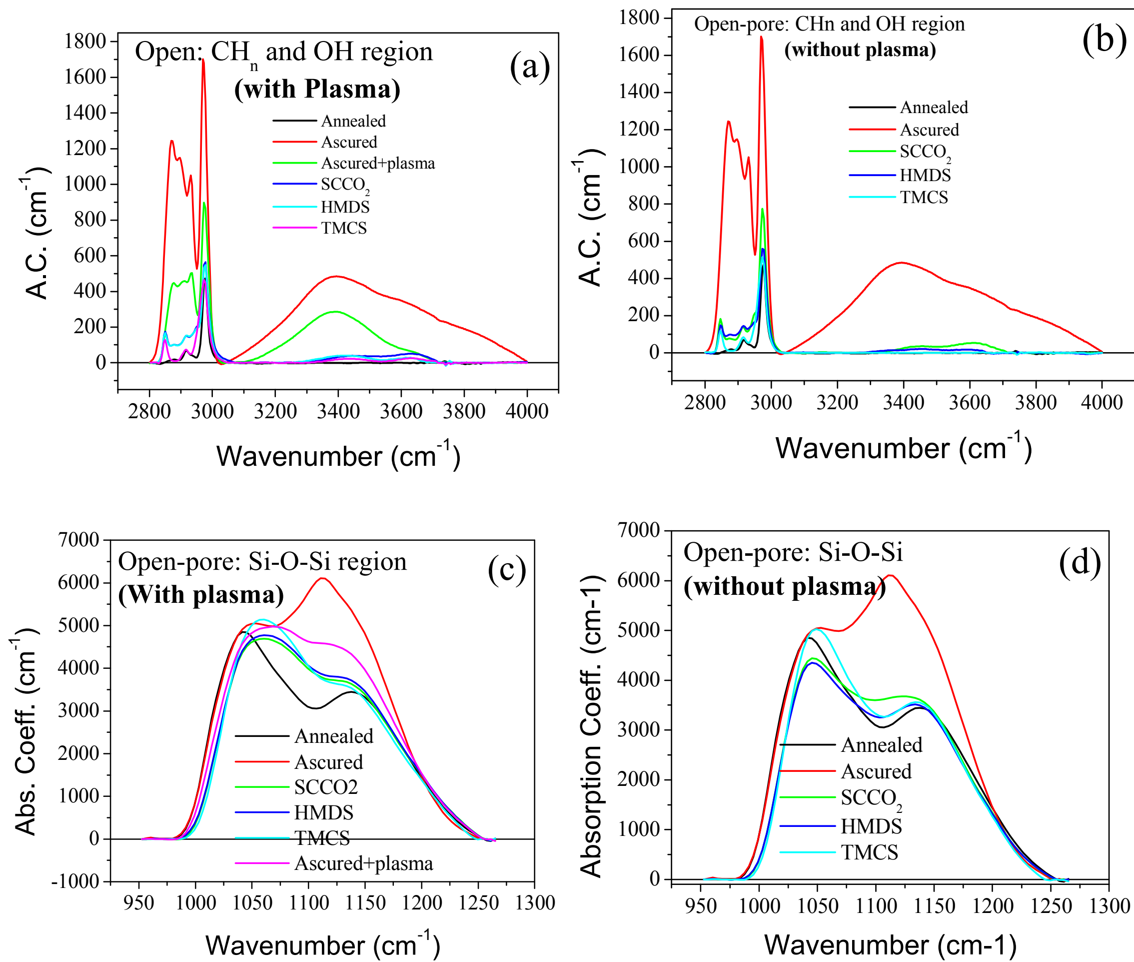

Figure 5-21 FTIR spectra of 2800cm-1 – 4000 cm^{-1} and 950cm^{-1} – 1250cm^{-1}, open-pore pore processed samples (a) and (c) with plasma process (b) and (d) without plasma process. For Si-O-Si (950 cm^{-1} – 1250 cm^{-1}) spectra.

Figure 5-22 shows the depth profile of closed-pore processed samples (a) with plasma process and (b) without plasma process. These samples underwent several processes such as $SCCO_2$ for porogen/water removal, VT/HMDS and $SCCO_2$/TMCS treatment. For closed-pore sample, the samples with plasma process (set #B) have slightly less thickness

as compared to without plasma process (set #A). These effects are not as severe as open-pore sample. The film thickness of set #A and set #B is 742 nm and 697.7nm, respectively. This is expected because of it closed-pore morphology nature blocking O attacks deeper into the sample. This can be verified via the FT-IR spectra. Figure 5-23 shows FT-IR spectra of 2800 cm^{-1} – 4000 cm^{-1} and 950 cm^{-1} – 1250 cm^{-1}, closed-pore pore processed samples (a) and (c) with plasma process (b) and (d) without plasma process. Similar as open-pore sample, the Si-O-Si crosslinking of the processed sample does not change as much.

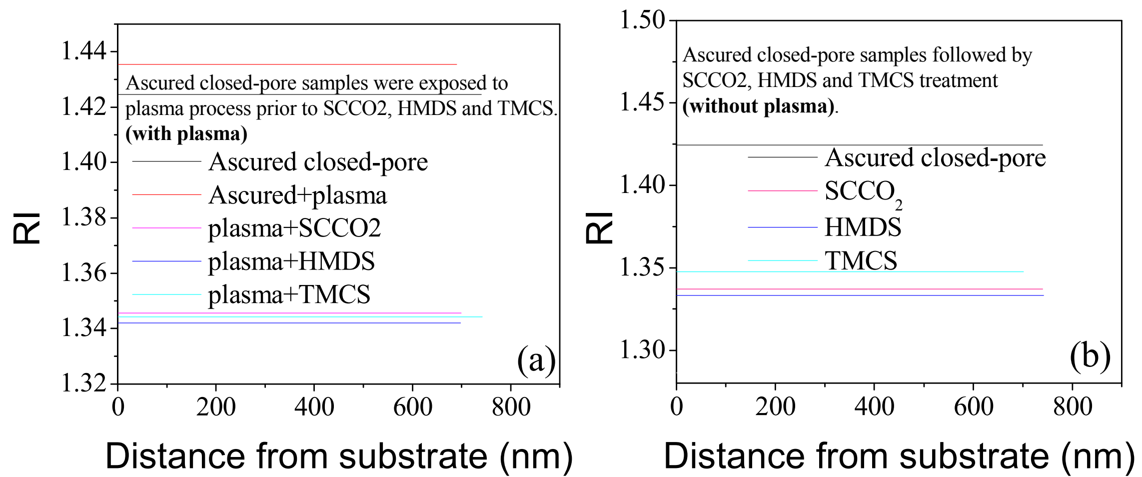

Figure 5-22 Depth profile of closed-pore processed samples (a) with plasma process and (b) without plasma process.

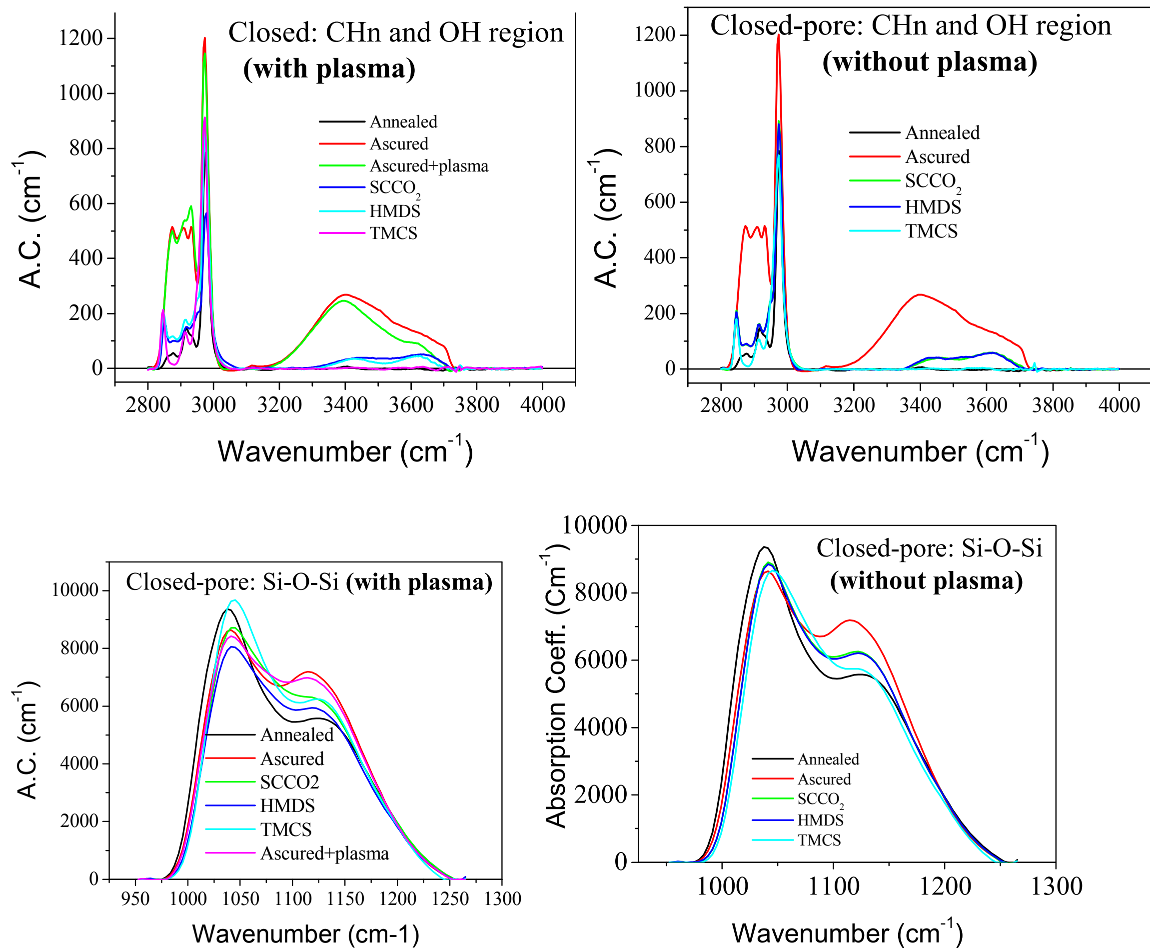

Figure 5-23 FT-IR spectra of 2800cm^{-1} – 4000 cm^{-1} and 950 cm^{-1} – 1250cm $^{-1}$, closed-pore pore processed samples (a) and (c) with plasma process (b) and (d) without plasma process.

Chapter 6

Conclusion/Future Work

6.1 Conclusion/Future Work

This dissertation research found that depth profile spectroscopy ellipsometry (SE) can be used to evaluate the performance of supercritical CO_2 ($SCCO_2$) process in generating nanoporous thin film for microelectronics application. This research shows designed analytical models used to describe a single layer porous film, bi-layer porous film and also a plasma-damaged graded single layer porous film. The mentioned films may be encountered during the fabrication of porous low-*k* insulator in semiconductor industry. Based on SE analysis, it can successfully distinguish between a bi-layer and single layer porous sample accurately. SE analysis is indeed better than conventional tools for porous film characterization, due to it quick measurement, no sample preparation and does not render sample reusability.

VASE™ showed than the $SCCO_2$ process can be utilized to create porous film, remove water, repair plasma-damaged and also seal pores. This research shows supercritical CO_2 processes with addition of appropriate co-solvents have successfully extracted porogen and water efficiently for both closed- and open-pore thin film. Depth profile SE analysis together with FT-IR analysis proved to be a good technique to

understand the effects of each process on the porous films. Depth profile SE also shows that the $SCCO_2$/MEK, THF-processed film has higher refractive index as compared to annealed sample due to incomplete water removal. This problem can be solved by reprocessing the processed $SCCO_2$/MEK, THF porous sample with $SCCO_2$/methanol treatment to remove bonded –OH groups. Depth profile SE shows the processed $SCCO_2$/methanol gives comparable refractive index values as compared to direct thermal annealing sample. Furthermore, the $SCCO_2$ process is performed at lower temperature (160°C) which proved to produce an equivalent porous film property as compared to standard thermal decomposition (~450°C). This work indeed shows that $SCCO_2$ treatment has performed better than thermal annealing process at shorter time and lower temperature. Upon a complete removal or porogen and water, the porous film may still be vulnerable towards water absorption throughout time. Hence, $SCCO_2$/TMCS and HMDS vapor treatment are used to terminate the silanol group with methyl group and to seal the pores to hinder the adsorption of water from environment and copper contamination. In conclusion, the depth profile SE analysis can offer a great ability in understanding of the physical properties of porous film.

References:

1. www.intel.com, March 2006.

2. R.Hiremane, Technology Intel Magazine, April, pp. 1-9 (2005)

3. M.R. Baklanov, K.P. Mogilnikov, V.G. Polovinkin and F.N. Dultsev, *The Journal of Vacuum Science and Technology B*, **18**, 1385 (2000).

4. E. Kondoh, M.R. Baklanov, E. Lin, D. Gidley and A. Nakashima, *Japanese Journal of Applied Physics*, **40**, L323 (2001).

5. B. Kastenmeier, K. Pfeifer and A. Knorr, "Porous Low-k Materials and Effective *k* ," *Semiconductor International*, July 2004, pp. 87.

6. http://public.itrs.net. Feb. 2006.

7. L. Peters, "Is pore sealing key to ultralow-*k* adoption" *Semiconductor International*, October, pp. 49 (2005).

8. R.D. Miller, W. Volksen, J.L. Hedrick, C.J. Hawker, J.F. Remenar, P. Furuta, C.V. Nguyen, D. Yoon, M. Toney, D.P. Rice and J. Hay, *Material Research Society* Conference Proceedings ULSI XV, pp. 327 -333 (2000).

9. R.D. Miller, J.L. Hedrick, D.Y. Yoon, R.F. Cook and J.P. Hummel, *Material Research Society*, October, pp. 44 - 48 (1997).

10. J.L. Hedrick, R.D. Miller, C.J. Hawker and K.R. Carter, W. Volksen, D.Y. Yoon and M. Trollsas, *Advanced Materials*, **10**(13), pp. 1049-1053 (1998).

11. J. McHardy and S.P. Sawan, *Supercritical Fluid Cleaning: Fundamentals, Technology and Applications*, (Noyes Publications: New Jersey, 1998).

12. T. Gougousi, D. Barua, E.D. Young and G.N. Parsons, *Chemistry of Materials*, **17**, pp. 5093-5100 (2005)

13. A. Cabanas, D.P. Long and J.J. Watkins, *Chemistry of Materials*, **16**, pp. 2028-2033 (2004)

14 . X.R. Ye, R. Xiang, C.M. Wai, Y. Lin, Yuehe, J.S. Young and M.H. Engelhard, *Surface and Coatings Technology*, **190**(1), pp. 25-31(2005).

15. R.F. Reidy, Z. Zhang, R.A. Orozco-Teran, B.P. Gorman, D.W. Mueller, Materials Research Society Symposium Proceedings, *Materials, Technology and Reliability for Advanced Interconnects and Low-k Dielectrics*, **766**, pp. 303-308 (2003).

16. Turkot *et al*. (2005)

17. P.D. Matz and R.F. Reidy, Diffusion and Defect Data--Solid State Data, 103-104(Ultra Clean Processing of Silicon Surfaces VII), *Solid State Phenomena Pt. B*, pp. 315-322. (2005)

18. P.M. Capani, P.D. Matz, D.W. Mueller, M.J. Kim, E.R. Walter, J.T. Rhoad, E.L. Busch, R.F. Reidy, *Material Research Society Symposium Proceeding*, **863**, pp. B2.7.1 – B2.7.6 (2005).

19. B.P. Gorman, R.A. Orozco-Teran, Z. Zhang, P.D. Matz, D.W. Mueller and R.F. Reidy, *The Journal of Vacuum Science and Technology B*,, **22**(3), pp. 1210-1212 (2004).

20. Martinez *et al*. (2003)

21. J.A. Lubguban, S. Gangopadhyay, B. Lahlouh, T. Rajagopalan, N. Biswas, J. Sun, D.H. Huang, S.L. Simon, A. Mallikarjunan, H-C. Kim, J. Hedstrom, W. Volksen, R.D. Miller and M.F. Toney, *Journal of Materials Research*, **19**, 3224 (2004).

22. K. Maex, M.R. Baklanov, D. Shamiyan, F. Iacopi, S.H. Brongersma and Z.S. Yanovitskaya, *Journal of Applied Physics*, **93**, 8793 (2003).

23. S. Terada, T. Kinashi and J. Spear, *AIP Conf. Proc.,* **683,** 546 (2003).

24. J. Ilavsky, A. J. Allen, G. G. Long and P. R. Jemian, Review of Scientific Instrument, *AIP*, 73, 1660 (2002).

25. A.A. Herrero, R.L. Heredero, E. Bernabeu and D. Levy, *Applied Optics*, 40, 527 (2001).

26. M.R. Baklanov, K.P. Mogilnikov, V.G. Polovinkin and F.N. Dultsev, *The Journal of Vacuum Science and Technology B*, 18, 1385 (2000).

27. K.P. Mogilnikov, V.G. Polovinkin, F.N. Dultsev and M.R. Baklanov, *Material Research Society Symposium Proceeding*, **565**, 81 (1999).

28. D.W. Gidley, W.E. Frieze, T.L. Dull, J.Sun, A.F. Yee. C.V. Nguyen. D.Y. Yoon, *Applied Physics Letters*, **76,** 1282 (2002).

29. H.G. Tompkins and W.A. McGahan, *Spectroscopic Ellipsometery and Reflectometry A User's Guide*, (John Wiley & Sons, 1999).

30. D.E. Aspnes, Thin Solid Films, **89**, 249 (1982).

31. K.R. Carter, R.F. Cook, M.A. Harbison, C.J. Hawker, J. L. Hedrick, S. Kim, G. Liniger, R.D. Miller, W. Volksen and D.Y. Yoon, USPTO 5,953,627, 1999.

32. J. Woollam, B. Johs, C. herzinger, J. Hilfiker. R. Synowicki and C. Bungay, *Critical Review of Optical Science and Technology*, Society of Photo-Optical Instrumentation Engineers, **CR72**, 1 (Optical Metrology: Washington, 1999).

33. D. Shamiryan, T. Abell, Q.T. Le and K. Maex, *Microelectronic Engineering*, **70**/2-4, 341 (2003).

34. J.G. Webster, *Wiley Encyclopedia of Electrical and Electronics Engineering Supplement 1*, (John Wiley and Sons, 2000).

35. Hect, *Optics 4th edition*, (Addison Wesley, 2002).

36. M. Born and E. Wolf, *Principles of optics: Electromagnetic theory of propagation, interference and diffraction of light* 7th edition, (Cambridge University Press, 1999).

37. F.L. Pedrotti and L.S. Pedrotti, *Introduction to Optics 2nd edition*, (Prentice Hall, 1993).

38. R.M.A. Azzam and N.M. Bashara, *Ellipsometry and Polarized Light*, (North-Holland Personal Library, 1987).

39. W.H. Press, B.P. Flannery, S.A. Teukolsky, and W.T. Vetterling, *Numerical Recipes: The Art of Scientific Computing* (Cambridge University Press: Cambridge, MA, 1988).

40. A.V. Goncharenko, Phys. Rev. E, **68,** 1 (2003).

41. D.E. Aspnes, Thin Solid Films, **89**, 249 (1982).

42. C. M. Herzinger, B. Johs, W. A. McGahan, J. A. Woollam and W. Paulson*, Journal of Applied Physics*, **83**, 3323 (1998).

43. E.D. Palik., *Handbook of optical constants of solids*, (San Diego: Academic Press, 1998).

44. C. Himcinschi, M. Friedrich, C. Murray, I. Streiter, S.E. Schulz, T. Gessner and D.R.T Zahn, *Semiconductor Science Technology*, **16**, pp. 806-811 (2001).

45. C. Himcinschi, M. Friedrich, C. Murray, I. Streiter, S.E. Schulz, T. Gessner and D.R.T Zahn, *Anal. Bioanal. Chem.*, **374**, pp. 654-657 (2002).

46. A. Alvarez-Herrero, R.L. Heredero, E. Bernabeu and D. Levy, *Applied Optics*, **40**(4), pp. 527 – 532 (2001).

47. J.M. Hollas, *High Resolution Spectroscopy*, (New York: John Wiley & Sons, 1998).

48. H.C. Kim, J.B. Wilds, C.R. Kreller, W. Volksen, P.J. Brock, V.Y. Lee, T. Magbitang, J.L. Hedrick, C.J. Hawker and R.D. Miller, *Advanced Materials*, 14, 1637 (2002).

49. McHardy J., *Supercritical Fluid Cleaning*, (New Jersey: Noyes Publications, 1998).

50. Taylor L.T., *Supercritical Fluid Extraction: Techniques in Analytical Chemistry*, John Wiley & Sons., Inc. (1996).

51. Rajagopalan T., Lahlouh, Lubguban J.A., Biswas N., Gangopadhyay S., Sun J., Huang D.H. and Simon S.L., Mallikarjunan, Kim H.-C., Volksen W., Toney M.F., Huang E., Rice P.M., Delenia and Miller R.D., *Applied Physics Letters*, **82**(24), pp. 4328-4330 (2003).

52 L.T. Taylor, Supercritical Fluid Extraction, (John Wiley & Sons, 1996).

53. B. Xie and A.J. Muscat, *IEEE Transaction of Semincoductor Manufacturing*, **17**(4) (2004).

54 M.T. Othman, J.A. Lubguban, A.A. Lubguban and S. Gangopadhyay, R. D. Miller, W. Volksen and H.-C. Kim, *Journal Applied Physics*, in press.

55. H-C. Kim, W. Volksen, R.D. Miller, E. Huang, G. Yang, R. M. Briber, K. W. Shin and S.K. Satija, *Chemistry of Materials*, **15**, 3 (2003).

[56] J.A. Lubguban, S. Gangopadhyay, B. Lahlouh, T. Rajagopalan, N. Biswas, J. Sun, D.H. Huang, S.L. Simon, A. Mallikarjunan, H-C. Kim, J. Hedstrom, W. Volksen, R.D. Miller and M.F. Toney, J. Mater. Res., **19**, 3224 (2004).

[57]M.T. Othman, J.A. Lubguban, A.A. Lubguban, S. Gangopadhyay, R.D. Miller, W. Volksen and H.-C. Kim, J. Appl. Phys. **99**, 083503 (2006).

[58] H.-C Kim, W. Volksen, R.D. Miller, E. Huang, G. Yang, R.M. Briber, K. W. Shin, and S.K. Satija, Chem. Mater. **15**, 609 (2003).

[59] B. Lahlouh, J.A. Lubguban, G. Sivaraman, R. Gale and S. Gangopadhyay, Electrochemical and Solid-State Letters, **7,** G338 (2004).

[60] B.P. Gorman, R.A. Orozco-Teran, Z. Zhang, P.D. Matz, D.W. Mueller and R.F. Reidy, The Journal of Vacuum Science and Technology B, **22**, 1210 (2004).

[61] T. Rajagopalan, B. Lahlouh, J.A. Lubguban, N. Biswas, S. Gangopadhyay, J. Sun, D. H. Huang, S. L Simon, D. Toma, R. Butler, Applied Surface Science, **252**, 6323 (2006).

[62] C. Himcinschi, M. Friedrich, C. Murray, I. Streiter, S.E. Schulz, T. Gessner and D.R.T Zahn, Semiconductor Science Technology, **16**, 806 (2001).

[63] C. Himcinschi, M. Friedrich, C. Murray, I. Streiter, S.E. Schulz, T. Gessner and D.R.T Zahn, Anal. Bioanal. Chem., **374**, 654 (2002).

VITA

Maslina Tasrin Othman was born December 21st, 1977 in Kuala Lumpur, Malaysia. She obtained all her three degrees from Department of Electrical and Computer Engineering, University of Missouri – Columbia: undergraduate, master and PhD. She received her Bachelor of Science in Electrical Engineering with Honors (2000). She then continued her master degree in the department of Electrical Engineering (2002) focusing on microwave and optical remote sensing studies. She finally completed her Ph.D. studies in Electrical Engineering (2007) focusing on microelectronic/semiconductor area. Completion of this dissertation concludes her Doctor of Philosophy in Electrical Engineering.